



universität  
wien

# DISSERTATION

Titel der Dissertation

“Synthesis of biomimetic surfaces under permanent in situ FTIR ATR  
monitoring”

Verfasserin

Dipl. Phys.Chem. Jasmina Matijašević

angestrebter akademischer Grad

Doctor of Philosophie (PhD)

Wien, 2008

Matrikel-Nummer: A 0408891

Dissertationsgebiet (lt. Studienblatt): Chemie

Betreuer: Univ.-Prof. Dr. Urs Peter Fringeli



*“When God made the solid state he left the surface to the Devil.”*

Enrico Fermi



## **ACKNOWLEDGMENT**

At the end of these four years I am pleased to take the opportunity to address my deep gratitude to people who have contributed to this thesis with their knowledge, friendship and financial support. Even though there were not so many, each and every one of them played a significant role in my arrival and survival in Vienna, and therefore they will remain in my heart forever.

Firstly, and most importantly, I am deeply indebted to supervisor Univ. Prof. Dr. Urs Peter Fringeli for giving me the opportunity to work within his research group.

I am grateful to him for teaching me thoroughness in scientific thinking, critical reviews, constructive suggestions; for giving me the chance to go to conferences in Leoben and London, and for supporting me throughout the whole thesis.

I am also thankful to Univ. Ass. Dr. Dieter Baurecht for helpful discussions regarding modulation spectroscopy and for help to finish this thesis; to Mag. Norbert Hassler for continuous encouragements, scientific and private conversations, for friendship and refreshing talks, for help with German language; to Dr. Gerald Reiter, a former member group, who helped me to start up by introducing me to the instrument and data evaluation; to Ing. Regina Prossinag for the familiar atmosphere and tones of cappuccino.

I am grateful to Karlsruhe research group for collaboration and AFM and EDX-ESEM measurements.

In addition, I wish to thank to O. Univ. Prof. Dr. Franz L. Dickert for giving me the opportunity to work as a student assistant at Vienna University and to finish my thesis.

I would also like to give my warmest thanks to my brother Dušan and my parents Mirjana and Sreten for their support and encouragement. I am grateful to my new friends too: Ivana, Alma and Irman who I met in Vienna.

Finally, I wish to thank my boyfriend Goran for his constant support, for his never-ending patience and, most importantly, for being “on line” when I needed him, no matter how many kilometres we were apart!



## Summary

Organized organic molecular monolayer and multilayer structures formed at solid surfaces by spontaneous adsorption of molecules from solutions are known as self-assembled mono- and multi-layers (SAMs). They have been studied extensively because they form well-ordered, cross-linked two-dimensional structures important for biomaterials and biosensors, nonlinear optical devices, HPLC, nanolithography, a variety of heterogeneous phenomena including catalysis, corrosion, lubrication, adhesion, and dispersion and deagglomeration of nanoparticles. Such self-assembled structures may provide formation of molecular structures with known spacing, orientation and thickness.

This work was focused on the study of *n*-alkyltrichlorosilanes which act as coupling agents between organic compounds (e.g. proteins) and inorganic hydroxylated surfaces (glass, quartz, germanium, silicon and metal oxides). Since the silane surface layer is planned as anchor for biomimetic surface formation, we directed attention to a most accurate quantitative analysis of the layer growth, surface concentration and the surface chemical reactions *in situ* by means of Single-Beam-Sample-Reference (SBSR) and Modulated Excitation (ME) Attenuated Total Reflection (ATR) FTIR spectroscopy.

The formation of self-assembled layers using the highly reactive compound 7-octenyltrichlorosilane (7-OTCS) was the first step of a novel and successful approach to *in situ* monitoring and quantifying surface chemical reactions on a molecular level. Surface reaction was performed on a germanium Multiple Internal Reflection Element (Ge MIRE). Activation of the surface resulted in free Ge-OH groups used for a spontaneous chemical reaction with 7-OTCS in toluene. Formation of Ge-O-Si bonds was enabled by hydrolization of Si-Cl<sub>3</sub> after partial elimination of a tightly bound thin water layer covering the MIRE. Unwanted side-reaction by hydrolization of Si-Cl<sub>3</sub> in solution followed by polymerization paralleled this process. Steady growing of the silane layer to multilayer thickness with increasing time was observed in all experiments.

Most unexpectedly, in some experiments the end-standing double bond of the silane layer was found to be partly oxidized without adding oxidative chemicals. Oxidation continued slowly even in pure solvent (toluene). Investigation of the ultra-structure of the layer by Atomic Force Microscopy (AFM) and Energy Dispersive X-ray Analysis

(EDX) using an Environmental Scanning Electron Microscope (ESEM) has revealed that nanoparticle sized remnants of molecular sieve used for solvent drying were incorporated into the silane layer as well as suspended in the bulk. We suggest that they acted as catalyst for the double bond oxidation by small amounts of dissolved oxygen.

Special attention had to be paid to background compensation of the final and time-resolved spectra of 7-octenylsilane layer (OCS-layer). For this purpose a special algorithm enabling automatic solvent/solution compensation has been developed. Background incompensation was a consequence of solvent (toluene) and 7-OTCS/toluene solution displacement by the attached layer as well as by toluene dilution by 7-OTCS molecules. Since 7-OTCS in solution spontaneously reacts with the Ge surface the measurement of a reference spectrum reflecting only dissolved 7-OTCS in toluene was disabled. This problem was overcome by the application of basic ATR theory.

The second step of building selective surface layer assemblies deals with the oxidation of the end-standing double bond of the silane layer by ozone. The ozonization process had led directly to the aimed carboxylic acid groups. A so-called "activated ester" method is used for the chemical modification of the carboxyl groups of the silane layer to *N*-hydroxysuccinimide (NHS) ester groups and immobilization of amine-terminated biomolecules.

In the last step of biomimetic surface formation glycosamine hydrochloride and amino-dextran have been immobilized to the surface via amide bond formation. The effectivity of saccharide covered silane layers toward non-specific protein Bovine Serum Albumin (BSA) adsorption was investigated. Compared to a clean Ge MIRE both types of saccharide modified surfaces have shown significant 70-80 % lower non-specific protein adsorption. It was shown that glucose monomer (glucosamine hydrochloride) is equally effective as glucose polymer (amino-dextran) that are much more expensive. The advantages of glucose modified surfaces used in biomedical applications are biocompatibility and slow biodegradability. Such surfaces are of considerable general interest since they serve as a base for most medical assays and many chemical sensors.



## Zusammenfassung

In dieser Arbeit wurden die Eigenschaften von 7-Octenyltrichlorsilan (7-OCTS) im Bezug auf die Verwendung als Bindeglied organischer Substanzen (z.B. Proteine) und anorganischer hydroxylierter Oberflächen (Germanium) untersucht. Dabei wurde besonderes Augenmerk auf eine genaue quantitative Beschreibung der Schichtentstehung, der resultierenden Oberflächenkonzentration und der chemischen Oberflächenreaktion gelegt. Als Messmethoden wurden mit der SBSR (Single Beam Sample Reference) Methode und modulierter Anregung (ME modulated excitation) zwei spezielle Methoden der FTIR (Fourier Transform Infrared) - ATR (Attenuated Total Reflection) Spektroskopie eingesetzt.

Die sich selbst anordnende Schicht der hoch reaktiven Substanz 7-OTCS wurde auf der Oberfläche eines Germanium-MIRE (multiple internal reflection element) hergestellt. Für die Auswertung hatte die genaue Kompensation der Hintergrundabsorption der 7-Octenylsilan-Schicht (OCS-Schicht) in den zeitaufgelösten Spektren sowie in den Spektren der fertigen Schicht höchste Priorität, wofür ein spezieller Algorithmus entwickelt wurde, der eine automatische Kompensation von gelöstem Stoff und Lösungsmittel zulässt.

Der zweite Schritt in der Herstellung dieser Schicht mit selektiver Oberfläche betrifft die Oxidation der endständigen C=C Doppelbindungen des Silans durch Ozon. Die Reaktion mit Ozon führte direkt zu den gewünschten Carbonsäuregruppen. Die sogenannte "activated ester" Methode diente zur chemischen Modifizierung der Carboxylgruppen des Silans in *N*-hydroxysuccinimid Ester Gruppen. Im letzten Schritt wurden Glucosamin und Amino-dextran auf dieser Oberfläche kovalent gebunden.

Verglichen mit einer reinen Oberfläche eines Ge-MIRE zeigten beide Arten der saccharid-modifizierten Oberflächen eine um 70-80% geringere nicht-spezifische Proteinadsorption. Der Vorteil der Verwendung derart modifizierter Oberflächen für biomedizinische Anwendungen sind Biokompatibilität und Stabilität gegenüber Abbauvorgängen.

Solche Oberflächen sind von großem allgemeinen Interesse, da sie als Basis für die meisten medizinischen Assays und viele chemische Sensoren dienen.

## Table of Content

<b>CHAPTER 1 GENERAL INTRODUCTION .....</b>	<b>7</b>
1.1 HISTORICAL OVERVIEW OF ORGANIC THIN FILMS .....	7
1.2 DEFINITION OF SELF-ASSEMBLED MONO- AND MULTI-LAYER (SAM) FILMS .....	8
1.3 STRUCTURE AND VARIETY OF SAM FILMS.....	9
1.4 STRUCTURE OF THE SAM FILMS PRODUCED BY ALKYLCHLOROSILANES.....	10
1.4.1 <i>Selecting a silane coupling reagent</i> .....	10
1.4.2 <i>Methods of applying silane coupling reagents</i> .....	11
1.4.3 <i>Formation of SAM films</i> .....	12
1.5 REVIEW OF EXPERIMENTAL TECHNIQUES.....	13
1.6 SOME OF THE SAM FILM CHARACTERIZATION DIFFICULTIES .....	14
1.7 IMPORTANCE OF SAM FILMS .....	15
1.8 BIOMOLECULE IMMOBILIZATION ON SAM FILMS .....	17
1.8.1 <i>Biosensors and biochips for diagnostic</i> .....	17
1.8.2 <i>Medical implants in the human body</i> .....	18
<b>CHAPTER 2 ATR FTIR SPECTROSCOPY.....</b>	<b>20</b>
2.1 THE PRINCIPLE OF TOTAL INTERNAL REFLECTION.....	20
2.1.1 <i>Relative electric field components</i> .....	23
2.1.2 <i>Effective thickness</i> .....	25
2.1.3 <i>Oriented samples</i> .....	26
2.1.4 <i>The surface concentration</i> .....	31
2.1.5 <i>Number of the internal reflection</i> .....	33
2.2 THEORETICAL BACKGROUND CONSIDERATIONS .....	34
<b>CHAPTER 3 MATERIALS AND METHODS .....</b>	<b>38</b>
3.1 EXPERIMENTAL TECHNIQUES .....	38
3.1.1 <i>FTIR ATR equipment</i> .....	38
3.1.2 <i>SBSR spectroscopy</i> .....	38
3.1.3 <i>Modulation Spectroscopy</i> .....	40
3.1.4 <i>Atomic Force Microscopy (AFM) and Environmental Scanning             Electron Microscopy (ESEM)</i> .....	45
3.2 CHEMICALS.....	46
3.3 METHODS .....	47
3.3.1 <i>Polishing and surface activation of Ge ATR MIRE</i> .....	47

3.3.2	<i>Silanization of the Ge and CdTe MIREs</i> .....	47
3.3.3	<i>Oxidation of terminal double bond of the silane layer by ozone</i> .....	48
3.3.4	<i>Identification of the expected COOH group</i> .....	49
3.3.5	<i>Activation of the carboxyl groups</i> .....	50
3.3.6	<i>Amide bond formation between amino species and NHS-ester terminated silane layer</i> .....	51
3.3.7	<i>Bovine Serum Albumin (BSA) adsorption</i> .....	52
<b>CHAPTER 4</b>	<b>RESULTS AND DISCUSSION</b> .....	<b>53</b>
4.1	SILANIZATION.....	53
4.1.1	<i>Surface activation of Ge MIRE</i> .....	53
4.1.2	<i>Silane layer preparation on Ge MIRE</i> .....	54
4.1.3	<i>Background compensation</i> .....	58
4.1.3.1	Background compensation of the final OCS-layer .....	58
4.1.3.2	Background compensation of the time-resolved spectra of OCS-layer growth.....	62
4.1.4	<i>Kinetics of the silane layer formation</i> .....	65
4.2	OXIDATION OF THE SILANE LAYER.....	68
4.2.1	<i>Oxidation of terminal ethylenic double bond of the silane layer by ozone</i> .....	68
4.2.2	<i>Proof of the existence of end-standing COOH groups</i> .....	69
4.3	ACTIVATION OF THE CARBOXYLIC ACID TERMINATED SILANE LAYER .....	74
4.3.1	<i>NHS effect on the carboxyl silane layer groups</i> .....	74
4.3.2	<i>The NHS-ester stability</i> .....	76
4.3.3	<i>NHS-ester terminated silane layer</i> .....	77
4.4	AMIDE BOND FORMATION .....	79
4.4.1	<i>Glucosamine hydrochloride binding to a silane layer via amide bonds</i> .....	80
4.4.2	<i>Deactivation of remained NHS-ester groups of the silane layer by ethanolamine</i> .....	84
4.4.3	<i>Overall amount of formed amide bonds</i> .....	86
4.5	BOVIN SERUM ALBUMIN (BSA) ADSORPTION ON GLUCOSE COVERED SILANE LAYER .....	89
4.6	PRELIMINARY EXPERIMENTS WITH AMINO-DEXTRANS .....	91
4.6.1	<i>Dextran binding to the silane layer via amide bonds</i> .....	91

4.6.2	<i>Deactivation of remained NHS-ester groups of the silane layer by ethanolamine.....</i>	<i>96</i>
4.6.3	<i>Overall amount of formed amide bonds produced by both dextran and ethanolamine.....</i>	<i>98</i>
4.6.4	<i>Bovine Serum Albumin (BSA) adsorption on dextran coated silane layer.....</i>	<i>101</i>
4.7	POSSIBLE EXPERIMENTAL PROBLEMS.....	103
4.7.1	<i>Solvent (toluene) contamination by water and molecular sieve beads .....</i>	<i>103</i>
4.7.2	<i>Silane layer preparation on the Ge MIRE catalyzed by nanoparticles of molecular sieve.....</i>	<i>106</i>
4.7.3	<i>Different types of toluene incompensation between reference and sample cuvettes.....</i>	<i>111</i>
4.7.4	<i>Silane layer preparation on the CdTe MIRE.....</i>	<i>113</i>
<b>CHAPTER 5</b>	<b>CONCLUSIONS .....</b>	<b>115</b>
<b>CHAPTER 6</b>	<b>APPENDIX .....</b>	<b>119</b>
6.1	MECHANISM OF OZONIZATION.....	119
6.2	MECHANISM OF AMIDE BOND FORMATION.....	120
6.3	DETERMINATION OF INTEGRATED MOLAR ABSORPTION COEFFICIENTS OF CHARACTERISTIC BANDS OF 7-OTCS .....	122
6.4	DETERMINATION OF INTEGRATED MOLAR ABSORPTION COEFFICIENTS OF SODIUM ACETATE BANDS .....	124
6.5	DETERMINATION OF INTEGRATED MOLAR ABSORPTION COEFFICIENTS OF AMIDE I' IN D <sub>2</sub> O BY 2-ACETAMIDO-2-DEOXY-D-GLUCOSE .....	126
6.6	OXIDIZED SILANE LAYERS.....	128
	References .....	130

## Chapter 1 *GENERAL INTRODUCTION*

### 1.1 Historical overview of organic thin films

Organic thin films have attracted considerable attention over the last years, although the subject has fairly old roots [1]. Even *the Babylonians* used to spread droplets of oil randomly onto water surfaces and by studying the behaviour of these thin films they made predictions about the future [2]. In 1774 *Benjamin Franklin* observed the calming influence of oil on water surfaces [3]. This experiment was followed roughly one hundred years later by *Lord Rayleigh's* (John William Strutt) conclusion that maximum oil film extension is representative of a layer one molecule thick. At about the same time, in the 19<sup>th</sup> century, *Agnes Pockels* prepared monolayers at the air-water interface [4]. Monolayers of amphiphilic molecules on the water surface and their behaviour at the liquid and gas interface was performed by *Irving Langmuir* at General Electric during the early part of the 20<sup>th</sup> century [5]. Langmuir films were used by *Katharine Blodgett* in the thirties to deposit multilayers of long chain carboxylic acids onto various solid substrates such as glass, chromium, brass, steel and silver surfaces [6]. Such films are referred to as Langmuir-Blodgett (LB) films. Recent additions to the family of molecular films are Self-Assembled Mono- and Multi-layers (SAMs) [7]. Systematic research on monomolecular layers adsorbed on metal surfaces was performed by Zisman [8] and Blackman and Dewar [9]. Netzer and Sagiv introduced covalently self-assembled silane films in 1983 [10]. Nuzzo and Allara showed adsorption of thiols from dilute solutions on gold surface [11]. Interest in these films has tremendously increased since that time, and the development and application of surface sensitive experimental techniques have resulted in an improved understanding of the film structure and growth process [12]. A general introduction of ultra thin self-assembled films is given in Ulman's book [13].

## 1.2 Definition of Self-Assembled Mono- and Multi-layer (SAM) films

The term “Self-Assembled Mono- and Multi-layers” has been widely used in the literature [14]. Therefore, it is important to define its meaning.

For a film of adsorbed material to be classified as a self-assembled the following conditions must be full filled:

- ❖ Thickness of the film must correspond to a single molecular thickness multiplied by the number of the layers.
- ❖ Film must be continuous. If material is not continuous but is only present in clumps or islands then it cannot be considered as a film.
- ❖ Adsorbed material must be chemically bound to the surface. The energy of chemisorption is important in the formation of self-assembled films and physisorbed material does not fall under this definition.
- ❖ Formation of a monolayer must be self-limiting in the presence of reagent excess. When the structure reaches a dense state, the deposition of material should stop with the formation of a single layer. On the other side, the formation of a multilayer is not self-limiting due to polymerization of adsorbate molecules. After monolayer formation adsorbate can no longer reach the substrate surface to react but molecules will be still added to the formed film resulting in reaction time prolongation and addition of a new layer.
- ❖ The film must be well ordered. The nature of the adsorbate-adsorbate interactions aids the formation of the film structure. As the density of adsorbates increases neighbouring molecules align themselves to maximize the Van der Waals interactions between hydrocarbon chains. Without the influence of these forces the result would likely be an amorphous rather than a well-ordered surface film.

It makes more sense to denote these specific structures as “Self-Assembled Films”. Therefore, self-assembled films are molecular assemblies that are formed spontaneously by adsorption of a surfactant with a specific affinity of its head-group to a substrate.

### 1.3 Structure and variety of SAM films

In a general sense, SAM films consist of three units (Figure 1):

- ❖ a surface-active head group which binds strongly to the substrate (alkoxy, acyloxy, halogen or amine group)
- ❖ a specific functional tail group that constitutes the outer surface of the film and modifies surface properties (vinyl, chloromethyl, primary amine, epoxy, methacrylate group) and
- ❖ a chain or backbone that connects the head and tail groups. [15]

All molecules will not self-organize on all substrates. Therefore, the affinity between the molecule and the surface is an important factor.

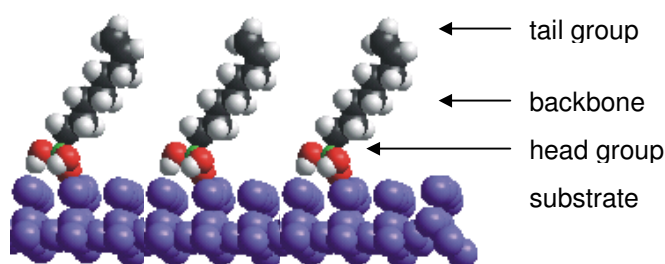


Figure 1. Structure of SAM films.

It is well known that organization and structure of SAM films are the result of the substrate-adsorbate interactions, the non-bonded interactions between adsorbates (electrostatic and Van der Waals forces), and the intramolecular interactions such as bond stretches, angle bends and torsions. Tail groups can also affect the film structure significantly providing a strong polar characteristic. The flexibility to design these films with various functional tail groups to accomplish desired surface properties and to control the structure in the nanometer regime is an attractive feature of self-assembled films [15].

There are several different types of SAM films given below [16].

- ❖ *Monolayers of fatty acids* are produced by spontaneous adsorption of long-chain *n*-alkanoic acids ( $C_nH_{2n+1}COOH$ ) on aluminium oxide and silver. This is an acid-base reaction and the driving force is the formation of a surface salt between the carboxylate anion and a surface metal cation. [17]
- ❖ *Monolayers of organosilicon derivatives* such as alkylchlorosilanes, alkylalkoxysilanes and alkylaminosilanes formed on the hydroxylated

substrates, e.g. silicon dioxide, aluminium oxide, quartz, glass, mica, zinc selenide, germanium oxide and gold. The driving force for these self-assemblies is the formation of polysiloxane network connected to the surface hydroxyl groups (-MOH) via M-O-Si bonds.

- ❖ *Organosulfur adsorbates* on metal and semiconductor surfaces such as alkanethiolates on Au(111) as well as thiophenols, thiocarbaminates and mercaptopyridines.
- ❖ *Organophosphonates and organophosphates* monolayers. An organophosphates has four oxygens with an alkyl group connected via a phosphoester bond. Phosphonates have three oxygens with a carbon attached directly to phosphorus. The lack of a hydrolysable P-O-C linkage makes phosphonate compounds more stable in aqueous solutions and easier to make SAMs than organophosphate compounds. [18]

#### 1.4 Structure of the SAM films produced by alkylchlorosilanes

The general formula of a silane coupling reagent,  $R-(CH_2)_n-Si-X_3$ , typically shows two classes of functionality, R and  $X_3$ . The group R is a non-hydrolysable organic radical that in a case of alkylchlorosilane molecules possesses a functionality such as vinyl group that imparts desired characteristics while the group X is a hydrolysable chlorine group. Following hydrolysis a reactive silanol group (Si-OH) is formed which can condense with other silanol groups present in a system to form siloxane linkages (Si-O-Si). [15]

##### 1.4.1 Selecting a silane coupling reagent

Factors influencing selection of silane coupling reagent include [19]:

- ❖ concentration and stability of surface hydroxyl groups
- ❖ physical and chemical features of silane coupling reagents
- ❖ stability of formed bonds between surface hydroxyl groups and silane coupling reagent.

Coupling between silane molecules and substrate is maximized when maximum number of substrate reactive centres exists. Hydroxyl groups covering the substrate vary widely in concentration. Freshly prepared substrates stored under neutral conditions have a minimum number of hydroxyl groups. Hydrolytically derived oxides



aged in moist air have significant amount of physically adsorbed water which can interfere with coupling. [19]

An important factor in controlling the effectiveness and properties of a coupled system is the linker between the organic functionality and the silicon atom. The linker length imposes a number of physical properties and reactivity limitations. The desirability of maintaining the reactive centres close to the substrate are most important in sensor applications, heterogeneous catalysis, fluorescent materials and composite systems in which the interfacing components are closely matched in modulus. On the other hand if the linker length is long, the functional group has greater mobility and can extend further from the inorganic substrate. This has important consequences if the functional group is expected to react with a single component in multi-component organic or aqueous phases found in homogeneous and phase transfer catalysis, biological diagnostics or liquid chromatography.

#### 1.4.2 Methods of applying silane coupling reagents

The structure and properties of the silane layer on an inorganic substrate depend not only on the functional groups attached to the silicon atom but also on the method used to bind silane molecule to the surface. Several different methods of applying silane coupling reagents are listed below [20].

- ❖ *Aqueous solutions.* From dilute solutions in pure water or in mixtures of water and polar solvents like alcohols. This method is used in industrial processes for environmental reasons.
- ❖ *Organic solutions.* From dilute solutions in dry organic solvents in order to avoid condensation of silane molecules as much as possible.
- ❖ *Vapour phase.* Volatile silanes can be applied to inorganic surfaces from vapour phase under a certain pressure.

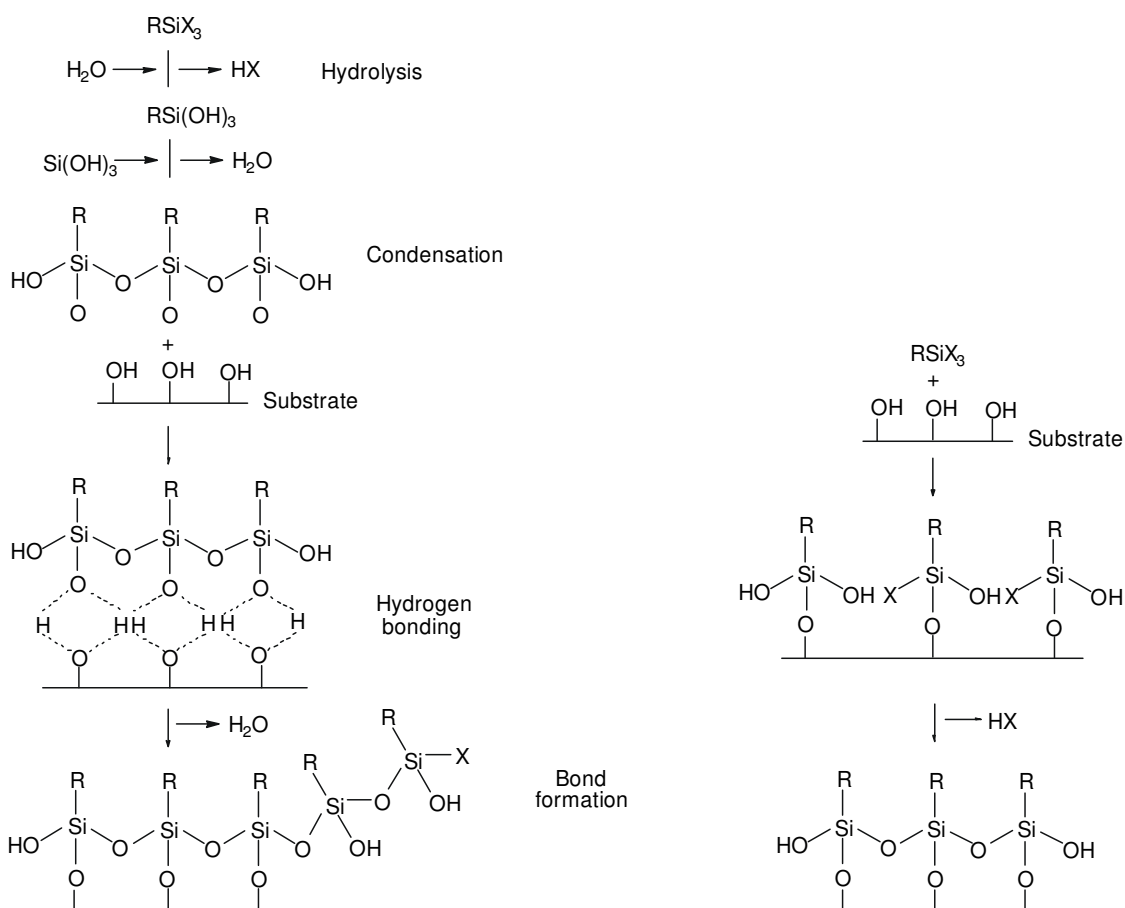
The external parameters that influence silanization reaction are certainly temperature and solution concentration. Various molecular features such as stiffness and length of the backbone or type of the end group also have an influence on the growth and the structure but these are rather intrinsic parameters inherent to a specific SAM system.

### 1.4.3 Formation of SAM films

Most of the widely used organosilanes have one organic substituent and three hydrolysable substituents. Formation of SAM films from solution involves three steps. The first step is hydrolysis of the three labile groups. Water needed for hydrolysis may come from several sources. It may be added and hydrolysis occurs immediately in the solution enabling condensation of silane molecules (Scheme 1, left) which can further form hydrogen bonds with OH groups of the substrate. On the other hand, if solution is very dry hydrolysis in solution will not occur. In that case, water needed for hydrolysis must be present on the substrate surface. Hydrolyzation occurs directly above the surface with direct binding of silane molecules to the surface (Scheme 1, right). After hydrolyzation, the next step is condensation between already bound silane molecules on the surface to oligomers, as well as vertical polymerization. Degree of polymerization is determined by the amount of available water and the organic substituent. Finally during drying or curing a covalent linkage with the substrate is formed with concomitant loss of water. [19]

Although described sequentially, these reactions can occur simultaneously after the initial hydrolyzation step. At the interface there is usually only one formed bond between each silicon atom of the organosilane molecule and the substrate surface. Two remaining silanol groups are present either in condensed or hydrolyzed form. The non-hydrolysable organic group remains available for covalent reaction or physical interaction with other phases. [19]

The ideal case would be monolayer formation between the coupling reagent and the surface where one of the hydrolyzable groups has reacted with surface hydroxyl group and two remaining hydrolysable groups with hydrolysable groups of neighbouring silane molecules. The ideal reaction is sketched in Scheme 1, right. In practice this case is very seldom.



Scheme 1. Two types of silanization reaction on an inorganic surface. Redrawn from ref. [20].

## 1.5 Review of experimental techniques

Many different thin film characterization techniques have been applied to SAM films.

- ❖ The first experiment one did on monolayers was the *Contact Angle Measurement* [13,21] for determination of the surface energies and wetting behaviour.
- ❖ To measure the thickness of the films *Ellipsometry* [22] is generally used.
- ❖ The surface morphology of the monolayers can be obtained from *Atomic Force Microscopy (AFM)* [23], *Scanning Tunneling Microscopy (STM)* [24], and *Environmental Scanning Electron Microscopy (ESEM)* [25].
- ❖ *Diffraction-based techniques* have been used for studying the 2D structure of SAM films such as *Low-Energy Electron Diffraction (LEED)* [26,27], *Grazing Incidence X-ray Diffraction (GIXD)* [28,29], and *Low-Energy Atom Diffraction (LEAD)* [30,31]. *X-ray reflectivity (XR)* [32,33] provides information on the electron density profile along the surface normal, i.e. film thicknesses,

roughness and electron densities. *Helium Atom Reflectivity (HAR)* [30] gives information on the roughness only of the outermost surface but is extremely sensitive to small changes like the adsorption of a small number of molecules.

- ❖ Various *Spectroscopy-based techniques* different in nature and energy scale can be exploited to deduce information on the structure and the growth:
  - \* Infrared (IR) spectroscopy [25,34,35,36,37,38,39]
  - \* Surface-Enhanced Raman Scattering (SERS) [34]
  - \* High-Resolution Electron Energy Loss Spectroscopy (HREELS) [26,40]
  - \* Near-Edge X-ray Absorption Fine Structure (NEXAFS) spectroscopy [41]
  - \* X-ray Photoelectron Spectroscopy (XPS) [34]

It is important to note that while the diffraction- and the spectroscopy-based methods are both spatially averaging, the average is performed over different regions with different weight. For instance, if the molecular tilt angle is determined by IR, the average is performed over all molecular chains including the disordered regions like grain boundaries, defect sites, etc., and also over molecules which are only physisorbed in a precursor layer. In contrast, the determination of the tilt angle by GIXD includes only the ordered (crystalline) regions. This is important when results from different techniques are compared.

## 1.6 Some of the SAM film characterization difficulties

❖ *Differences in the analytical methods* [1]. An important point is the difference in the analytical methods, i.e. their sensitivity to different features. X-ray Reflectivity (XR) is sensitive to the thickness and the density. Atomic Force Microscopy (AFM) is sensitive to the local structure and can detect the difference between layer and substrate or standing-up and lying-down molecules. Spectroscopic techniques (like IR) typically average over macroscopic lengths and are often particularly sensitive to the tilt angle of the molecular backbone. They detect molecules in disordered as well as in ordered areas (which can lead to an effectively decreased overall tilt angle), whether they are strongly attached to the substrate or not. When comparing results from different groups also the sensitivity to the preparation conditions and the environment has to be taken into account.

❖ *Ex situ vs. in situ*. There are different *ex situ* rinsing procedures already established for the investigation of SAM films. *Ex situ* the partially formed film might

“dry out” and the molecules might “fall over”. It is more efficient to investigate the growth *in situ*, i.e. in solution without taking the substrate out for the measurement. It was proposed that the solvent molecules help to keep the adsorbed molecules vertical and that rinsing causes some of molecules to be removed from the film, creating free volume, which enables molecules to tilt over thereby lowering the thickness [42].

❖ *Temperature dependence of the growth.* It was found that the critical temperature  $T_c$  for *n*-alkyltrichlorosilane monolayers on oxidized silicon is 28 °C [43]. Furthermore, this threshold temperature is found to exhibit a systematic increase with increasing of chain length. It was concluded that films prepared below  $T_c$  exhibit a heterogeneous structure with closely spaced islands of densely packed, nearly all-trans alkyl chains arranged almost vertical to the surface [44]. In contrast, films prepared at above  $T_c$  exhibit monotonically diminishing coverage with increasing preparation temperature and the alkyl chains increasingly assume higher contents of conformational disorder.

❖ *Water content in solution and cleanliness.* Since the presence of a water layer at the interface plays an important role for the growth of the SAM, it is not surprising that the water content in solution needs to be carefully controlled. In a case of alkylmethoxysilanes insufficient water concentration disables complete layer formation whereas in a case of alkylchlorosilanes water excess facilitates polymerization in solution. It was reported that increasing water content or also increasing age of the solution favours island-type growth more strongly [45]. Since the growth of silane-based SAM films is so sensitive to the level of moisture, which on the other hand is difficult to control precisely, this is one source of problems in the comparability of results from different groups.

## 1.7 Importance of SAM films

SAM films possessing different physical, chemical and electrical properties depending on their structure and composition may provide formation of molecular structures with known spacing, orientation and thickness. [46,47] Not mentioning their importance as model systems to study self-organization, intermolecular interactions and molecular-substrate interactions [48,49], SAM films have found applications in a wide range of fields, e.g. biomaterials [50] and biosensors [51],

nonlinear optical devices [52,53], HPLC [54], nanolithography [55], a variety of heterogeneous phenomena including catalysis [56], corrosion [57], lubrication [58], adhesion [59], and dispersion and deagglomeration of nanoparticles [60]. Different applications utilize different properties of the SAM films. The numerous existing and potential applications of films are summarized in the following three categories:

❖ *Applications that utilize the physical properties of SAM films.* SAM films can completely change wetting and frictional properties of the substrate. By the terminal groups of the organic molecules such as  $\text{CH}_3$ ,  $\text{OH}$ ,  $\text{NH}_2$  and  $\text{COOH}$  one can tailor the surface energy to different requirements. [61] Silanized surfaces have already found applications in gas and liquid chromatography.

❖ *Applications that utilize the chemical properties of SAM films.* SAM films that consist of long chain alkanes can be compact and chemically inert. This makes it difficult for chemical reagents to penetrate and react with the substrate surface. Films can serve as corrosion protection layers on metal and semiconductor surfaces. Siloxane films were demonstrated to be high resolution etching masks for microelectronics fabrication [62,63,64]. The area covered with siloxane remained inert while the bare silicon substrate was etched selectively. Similarly, SAM films can serve as templates for area-selective deposition on metals and other materials [65,66,67,68]. One can tailor the interaction between the films and other molecules or particles by modifying the terminal groups on films. Existing applications include modifying the biomaterial interface to control proteins [69]. Functionalized SAM films are also used as model system of biological surfaces [70]. Inspired by the capability of biological membranes to recognize specific chemical and biological stimuli and to convert them to measurable signals, researchers are trying to build chemical and biological sensor devices based on SAM films [71].

❖ *Applications that utilize the electrical properties of SAM films.* SAM films have different electrical characteristics such as conductivity, dielectric constant and capacitance. The flexibility of the electrical characteristics lies in the degree of conjugation, polarisability and dipole moment of the molecules and structure of the monolayers [72]. SAM films on semiconductor surfaces show promising potential as ultra-thin gate insulating layers in microelectronics [73]. In addition, SAM films are widely anticipated to be the building blocks of molecular electronics [74].

## 1.8 Biomolecule immobilization on SAM films

Nowadays the development of new biomaterials is based on SAMs. In biological surface science, as the broad interdisciplinary area, properties and processes at interface between synthetic materials and biological environments are investigated and new SAM surfaces are fabricated. [75] Self-assembled monolayers have attracted considerable attention as surface-active materials due to their specific binding properties and minimal background interference. [51] The chemically controlled modified SAM surfaces play an important role in dental and orthopaedic application, drug delivery, biosensors, bioreactors and many diagnostic techniques. [76,77,78]

Biomimetic surfaces can be prepared by chemisorption of sugar polymers onto modified silane surfaces. Sugar polymers are of enormous diversity and widely distributed in different organisms and cell types. They have multiple roles in pathogen detection, immunity and cell-cell interactions. Dextran belongs to a group of sugar polymers that evolved mainly to benefit a narrow range of microbial species. Dextran is a collective name for high-molecular-weight polymers composed of D-glucose units connected with  $\alpha$ -1,6 linkages and various amounts of side branches linked with  $\alpha$ -1,2,  $\alpha$ -1,3, or  $\alpha$ -1,4 to the main chains. Due to diverse branching of the glucose backbone chain, dextran polymers have a remarkable diversity in chain length and in physicochemical properties. [79]

The advantages of processed dextrans for biomedical applications are the biocompatibility, slow biodegradability and feasibility of incorporation of molecules into the matrices formed by dextrans. [79] Since dextranase, the enzyme that degrades dextran, is produced by bacteria and not by tissues, dextran coatings or implants will not degrade enzymatically in most tissues. Enzymatic degradation will only occur in tissues that have significant microbial populations, e.g. gastrointestinal and nasal tracts. Surface-immobilised dextran may be quite stable in most tissue environments as recent studies have shown that surface-immobilised dextran is resistant to dextranase-mediated degradation. [80]

### 1.8.1 Biosensors and biochips for diagnostic

To allow controlled release of pharmaceutical agents from a medical device, polymeric matrices that can be used to coat or impregnate implants and in which

therapies can be incorporated are required. The initial selection criteria for such a polymeric matrix is its non-toxicity to the biological environment in which it is intended to function. In addition, a matrix that can slowly be degraded is of a great interest since it can potentially allow for the continuous release of drugs. Because hydrogels are hydrophilic and their physical properties resemble those of biological tissues, they are appealing materials for use in the biological environment. Moreover, hydrogels made from natural polymers are biodegradable. The synthesis of hydrogels from proteins or saccharides is presented in a variety of research articles. Saccharides are readily available and can be degraded by hydrolysis or enzymatically in certain cases. They possess hydroxy-functional groups that can be used for the chemical modifications leading to crosslinking and the formation of hydrogels. These hydroxyl groups can also be used for to the covalent attachment of drugs or other therapies to the hydrogel backbone. [81]

### **1.8.2 Medical implants in the human body**

If a biomedical material is implanted into a living tissue, a cascade of host reactions occur at the interface between the tissue and the material known as an inflammatory response. This inflammatory response ends in an “encapsulation” of the material which means the development of a scar tissue surrounding the biomaterial. Immediately upon implantation, biomaterial substrates become coated with serum or plasma proteins such as albumin. Albumin, the most abundant protein, adsorbs first but is displaced by larger proteins that interact more favorably with the underlying substrate, a process known as the Vroman effect [82]. These adsorbed proteins are unable to maintain their native structures and in turn will cause adverse reactions such as the formation of fibrous capsules adjacent to soft tissue implants or blood clots inside synthetic vascular grafts. Protein fouling of biomaterials also renders biomaterials susceptible to colonization and infection by bacteria. Until recently, the adsorption and accumulation of biological material on implanted biomaterial surfaces have been irreversible and uncontrollable. Recent advances in biomaterial design, however, have reduced undesirable protein adsorption and unfavorable cell adhesion onto the materials. Biomaterial development has focused on creating adhesion-resistant interfaces as a solution to protein fouling, bacterial infections and adverse physiological reactions. Most protein-resistant polymeric biomaterials and coatings include poly(ethylene glycol) (PEG), poly-(ethylene oxide) (PEO) and their



derivatives. An alternative materials to PEG are chitin and dextran. Recent studies show that dextran-coated biomaterial surfaces provide low protein binding and anticellular adhesion comparable to PEG. [80,83] The advantage to using dextran-coated surfaces is that dextran provides multiple reactive sites for immobilization of biologically active molecules.

## Chapter 2 ATR FTIR SPECTROSCOPY

FTIR ATR spectroscopy represents a sensitive method for *in situ* investigations of processes at or near a surface. Particularly when thin layers are investigated with respect to the surface concentration and molecular structure, very sensitive techniques have to be applied in order to achieve an adequate signal-to-noise ratio. Information about the functional groups of molecules, their quantity and their spatial orientation can be obtained with the help of the measured ATR FTIR spectra. Even additives and impurities of small amounts can be detected. [84]

### 2.1 The principle of total internal reflection

The theory of reflection and transmission of an electromagnetic wave by a plane boundary was first derived by Fresnel. The geometry of specular reflection and transmission is depicted in Figure 2.

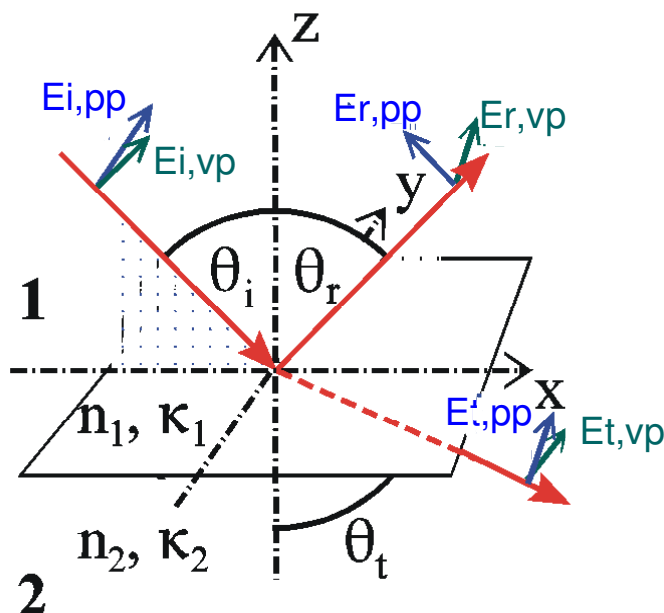


Figure 2. Specular reflection and transmission. The angles of incidence (i), reflection (r) and refraction (t) are denoted by  $\theta_i$ ,  $\theta_r$  and  $\theta_t$ , respectively. The corresponding electric field components are denoted by E. They are split into orthogonal portions, one parallel to the plane of incidence (x,z-plane) and the other perpendicular to this plane (parallel to y-axis). Accordingly, electric fields are referred to as parallel (pp) and perpendicular (vp) polarised;  $n_1$ ,  $n_2$ ,  $\kappa_1$  and  $\kappa_2$  denote the refractive and absorption indices in the two media.

Internal reflection can only occur when the angle of the refracted beam  $\theta_t$  is larger than the angle of incidence  $\theta_i$  (Figure 2). This means, according to Snell's law ( $n_1 \sin \theta_i = n_2 \sin \theta_t$ ), that the refractive index of rare medium 2 must be smaller than that of optically dense medium 1 ( $n_2 < n_1$ ).

The region of total reflection begins when the angle of refraction reaches  $90^\circ$ , i.e. at *the critical angle of incidence*  $\theta_c$ . It follows from Snell's law of refraction that

$$\begin{aligned} \theta_t = 90^\circ &\Rightarrow \text{then } \theta_i = \theta_c \\ \sin \theta_c &= \frac{n_2}{n_1} = n_{21} \end{aligned} \quad (1)$$

Under these conditions, interference of the incident and reflected electric field at the interface generates a standing wave, i.e. *evanescent wave* beyond the reflecting interface in the rare medium (Figure 3).

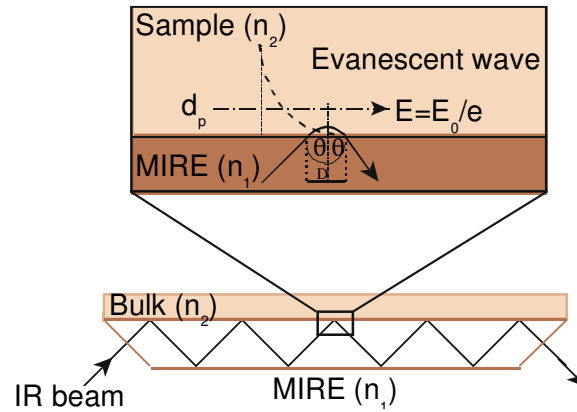


Figure 3. The principle of total internal reflection.

An electromagnetic wave propagates from medium 1 (MIRE) into a nonabsorbing medium 2 under the conditions of total reflection [85] and generates *an evanescent field* in the rare medium:

$$E_{pp/vp}^r(z) = E_{pp/vp}^r(0) \cdot e^{\left(-\frac{z}{d_p}\right)} \quad (2)$$

where  $E_{pp/vp}^r(0)$  denotes the relative electric field strength at the interface ( $z=0$ ). The relative electric field components in the rarer medium 2 and at the interface  $z=0$ ,  $E_{pp/vp}^r(z)$  and  $E_{pp/vp}^r(0)$ , represent the ratio between the electric field components  $E_{0x,2}, E_{0z,2}, E_{0y,2}$  and  $E_{0pp,1}, E_{0vp,1}$  given by Fresnel's equations (see next Section 2.1.1). [86]

The distance from the interface where  $E_{pp/vp}^r(z)$  drops to a value  $1/e$  of  $E_{pp/vp}^r(0)$  is called *the penetration depth*  $d_p[m]$  given by eq. (3):

$$d_p = \frac{\lambda/n_1}{2\pi\sqrt{\sin^2 \theta_i - n_{21}^2}} = \frac{1}{2\pi \cdot \tilde{\nu} \cdot \sqrt{n_1^2 \sin^2 \theta_i - n_2^2}} \quad (3)$$

Here  $n_{21}$  stands for the ratio  $n_2/n_1$  of the refractive indices of the rarer medium ( $n_2$ ) and of the internal reflection element ( $n_1$ );  $\lambda_1 = \lambda_{\text{vacuum}}/n_1$ ;  $\theta_i$  is the angle of incidence. This distance amounts to the order of magnitude of the wavelength  $\lambda_1$  of the infrared radiation, varying between a fraction of a micron and a few microns depending on the refractive indices of the MIRE (e.g.  $n_{\text{Ge}}=4.0$ ,  $n_{\text{ZnSe}}=2.4$ ) and the medium 2 ( $n_2 \approx 1.5$  for organic materials) as well as the angle of incidence. According to eq. (3) the penetration depth is wavelength dependent (Figure 4).

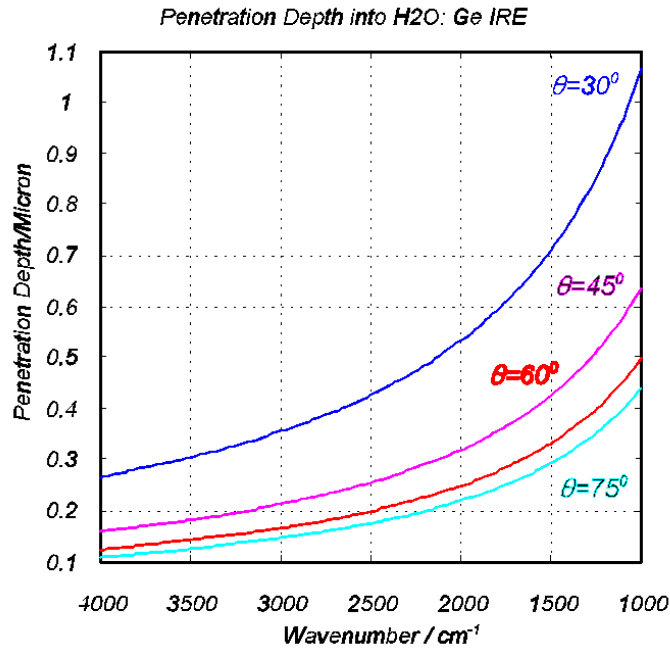


Figure 4. Penetration depth dependence on wavenumber for Ge MIRE in H<sub>2</sub>O at different angles of incidence.

The displacement  $D$ , the so-called “Goos-Hänchen shift” [87], represents a displacement of the incident and reflected waves. The displacement is equal to a fraction of a wavelength and proportional to the penetration depth. The “evanescent field” exhibits another interesting feature, namely the existence of electric field components along all three axes of the rectangular coordinate system attached to the ATR plate, interacting with transition dipoles in all orientations. Transition dipoles will absorb energy in internal reflection regardless of their orientation while in

transmission only dipoles oriented parallel to the direction of propagation can absorb energy. In contrast, the incident plane wave has only electric field components in the plane perpendicular to the direction of propagation. By means of polarizer, two selected directions of the incident electric field vector may be chosen, namely parallel (pp) and perpendicular (vp) to the plane of incidence.

### 2.1.1 Relative electric field components

Figure 5 shows the MIRE fixed coordinate system which is relevant for the description of optical and structural features of the system [88].

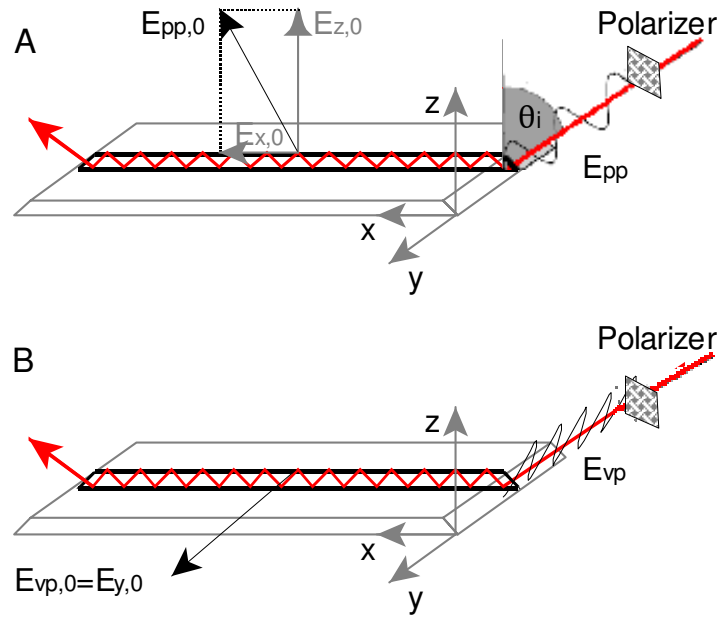


Figure 5. Schematic presentation of attenuated total reflection (ATR) in multiple reflection mode. For easier recognition, the plane of incidence is drawn in a bold black line than the rest of the ATR crystal. (A) Infrared light polarized parallel to the plane of incidence contributes to the transverse magnetic TM wave that can interact with the x- and z-components of the transition dipole moment of the sample, i. e.  $M_x$  and  $M_z$ . (B) The transverse electric TE wave that only excites the y-component of the dipole moment,  $M_y$ , consists of infrared light polarized perpendicular to the plane of incidence.  $\theta_i$ , angle of incidence;  $E_{pp}$  and  $E_{vp}$ , parallel and perpendicular components of the electric field of incident light;  $E_{pp,0}$  and  $E_{vp,0}$ , parallel and perpendicular polarized components of the electric field of the evanescent wave;  $E_{x,0}$ ,  $E_{y,0}$ ,  $E_{z,0}$ , electric field components with respect to the plate fixed-coordinate system ( $E_{pp,0} \rightarrow E_{x,0}$ ,  $E_{z,0}$ ;  $E_{vp,0} \rightarrow E_{y,0}$ ). Redrawn and rewritten from ref. [89].

From Fresnel's equations, it follows that parallel component  $E_{pp,0}$  results in the  $E_{x,0}$  and  $E_{z,0}$  (Figure 5A) and perpendicular component  $E_{vp,0}$  in the  $E_{y,0}$  of the evanescent field (Figure 5B).

In a case of bulk rarer medium ( $n_2$ ) above ATR crystal ( $n_1$ ) the relative electric field components are given by:

$$\begin{aligned} E_{0x,2}^r &= \frac{E_{0x,2}}{E_{0pp,1}} = \frac{2\cos\theta(\sin^2\theta - n_{21}^2)^{1/2}}{(1 - n_{21}^2)^{1/2}[(1 + n_{21}^2)\sin^2\theta - n_{21}^2]^{1/2}} \\ E_{0z,2}^r &= \frac{E_{0z,2}}{E_{0pp,1}} = \frac{2\sin\theta\cos\theta}{(1 - n_{21}^2)^{1/2}[(1 + n_{21}^2)\sin^2\theta - n_{21}^2]^{1/2}} \\ E_{0y,2}^r &= \frac{E_{0y,2}}{E_{0vp,1}} = \frac{2\cos\theta}{(1 - n_{21}^2)^{1/2}} \end{aligned} \quad (4)$$

with  $E_{0pp,2}^r = \left(E_{0x,2}^r + E_{0z,2}^r\right)^{1/2}$  and  $E_{0vp,2}^r = E_{0y,2}^r$ .

The expressions in eqs. (4) hold exactly for nonabsorbing media 1 and 2 but are good approximations for weak absorbing samples.

In the case of a thin layer of refractive index  $n_2$  immobilized at the surface of the ATR crystal of refractive index  $n_1$ , the evanescent wave penetrates into the surrounding medium of refractive index  $n_3$ , too. As long as the layer thickness  $d$  is small compared to the penetration depth  $d_p$  the thin layer approximation leads to good result. This approximation is based on the assumption that the electric field in the rarer medium is determined by media 1 and 3. Thin film is considered to be a dielectric which is introduced into this field.

For thin immobilized film ( $n_2$ ) on ATR crystal ( $n_1$ ) in contact with bulk rarer medium ( $n_3$ ) one obtains

$$\begin{aligned} E_{0x,2}^r &= \frac{E_{0x,2}}{E_{0pp,1}} = \frac{2\cos\theta(\sin^2\theta - n_{31}^2)^{1/2}}{(1 - n_{31}^2)^{1/2}[(1 + n_{31}^2)\sin^2\theta - n_{31}^2]^{1/2}} \\ E_{0z,2}^r &= \frac{E_{0z,2}}{E_{0pp,1}} = \frac{2 \cdot n_{32}^2 \cdot \sin\theta\cos\theta}{(1 - n_{31}^2)^{1/2}[(1 + n_{31}^2)\sin^2\theta - n_{31}^2]^{1/2}} \\ E_{0y,2}^r &= \frac{E_{0y,2}}{E_{0vp,1}} = \frac{2\cos\theta}{(1 - n_{31}^2)^{1/2}} \end{aligned} \quad (5)$$

with  $E_{0pp,2}^r = \left(E_{0x,2}^{r^2} + E_{0z,2}^{r^2}\right)^{1/2}$  and  $E_{0vp,2}^r = E_{0y,2}^r$ .

It should be noted that generally  $E_{0x}^r$ ,  $E_{0y}^r$  and  $E_{0z}^r$  are not equal.

Equations are overtaken from ref. [88].

### 2.1.2 Effective thickness

Quantitative analysis in transmission spectroscopy is based the Lambert-Beer's law:

$$T = \frac{I}{I_0} = e^{-A} = e^{-\varepsilon \cdot c \cdot d} \quad (6)$$

where  $I_0$  is the incident intensity,  $I$  is the transmitted intensity,  $A = \varepsilon \cdot c \cdot d$  denotes the absorbance,  $\varepsilon$  molar absorption coefficient,  $c$  concentration,  $d$  sample thickness.

To apply Lambert-Beer's law to ATR data, one must introduce a hypothetical thickness  $d_e$  of a sample which would result in the same absorbance of a given band in a hypothetical transmission experiment as obtained with the real sample thickness  $d$  in the ATR experiment. The quantity  $d_e$  was introduced by Harrick [90] and referred to as "*effective thickness*".

For an isotropic layer extended from  $z = z_i$  to  $z = z_f$  ( $d = z_f - z_i$ ) one obtains:

$$d_{e,pp/vp}^{iso} = \frac{1}{\cos \theta_i} \cdot \frac{n_2}{n_1} \cdot \frac{d_p}{2} \cdot \left( e^{-\frac{2z_i}{d_p}} - e^{-\frac{2z_f}{d_p}} \right) \cdot E_{0,pp/vp}^{r^2} \quad (7)$$

$E_{0,pp/vp}^{r^2}$  denotes the square of the relative electric field strength in medium 2.

For an immobilized layer  $z_i=0$  (i.e.  $z_f=d$ ), one obtains

$$d_{e,pp/vp}^{iso} = \frac{1}{\cos \theta_i} \cdot \frac{n_2}{n_1} \cdot \frac{d_p}{2} \cdot \left( 1 - e^{-\frac{2d}{d_p}} \right) \cdot E_{0,pp/vp}^{r^2} \quad (8)$$

Two special cases should be mentioned: bulk case and thin film case (Figure 6).

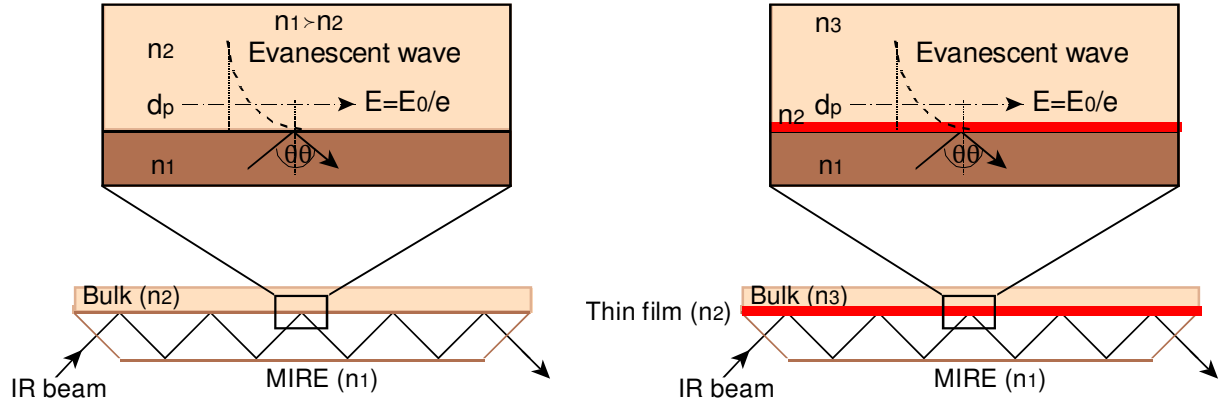


Figure 6. Schematic presentation of the ATR principle for a bulk medium (left) and a thin film (right).

❖ For a bulk medium the electric field amplitude falls to a very low value within the thickness of the rarer medium,  $d$ . The sample thickness is much bigger than the penetration depth, such that  $d \gg d_p$  (Figure 6, left).

In this case, for a bulk medium extended from  $z_i = 0$  to  $z_f = \infty$  eq. (7) results in

$$d_{e,pp/vp}^{b,iso} = \frac{1}{\cos \theta_i} \cdot \frac{n_2}{n_1} \cdot \frac{d_p}{2} \cdot E_{0,pp/vp}^2 \quad (9)$$

According to eq. (9)  $d_e$  turns out to be wavelength dependent via  $d_p$ . As a consequence, ATR spectra of bulk media generally show increasing intensity with increasing wavelength (decreasing wavenumber).

❖ When the thickness of a layer  $d = z_f - z_i$  is small compared to  $d_p$ , the electric field amplitude can be assumed to be a constant over the layer thickness (Figure 6, right). In that case, eq. (7) reduces by linearization of exponential part to eq. (10) which is independent of the wavelength. For  $z_i=0$  one obtains

$$d_{e,pp/vp}^{th,iso} = \frac{1}{\cos \theta_i} \cdot \frac{n_2}{n_1} \cdot d \cdot E_{0,pp/vp}^2 \quad (10)$$

The effective thickness for thin film is proportional to the actual film thickness,  $d$ .

### 2.1.3 Oriented samples

The intensity of the light absorption (i.e. integrated absorbance) is proportional to the square of the scalar product between the transition dipole moment  $\bar{M}$  of a given molecule and the electric field of radiation  $\bar{E}$  according to eq. (11):

$$I = \int A(\tilde{\nu}) d\tilde{\nu} = c \cdot d \cdot \int \epsilon(\tilde{\nu}) d\tilde{\nu} \approx (\bar{E} \cdot \bar{M})^2 \quad (11)$$

where



$$(\vec{E} \cdot \vec{M})^2 = |\vec{E}|^2 \cdot |\vec{M}|^2 \cdot \cos^2(\vec{E}, \vec{M}) = (E_x M_x + E_y M_y + E_z M_z)^2 \quad (12)$$

Eqs. (11) and (12) form the basis of orientation measurements.  $M_x$ ,  $M_y$ , and  $M_z$  denote the components of the transition dipole moment in the IRE fixed coordinate system shown in Figure 7.

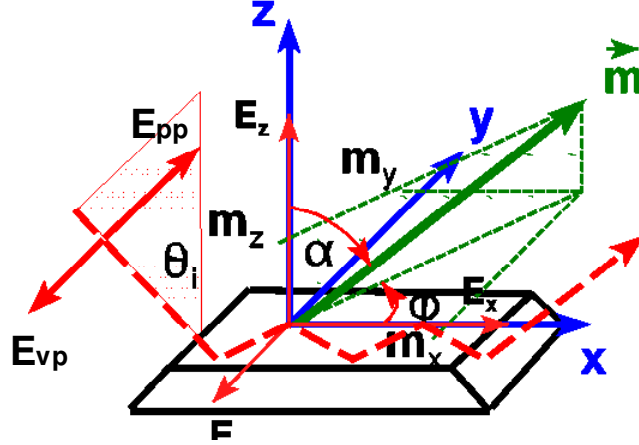


Figure 7. ATR set up. Optical and structural features are related to the IRE fixed coordinate system  $x, y, z$ .  $E_{pp}$  and  $E_{vp}$  denote the parallel and perpendicular polarized components of the light incident to the IRE under the angle  $\theta_i$ .  $E_{pp}$  results in the  $E_x$  and  $E_z$  components of the evanescent field, while  $E_{vp}$  results in the  $E_y$  component.  $\vec{m}$  denotes the unit vector in direction of the transition dipole moment vector of a given vibrational mode, and  $m_x$ ,  $m_y$ ,  $m_z$  are the corresponding components in the IRE coordinate system.  $\vec{m}$  goes off at an angle  $\alpha$  with respect to the  $z$ -axis and the projection of  $\vec{m}$  to the  $xy$ -plane goes off at an angle  $\phi$  with respect to the  $x$ -axis.

It is usual to work with dimensionless relative intensities instead of absolute intensities in order to get rid of physical and molecular constants, e.g. the magnitude of the transition moment. The so-called *dichroic ratio* is introduced as the absorbance ratio obtained from spectra measured with parallel and perpendicular polarized incident light, i.e.

$$R = \frac{\int A_{pp}(\tilde{\nu}) d\tilde{\nu}}{\int A_{vp}(\tilde{\nu}) d\tilde{\nu}} \quad (13)$$

In order to get information on the direction of the transition dipole moment  $\vec{M}$ , the scalar product notation using vector components (eq. (14)) will be used. Taking into account that parallel component of the evanescent field is represented by  $x$ - and  $z$ -

components, and perpendicular component by the y-component one obtains for the dichroic ratio:

$$R = \frac{E_x^r{}^2 m_x^2 + E_z^r{}^2 m_z^2 - 2E_x^r E_z^r m_x m_z}{E_y^r{}^2 m_y^2} \quad (14)$$

where  $E_{x,y,z}^r$  denote the relative electric field components;  $m_x$ ,  $m_y$ , and  $m_z$  are the unit vector components of  $\vec{M}$ . Eq. (14) holds for a single crystalline sample. In a complex non crystalline molecule there are generally many possibilities of molecular arrangements, conformational changes and fluctuations. The experimentally available quantity  $R$  is therefore an ensemble mean represented by:

$$R = \frac{E_x^r{}^2 \langle m_x^2 \rangle + E_z^r{}^2 \langle m_z^2 \rangle - 2E_x^r E_z^r \langle m_x m_z \rangle}{E_y^r{}^2 \langle m_y^2 \rangle} \quad (15)$$

Uniaxial orientation along the z-axis is often encountered in membrane spectroscopy. In this case  $\langle m_x m_z \rangle = 0$ , resulting in

$$R = \frac{E_x^r{}^2 \langle m_x^2 \rangle + E_z^r{}^2 \langle m_z^2 \rangle}{E_y^r{}^2 \langle m_y^2 \rangle} \quad (16)$$

The unit vector components as presented in Figure 7 are determined by the angles  $\alpha$  and  $\phi$ :

$$m_x = \sin \alpha \cos \phi$$

$$m_y = \sin \alpha \sin \phi$$

$$m_z = \cos \alpha$$

with corresponding mean squares

$$\begin{aligned} \langle m_x^2 \rangle &= \langle \sin^2 \alpha \cos^2 \phi \rangle = \frac{1}{2} \left( 1 - \langle \cos^2 \alpha \rangle \right) \\ \langle m_y^2 \rangle &= \langle \sin^2 \alpha \sin^2 \phi \rangle = \frac{1}{2} \left( 1 - \langle \cos^2 \alpha \rangle \right) \\ \langle m_z^2 \rangle &= \langle \cos^2 \alpha \rangle \end{aligned} \quad (17)$$

It should be noted that for an isotropic arrangement of transition moments the ensemble mean of any component of eq. (17) result in 1/3. As a consequence eq. (16) results in

$$R^{\text{iso}} = \frac{E_x^2 + E_z^2}{E_y^2} \quad (18)$$

which, according to eq. (5) differs from unity.  $R^{\text{iso}} = 1$  holds only for transmission spectroscopy.

Introducing eq. (17) into eq. (16) results in

$$R = \frac{E_x^2}{E_y^2} + 2 \frac{E_z^2}{E_y^2} \cdot \frac{\langle \cos^2 \alpha \rangle}{1 - \langle \cos^2 \alpha \rangle} \quad (19)$$

Solving eq. (19) for  $\langle \cos^2 \alpha \rangle$  results in

$$\langle \cos^2 \alpha \rangle = \frac{\left( R - \frac{E_x^2}{E_y^2} \right) \frac{E_y^2}{E_z^2}}{2 + \left( R - \frac{E_x^2}{E_y^2} \right) \frac{E_y^2}{E_z^2}} \quad (20)$$

This quantity is directly related to the segmental order parameter of the corresponding vibration (e.g. CH<sub>2</sub> stretch)  $S_{\text{seg}}(i)$ , which characterizes the partial alignment of the transition dipole moment  $\vec{M}_i$  with respect to the z-axis (Figure 8a) and which corresponds to the “bond-order” parameter encountered in nuclear magnetic resonance (NMR) spectroscopy.

$$S_{\text{seg}}(i) = \frac{3}{2} \langle \cos^2 \alpha \rangle - \frac{1}{2} \quad (21)$$

Perfect alignment along the z-axis would result in  $\langle \cos^2 \alpha \rangle = 1$  and  $S_{\text{seg},z} = 1$ , respectively. On the other hand, an isotropic arrangement of transition moments would result in the ensemble mean  $\langle \cos^2 \alpha \rangle = 1/3$  corresponding to  $S_{\text{seg,iso}} = 0$ . Finally, isotropic arrangement of the transition moments in the x,y-plane, i.e.  $\alpha = 90^\circ$ ,  $\langle \cos^2 \alpha \rangle = 0$  would result in  $S_{\text{seg,xy}} = -1/2$ . Both  $\langle \cos^2 \alpha \rangle$  and  $S_{\text{seg}}$  are experimentally accessible by polarized light measurements.

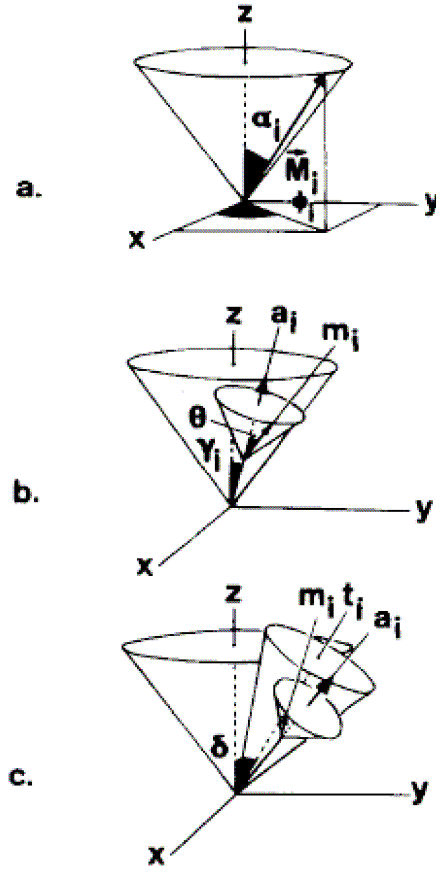


Figure 8. (a) Model for the calculation of  $S_{\text{seg}}(i)$ : uniaxial orientation of the  $i$ -th transition dipole moment vector  $\vec{M}_i$  around the  $z$ -axis; distribution function  $P(\phi_i) = 1$  (for details see ref. [91]). (b) Model for the derivation of  $S_{\text{mol}}(i)$  in the *liquid crystalline phase*: superposition of two uniaxial distributions. (c) Model for the derivation of  $S_{\text{mol}}(i)$  in the *gel phase*: superposition of three uniaxial distributions.  $m_i$ : instantaneous orientation of the transition dipole moment's unit vector.  $a_i$ : instantaneous orientation of the segmental molecular axis.  $t_i$ : tilted average orientation of the segmental molecular axis. Angles:  $\delta$ , tilt angle between  $z$ -axis and  $t_i$ ;  $\gamma_i$ , angle between  $z$ -axis and  $a_i$ ;  $\Theta$ , angle between  $a_i$  and  $m_i$ .

For the calculation of  $S_{\text{mol}}(i)$  from  $S_{\text{seg}}(i)$ , a superposition of two uniaxial orientations is assumed (Figure 8b):  $\vec{m}_i$  is oriented uniaxially around the segmental molecular axis  $a_i$  with the fixed angle  $\Theta$ . The segmental molecular axis  $a_i$  exhibits a uniaxial distribution with respect to the  $z$ -axis. The angle  $\gamma_i$  between the  $i$ -th segmental molecular axis and the  $z$ -axis is subjected to fluctuations. Thus, the spectroscopically relevant quantity is  $\langle \cos^2 \gamma_i \rangle$ . If the uniaxial distribution of a vector  $\vec{M}_i$  is the result of a superposition of different uniaxially oriented vectors, it follows that the order

parameter associated with the first vector can be split up into order-parameter-like factors which refer to the superposed uniaxially distributed vectors; that is,

$$S_{\text{seg}}(i) = \left( \frac{3}{2} \cos^2 \Theta - \frac{1}{2} \right) S_{\text{mol}}(i) \quad (22)$$

with

$$S_{\text{mol}}(i) = \frac{3}{2} \cos^2 \gamma_i - \frac{1}{2} \quad (23)$$

In the gel phase, model can be described by the product of three order-parameter-like terms since it can be visualized as a superposition of three uniaxially distributed components: the tilted average molecular axis is distributed uniaxially around the bilayer normal, the instantaneous molecular axis around the mean molecular axis, and the transition dipole moment around the instantaneous molecular axis (Figure 8c):

$$S_{\text{CH}_2}(i) = \left( \frac{3}{2} \cos^2 \Theta - \frac{1}{2} \right) \left( \frac{3}{2} \cos^2 \delta - \frac{1}{2} \right) S_{\text{mol}}(i) \quad (24)$$

Equations (21) and (24) can be applied in the liquid crystalline phase and in the gel phase, respectively. In the case of  $\delta = 0^\circ$  (liquid crystalline phase or zero chain tilt in the gel phase), eq. (24) converts to eq. (21). In both cases,  $S_{\text{mol}}(i)$  is a measure of the extent of the angular fluctuations of the  $i$ -th segmental molecular axis around its nontilted (or tilted) average orientation.

#### 2.1.4 The surface concentration

The concept of effective thickness is maintained also for oriented samples. However, one has to take into account that the effective thickness may become zero (no absorbance) if the angle between the transition dipole moment  $\bar{M}$  and the electric field vector  $\bar{E}$  is  $90^\circ$ , and maximum for parallel alignment of the two vectors. Weighting is achieved by multiplying the axial effective thicknesses of isotropic samples  $d_{\text{ex,ey,ez}}^{\text{iso}}$  by factors depending on the ultrastructure of the sample (i.e. the corresponding ensemble mean of the unit vector components of the transition moment as introduced by eq. (17)) resulting in eqs. (25).

$$\begin{aligned}
d_{\text{ex}} &= 3 \langle m_x^2 \rangle d_{\text{ex}}^{\text{iso}} = \frac{3}{2} \left( 1 - \langle \cos^2 \alpha \rangle \right) d_{\text{ex}}^{\text{iso}} \\
d_{\text{ey}} &= 3 \langle m_y^2 \rangle d_{\text{ey}}^{\text{iso}} = \frac{3}{2} \left( 1 - \langle \cos^2 \alpha \rangle \right) d_{\text{ey}}^{\text{iso}} \\
d_{\text{ez}} &= 3 \langle m_z^2 \rangle d_{\text{ez}}^{\text{iso}} = 3 \langle \cos^2 \alpha \rangle d_{\text{ez}}^{\text{iso}}
\end{aligned} \tag{25}$$

The surface concentration  $\Gamma$  of a species in a layer may be understood as projection of the molecules in the volume concentration  $c$  defined by unit area and height  $d$  (real sample thickness). It follows from eqs. (6) and (25)

$$\Gamma = c \cdot d = \frac{A_{\text{pp/vp}} \cdot d}{\varepsilon \cdot d_{\text{e,pp/vp}}} = \frac{\int A_{\text{pp/vp}}(\tilde{\nu}) d\tilde{\nu} \cdot d}{\int \varepsilon(\tilde{\nu}) d\tilde{\nu} \cdot d_{\text{e,pp/vp}}} \tag{26}$$

$A_{\text{pp/vp}}$  denotes the absorbances measured with parallel and perpendicular polarized incident light, respectively;  $\int \varepsilon(\tilde{\nu}) d\tilde{\nu}$  is the decadic integrated molar absorption coefficient of the band;  $d_{\text{e,pp/vp}}$  denotes the effective thickness of the layer. It depends on the polarisation of incident light and on the structure of the layer. [91] With  $N$  active total reflections and  $\nu$  equal functional groups of a molecule, the surface concentration  $\Gamma$  may then be expressed as depending on the experimentally determined dichroic ratio  $R$  and the relative electric field strengths resulting from Fresnel's equations in

$$\Gamma = \frac{d \int A_{\text{pp/vp}}(\tilde{\nu}) d\tilde{\nu}}{3\nu \cdot N \cdot d_{\text{e,pp/vp}}^{\text{th,iso}} \int \varepsilon(\tilde{\nu}) d\tilde{\nu}} \left[ 2 - \frac{E_x^2}{E_z^2} + R \frac{E_y^2}{E_z^2} \right] \tag{27}$$

Accordingly to eq. (10), eq. (27) converts into eq. (28) in the case of a thin layer.

$$\Gamma = \frac{\int A_{\text{pp/vp}}(\tilde{\nu}) d\tilde{\nu}}{3\nu \cdot N \cdot d_{\text{e,pp/vp}}^{\text{rel,iso}} \int \varepsilon(\tilde{\nu}) d\tilde{\nu}} \left[ 2 - \frac{E_x^2}{E_z^2} + R \frac{E_y^2}{E_z^2} \right] \tag{28}$$

As a consequence, the surface concentration of a thin layer ( $d \ll d_p$ ) featuring uniaxial orientation along the  $z$  axis can be determined without knowing the real thickness  $d$  and its real structure. Structural information of the layer is contained in the experimentally determined dichroic ratio  $R$ .

Surface concentration equations are taken from ref. [39, 92].

### 2.1.5 Number of the internal reflection

The number of internal reflections  $N$  is calculated from simple geometrical considerations. The incident beam advances a distance ("skip distance") equal to  $t \times \tan \theta$  for each reflection. [90] If the MIRE length is  $l$ , the total number of reflections for a single pass plate is given by:

$$N = \frac{l}{t} \times \cot \theta \quad (29)$$

For single-pass plates,  $l$  is measured from the center of the entrance aperture to the center of the exit aperture, as shown in Figure 9.  $N$  is dependant on  $\theta$  and increases as the MIRE is made longer and thinner.

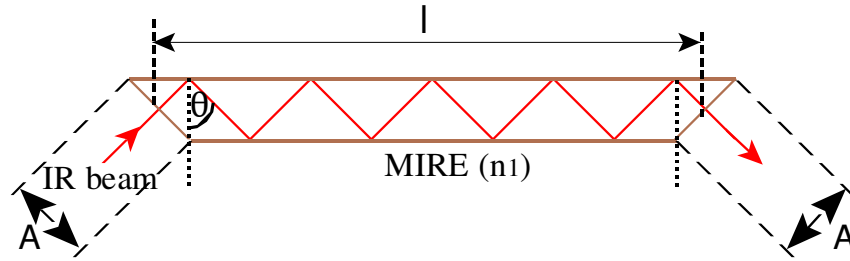


Figure 9. Single-pass MIRE defining aperture (A), length ( $l$ ) and angle of incidence ( $\theta$ ).

## 2.2 Theoretical background considerations

The ATR set-up enables the measurement of a thin layer in contact with solvent or reactive solution in the S cuvettes while the R cuvettes filled with pure solvent serve as reference. When thin layer and solvent have vibrational bands clearly resolved from each other, measured SBSR spectrum of a thin layer in solvent as well as a thin layer in reactive solution will always feature negative background incompenation.

In case of SBSR spectrum of thin layer in contact with solvent, background incompenation occurs due to solvent displacement by the attached layer. On the other side, background incompenation of time-resolved SBSR spectra of a layer growth in contact with reactive solution occurs not only due to reactive solution displacement by the growing layer but also because of solvent dilution by reactive solute molecules. Therefore, basic ATR theory has to be applied to both the SBSR spectrum of attached layer and the SBSR spectra of the growing layer.

The first problem related to the compensation of a thin layer in solvent results from the fact that the evanescent field penetrates proportionally to its wavelength into the rarer medium. As a consequence the SBSR measurement results in a wavelength dependent overcompensation of the background (solvent) due to its displacement by the growing layer. One has to take into account that the influence of the layer thickness is more prominent at high wavenumbers (small wavelengths).

Effective thickness for bulk (solvent) of refractive index  $n_3$  given by eq. (9) is converted into eq. (30) by replacing  $n_2$  by  $n_3$ .

$$d_{e,pp/vp}^{b,iso} = \frac{n_3}{n_1 \cos \theta} \cdot \frac{d_p}{2} \cdot E_{b,pp/vp}^{r2} \quad (30)$$

where  $d_p$  denotes the wavelength dependent penetration depth,  $E_{b,pp/vp}^r$  denotes the relative electric field strength in the bulk (b) rarer medium for parallel (pp) and perpendicular (vp) polarized incident light.

Effective thickness of a very thin ( $d \ll d_p$ ) isotropic surface layer (th) of thickness  $d$  and refractive index  $n_2$  given by eq. (10) is modified into eq. (31) by exchanging layer thickness  $d$  by  $d_0$ .

$$d_{e,pp/vp}^{th,iso} = \frac{n_2}{n_1 \cos \theta} \cdot d_0 \cdot E_{th,pp/vp}^{r2} \quad (31)$$



For adequate background compensation of the attached layer in the S cuvettes, the absorbance spectrum of the pure solvent measured in the R cuvettes ( $A^b$ ) has to be scaled by the factor  $\kappa_1$  to the range corresponding to the layer thickness and then added to the experimentally obtained absorbance spectrum of thin layer ( $A^{th}$ ), thus removing the wavelength dependent overcompensation.

$$A_{corr} = A^{th} + A^b \cdot \kappa_1 \quad (32)$$

The scaling factor  $\kappa_1$  representing the ratio between effective thicknesses of thin film and bulk medium (solvent) is given by eq. (33).

$$\kappa_1 = \frac{d_{e,pp/vp}^{th,iso}}{d_{e,pp/vp}^{b,iso}} = \frac{\frac{1}{\cos\theta} \cdot \frac{n_2}{n_1} \cdot d_0 \cdot E_{th,pp/vp}^2}{\frac{1}{\cos\theta} \cdot \frac{n_3}{n_1} \cdot \frac{d_p}{2} \cdot E_{b,pp/vp}^2} = \frac{2d_0}{d_p} = \frac{2d_0}{\frac{\lambda}{2\pi n_1 \sqrt{\sin^2\theta - \left(\frac{n_3}{n_1}\right)^2}}} \quad (33)$$

$$\kappa_1 = 4\pi \sqrt{n_1^2 \sin^2\theta - n_3^2} \cdot d_0 \cdot \tilde{\nu}$$

It should be noted that the electric fields in bulk and thin layer become the same and can be traced. The layer displaced solvent has the same refracted index as the bulk and therefore one has to set  $n_2=n_3$ .

The scaling factor  $\kappa_1$  is independent of the polarisation. For a layer thickness of  $d=13$  Å,  $n_1 = 4.0$  (Ge),  $n_3 = 1.49$  (toluene, bulk),  $\theta=45^\circ$  (angle of incidence), one obtains for  $\kappa_1$  as depending on the wavenumber  $\tilde{\nu}$  the following linear graph (Figure 10).

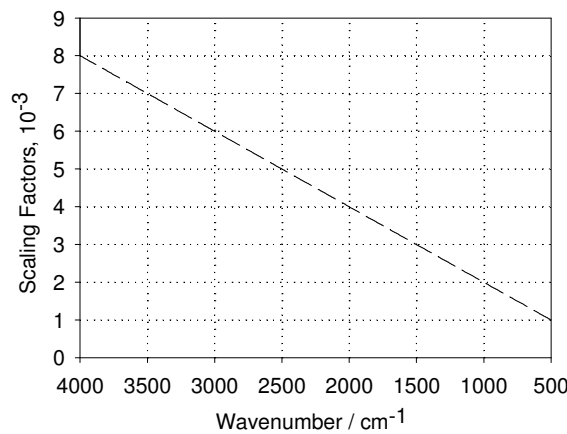


Figure 10. Dependence of the scaling factor  $\kappa_1$  on the wavenumber  $\tilde{\nu}$ . The solvent overcompensation in presence of a thin layer ( $d_0=1.3$  nm) corresponds to the product of  $\kappa_1$  and the absorbance spectrum of pure solvent in contact with the MIRE.

The second problem that appears in background compensation of time-resolved spectra of growing layer still in reactive solution is due not only to reactive solution displacement by the growing layer but also solvent dilution by solute molecules. For such background compensation measurement of an SBSR spectrum of reactive solution is necessary. In case of a very reactive compound it is principally not possible to measure such SBSR spectrum unless chemical reaction with the Ge MIRE surface starts immediately. This problem can be overcome by theoretical means, too.

The principle of this method is the following. The final layer spectrum in solvent should be subtracted from the spectrum of the final layer still in contact with reactive solution resulting in the absorbance spectrum of reactive solution in the range from distance  $d_0$  (layer thickness) to infinity. The experimentally not accessible spectrum of reactive solution can now be scaled down from  $d_0$  (layer thickness) to distance  $d=0$  (MIRE surface) using a new scaling factor  $\kappa_2$ .

According to eq. (30) effective thickness of not available reactive solution spectrum ranging from  $z_i=0$  to  $z_f=\infty$  can be expressed by

$$\begin{aligned} d_{e,pp/vp}^{b,iso}(0,\infty) &= \frac{1}{\cos\theta} \cdot \frac{n_3}{n_1} \cdot \frac{d_p}{2} \cdot E_{b,pp/vp}^2 \cdot \left( e^{-\frac{2 \cdot 0}{d_p}} - e^{-\frac{2 \cdot \infty}{d_p}} \right) = \\ &= \frac{1}{\cos\theta} \cdot \frac{n_3}{n_1} \cdot \frac{d_p}{2} \cdot E_{b,pp/vp}^2 \end{aligned} \quad (34)$$

The effective thickness of reactive solution above the growing layer ( $z_i=d_0$  to  $z_f=\infty$ ) can be written as:

$$\begin{aligned} d_{e,pp/vp}^{b,iso}(d_0,\infty) &= \frac{1}{\cos\theta} \cdot \frac{n_3}{n_1} \cdot \frac{d_p}{2} \cdot E_{b,pp/vp}^2 \cdot \left( e^{-\frac{2 \cdot d_0}{d_p}} - e^{-\frac{2 \cdot \infty}{d_p}} \right) = \\ &= \frac{1}{\cos\theta} \cdot \frac{n_3}{n_1} \cdot \frac{d_p}{2} \cdot E_{b,pp/vp}^2 \cdot e^{-\frac{2 \cdot d_0}{d_p}} \end{aligned} \quad (35)$$

The scaling factor  $\kappa_2$  presents the ratio between the effective thickness of reactive solution ranging from 0 to  $\infty$  and of reactive solution from  $d_0$  to  $\infty$  as given by eq. (36)

$$\begin{aligned}
\frac{d_{e,pp/vp}^{b,iso}(0,\infty)}{d_{e,pp/vp}^{b,iso}(d_0,\infty)} &= \frac{\frac{1}{\cos\theta} \cdot \frac{n_3}{n_1} \cdot \frac{d_p}{2} \cdot E_{b,pp/vp}^2}{\frac{1}{\cos\theta} \cdot \frac{n_3}{n_1} \cdot \frac{d_p}{2} \cdot E_{b,pp/vp}^2 \cdot e^{-\frac{2 \cdot d_0}{d_p}}} = e^{\frac{2 \cdot d_0}{d_p}} \\
d_{e,pp/vp}^{b,iso}(0,\infty) &= e^{\frac{2 \cdot d_0}{d_p}} \cdot d_{e,pp/vp}^{b,iso}(d_0,\infty) = \kappa_2 \cdot d_{e,pp/vp}^{b,iso}(d_0,\infty) \\
\kappa_2 &= e^{\frac{2 \cdot d_0}{d_p}} \tag{36}
\end{aligned}$$

Calculated spectrum of reactive solution (0 to  $\infty$ ) is used now as a new artificial reference spectrum for background subtraction of time-resolved spectra. For each time point, artificial reference spectrum is scaled down by scaling factor  $\kappa_1$  and added to the corresponding time-resolved spectrum removing background overcompensation.

## *Chapter 3 MATERIALS AND METHODS*

### **3.1 Experimental techniques**

#### **3.1.1 FTIR ATR equipment**

Multiple internal reflection elements (MIREs) of trapezoidal shape were made of germanium (Ge,  $52 \times 20 \times 2.1 \text{ mm}^3$ ,  $51 \times 20 \times 1.44 \text{ mm}^3$ ,  $51 \times 20 \times 1.48 \text{ mm}^3$ ) and cadmium-telluride (CdTe,  $52 \times 19.5 \times 1.6 \text{ mm}^3$ ). At the nominal angle of incidence  $\theta = 45^\circ$  according to eq. (29) one obtained 19.4, 27.97, 27.29 and 25.3 active internal reflections, respectively.

Stationary and modulated excitation (ME) ATR FTIR spectra were recorded with Bruker IFS 66 spectrometer at  $T = 15^\circ\text{C}$  (or  $25^\circ\text{C}$ ) and  $22^\circ\text{C}$ , respectively. Instrument was equipped with a lift-model Single-Beam-Sample-Reference (SBSR) ATR mirror attachment with a hydrodynamically optimized and water-thermostated cell (flow-through cuvette) made of poly(ether ether ketone) (Peek). Spectra were recorded with parallel and perpendicular polarized IR light produced by an aluminium grid polarizer on a KRS-5 substrate. A mercury cadmium telluride (MCT) detector was used. Spectral resolution was  $4 \text{ cm}^{-1}$  with zero filling factor 4. The Blackman-Harris 3-Term function was used for apodization.

#### **3.1.2 SBSR spectroscopy**

Most FTIR spectrometers are working in the single-beam (SB) mode. As a consequence, a single-channel reference spectrum has to be stored for later conversion of single-channel sample spectra into transmittance and absorbance spectra. This technique suffers inaccuracy owing to drifts resulting from the instrument, the sample or atmospheric absorption. In order to eliminate these unwanted effects to a great extent a new ATR attachment has been constructed, converting a single-beam instrument into a pseudo-double-beam instrument. The principle features of this attachment are depicted in Figure 11.

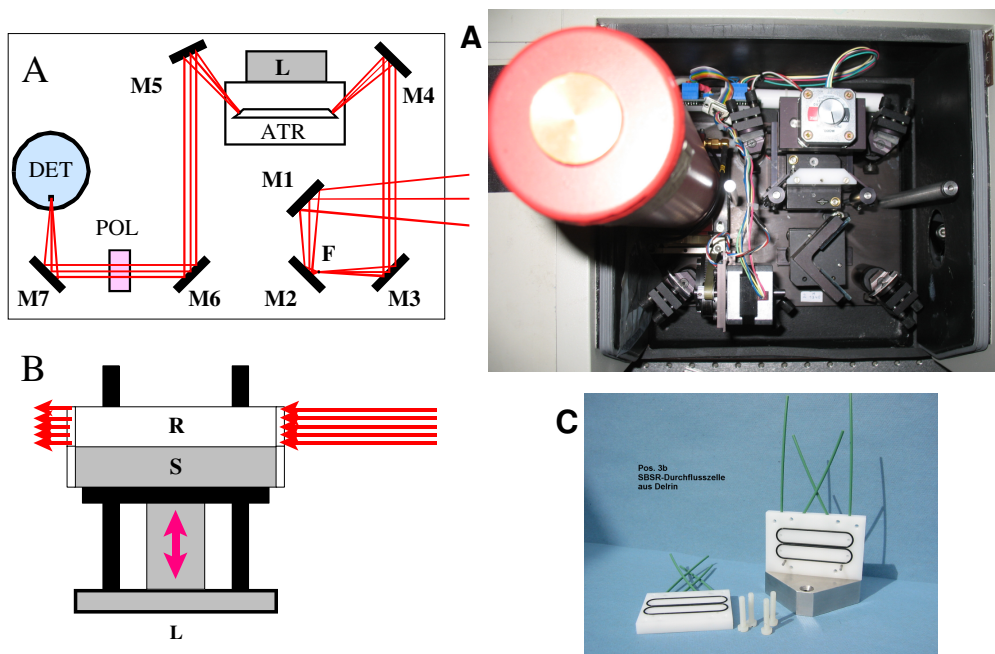


Figure 11. Single Beam Sample Reference (SBSR) ATR attachment. (A) The focus in the sample compartment is displaced to the position F by the planar mirrors M1 and M2. The off-axis parabolic mirror M3 produces a parallel beam with a diameter of one centimeter, i.e. half of the height of the IRE. The cylindrical mirror M4 focuses the light to the entrance face of the IRE. M5 which has the same shape as M4 reconverts to parallel light passing via the planar mirror M6 through the polarizer POL and being focused to the detector DET by the off-axis parabolic mirror M7. (B) Alternative change from sample to reference and vice versa is performed by computer controlled lifting and lowering of the ATR cell body. (C) Flow-through SBSR cell.

As usually, a convergent IR beam enters the sample compartment. The focal point is now displaced by the planar mirrors M1 and M2 to the new position F, whereas the off-axis parabolic mirror M3 performs a conversion of the divergent beam into a parallel beam with fourfold reduced cross-section. This beam is focused to the entrance face of a trapezoidal IRE by a cylindrical mirror M4. Therefore, the ray propagation in the IRE is still parallel to the direction of light propagation (x-axis), enabling subdivision of the large IRE surfaces (x,y-plane) in perpendicular direction (y-axis) to the light propagation. One half of the IRE is then used for the sample (S) and the other one for the reference (R). Both S and R were encapsulated by flow-through cuvettes, independently accessible by liquid or gaseous flow-through. This principle is referred to as *Single Beam Sample Reference (SBSR)* technique.

The SBSR cell (Figure 11, C) made of Peek is placed on the cell platform (Figure 11, B). It consists of independently accessible S and R cuvettes on both sides of the MIRE. Viton O-rings were used for sealing. The cuvettes have been

hydrodynamically optimized with respect to flow-through featuring a rectangular shape ( $35.35 \times 7.5 \text{ mm}^2$ ), terminated on either side by a half circle ( $r = 3.75 \text{ mm}$ ). The distance between the MIRE and cell body was  $\sim 150 \mu\text{m}$  resulting in a volume of  $\sim 50 \mu\text{L}$  per cuvette. Temperature regulation of the SBSR cell within  $\pm 0.2^\circ\text{C}$  was achieved by an external thermostat with circulating water. The temperature of the cell was monitored throughout the experiment by means of a digital contact thermometer. All SBSR equipment was obtained from OPTISPEC [93]. The cell platform is moved alternatively up and down aligning the sample and reference cuvettes with the IR beam, respectively. [88, 94]

SBSR absorbance spectra are calculated from sample and reference single channel spectra which have been measured with very short mutual time delay.

### **3.1.3 Modulation Spectroscopy**

Modulation spectroscopy or modulated excitation (ME) spectroscopy can always be applied if a system admits a periodic alteration of its state by the variation of an external parameter, such as temperature (T), pressure (p), concentration (c), electric field (E), electric potential ( $\Psi$ ), radiant power ( $\Phi$ ) or mechanical force (F) [95]. The response of the system to a ME will also be periodic, exhibiting the same frequency as the stimulation (Figure 12). In case of a non-linear system the response to a sinusoidal stimulation will also contain multiples of the fundamental frequency. After an initial period of stimulation, the system will reach the stationary state, which is characterized by periodic alterations around a constant mean. In case of incomplete reversibility, e.g. the existence of an irreversible exit in the reaction scheme, the signal amplitudes of the initial components and of the intermediate species will decline, as the system is approaching its final state.

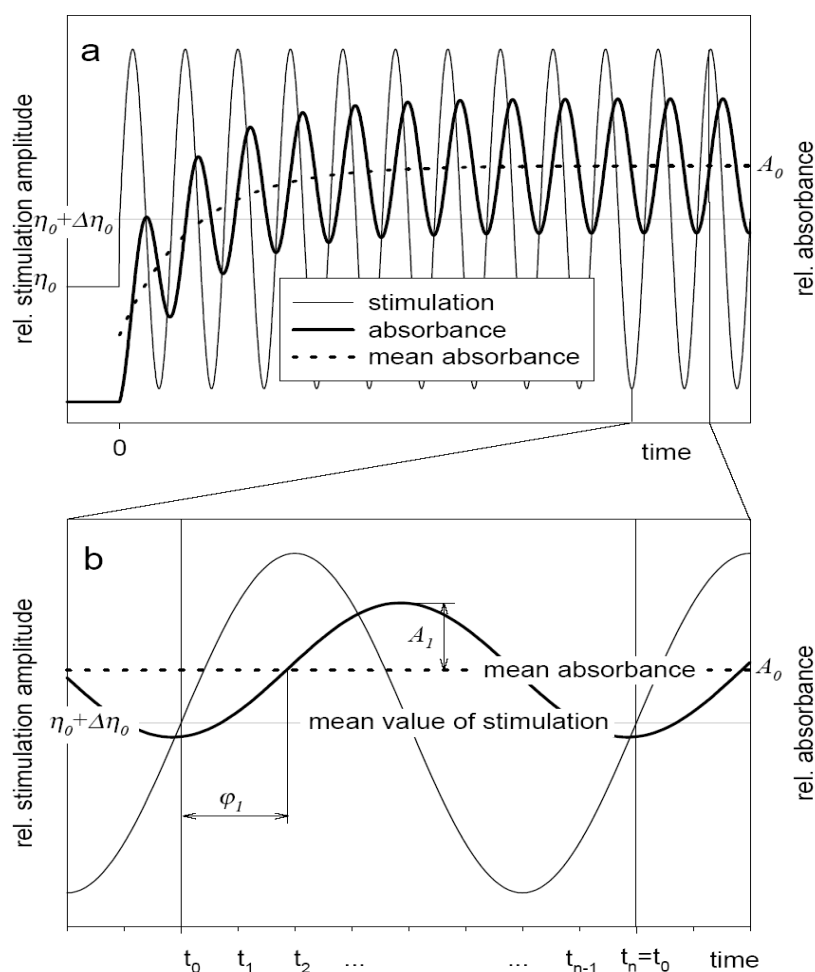


Figure 12. Periodic stimulation and induced changes in the concentration of an absorbing species. (a) The sinusoidal excitation (e.g. concentration) starts at the time  $t=0$  with an additional jump from the initial stimulation value  $\eta_0$  to the mean stimulation value  $\eta_0 + \Delta\eta_0$ . After an initial time (in this case approximately five periods) the stationary state is reached. In this state the absorbance varies periodically around a mean value  $A_0$ . It should be noted that data sampling in modulation spectroscopy always has to be delayed by the time the system is required to reach this stationary state. At low modulation frequencies this can lead to a considerable extension of the measurement time. (b) Expanded section of (a). In the stationary state the absorbance of the excited species and the stimulation show a phase lag  $\Phi_i$ , which is characteristic of the kinetics of the stimulated system.  $A_1$  is the absorbance modulation amplitude. Calculation was based on first order kinetics, i.e. with a linear system. Consequently, a sinusoidal stimulation cannot produce higher harmonics in the response. In a typical modulation experiment, data acquisition is performed in the stationary state of excitation. The measurement of the  $n$  time-resolved spectra takes place at the times  $t_i (i=0 \dots n-1)$  and is triggered by the beginning of each stimulation period. The sample points of the  $n$  spectra have to fit exactly into the time of one period. (figure taken from [96]).

Phase sensitive detection (PSD) is used for the evaluation of amplitudes and phase lags of the periodic system response. In a simple view, PSD applied to data from a spectroscopic ME experiment results in a special kind of difference spectra between excited and non-excited states, so called *phase resolved spectra* (for a detailed description refer to [95] and [96]). Let us consider a system, which is stimulated by a sinusoidally oscillating external parameter. During one half-wave one has excitation followed by relaxation in the other. In the stationary state, this alteration between excitation and relaxation may be repeated as many times as necessary in order to obtain a good signal-to-noise (S/N) ratio of the modulation spectra. Moreover, it should be noted that PSD is a narrow band detection, i.e. noise contributes only from a frequency range which is close to the stimulation frequency  $\omega_m$ .

Since the periodic system response is evaluated automatically within each period of stimulation, instabilities of the spectrometer, the environment and the sample are much better compensated than with conventional techniques, where a reference spectrum has to be stored at the beginning of the experiment. As a consequence, ME technique generally leads to high quality background compensation with a low noise level resulting in enhanced sensitivity by at least one order of magnitude.

So far, ME spectroscopy appears as a special type of difference spectroscopy. Details about difference spectroscopy are given in ref. [97]. This is true if the frequency of stimulation is slow compared to the kinetics of the response of the stimulated system. However, if one or more relaxation times of the externally excited process fulfil the condition  $0.1 < \omega_m \cdot \tau_i < 10$ , where  $\omega_m$  denotes the angular frequency of stimulation and  $\tau_i$  is the  $i$ -th relaxation time of the system, significant phase lags  $\Phi_i$  between stimulation and sample responses will occur. Phase lag and relaxation time are related by  $\Phi_i = \arctan(-\omega_m \cdot \tau_i)$ . This phenomenon is paralleled by damping of the response amplitudes  $A_i$ . Both are significant of the underlying reaction scheme and the associated rate constants of the stimulated process [98]. In this case selectivity of ME spectroscopy, e.g. with respect to single components in heavily overlapping absorption bands is significantly higher than that achievable by normal difference spectroscopy. The reason is the typical dependence of phase lags  $\Phi_i$  and amplitudes  $A_i$  on the modulation frequency  $\omega_m$ . If a set of absorption bands of a modulation spectrum exhibits the same phase lag  $\Phi_i$  it is considered as a correlated population. Such a population consists e.g. of molecules or parts of them that are involved in the same reaction step. The assignment of a group of absorption bands in a modulation



spectrum to a population is considered to be validated if upon changing the stimulation frequency  $\omega_m$  all these bands exhibit further on the same dependence with respect to phase lag  $\Phi_i(\omega_m)$  and amplitude  $A_i(\omega_m)$ .

Moreover, the dependence of phase lag and amplitude on  $\omega_m$  may be calculated based on a given reaction scheme. Obviously, ME spectroscopy enables a very rigorous test of the significance of a reaction scheme since consistence of experimental data with theory derived from a given reaction scheme must hold on over the whole frequency range of stimulation. Theoretically modulation spectroscopy and relaxation spectroscopy [98,99,100] have the same information content regarding kinetic parameters. It should be noted, that the stimulation frequency  $\omega_m$  means an additional degree of experimental freedom for modulation spectroscopy. Consequently, the experimentally available kinetic data may be spread on a 2D scale, the  $\omega_m$ -t-plane, while relaxation experiments result in the same information on linear scale, the t-axis. Therefore, the former enables a more rigorous validation of experimental data since the system response at any frequency must be consistent with the reaction scheme underlying the kinetic analysis. The price to pay for this advantage is, however, a more complicated theoretical approach for the evaluation of kinetic parameters.

At the beginning of a ME experiment the system will relax from its equilibrium state to a new quasi steady-state. This will last about three times the largest relaxation time of the system. Now data acquisition may begin by measuring  $N$  spectra at equidistant time slices within each repetitive stimulation period  $T$ , thus approximating the continuous sample response  $A(\tilde{\nu}, t)$ . These  $N$  so called *sample point spectra* are then co-added and subjected to a *digital phase sensitive detection (PSD)* resulting in the so called *phase-resolved or demodulated spectra* according to eq. (37).

$$A_k^{\phi_k^{\text{PSD}}}(\tilde{\nu}) = \frac{2}{T} \int_0^T A(\tilde{\nu}, t) \sin(k \cdot \omega \cdot t + \phi_k^{\text{PSD}}) dt \quad (37)$$

$A(\tilde{\nu}, t)$  represents the time-resolved steady state spectral response of a sample that is periodically stimulated at frequency  $\omega$ . In a general case,  $A(\tilde{\nu}, t)$  may be a superposition of partial responses in the fundamental  $\omega$  as well as in higher harmonics  $k \cdot \omega$  according to eq. (38)

$$A(\tilde{\nu}, t) = \sum_k A_{k0}(\tilde{\nu}) \cdot \sin(k \cdot \omega \cdot t + \phi_k) \quad (38)$$

Introducing eq. (38) into eq. (37) results in

$$A_k^{\phi_k^{\text{PSD}}}(\tilde{\nu}) = A_{k0}(\tilde{\nu}) \cdot \cos(\phi_k - \phi_k^{\text{PSD}}) \quad (39)$$

Eqs. (37) and (39) explain the principal features of PSD. The periodic stationary sample response  $A(\tilde{\nu}, t)$  has to be multiplied by a demodulation function. In case of eq. (37) demodulation occurs at frequency  $k \cdot \omega$ . Moreover a new arbitrary parameter  $\phi_k^{\text{PSD}}$  is introduced. As a consequence, this procedure extracts the amplitude of the sample response with frequency  $k \cdot \omega$  from the overall signal resulting in phase resolved spectra described by eq. (39).  $\phi_k$  denotes the phase delay in the  $k \cdot \omega$  response between the onset of stimulation with frequency  $\omega$  and the response of the sample. In case of harmonic stimulation with frequency  $\omega$ , a signal response at  $k \neq 1$  unambiguously points to non-linear steps in the reaction scheme of the system. MES has also access to time resolved information, since phase delays  $\phi_k$  introduced by the system are related to the reaction scheme as well as to the underlying rate constants. If the period of stimulation is long compared to relaxation times of the system, e.g. as in case of a chemical stimulation, time resolved information is no longer available, however, there remain still two most relevant advantages of MES over conventional difference spectroscopy. (i) The signal-to-noise ratio of a phase resolved spectrum is at least 10 times better than achievable by conventional difference spectroscopy, since in an electronic sense, MES is a narrow band technique. (ii) MES with PSD results in a Fourier analysis of the sample response which is significant of the underlying reaction scheme. Conventional difference spectroscopy has no access to this information.

In this experiment the stimulation period was  $T=5\text{min}$ , i.e. the layer was 2.5min in contact with both stimulating solutions of pH 4 and pH 8, respectively. Six modulation cycles have been added leading to an overall accumulation time of 30min per presented parallel ME spectrum.

For more details reader is referred to ref. [95] and [96].

### 3.1.4 Atomic Force Microscopy (AFM) and Environmental Scanning Electron Microscopy (ESEM)

*Atomic force microscopy.* Characterization of surface topography and manipulation of silane films were carried out with a XE-100 scanning probe microscope (Park Systems Inc.) equipped with a closed-loop xy-scanner (scan range 50  $\mu\text{m}$  x 50  $\mu\text{m}$ ) and a closed-loop z-scanner. The instrument was located on a home-made air-damped platform standing on an active vibration isolation unit (MOD-1 L plus, Halcyonics GmbH). For characterization and manipulation silicon non-contact cantilevers (tip radius  $\leq 10$  nm, nominal resonant frequency 320 kHz, nominal force constant 42 N / m) were used. In all experiments the scan rate was set to 1 Hz and (256 x 256) data points were generated. The topography characterization was done using true non-contact mode atomic force microscopy (AFM). After film characterization the surface was manipulated (scratched) using contact mode AFM (with a non-contact cantilever). Subsequently the manipulated probe was characterized again with true non-contact AFM. The used scan size was bigger than in manipulation experiments to characterize the manipulated and the non-manipulated surface in the same image.

*Environmental Scanning Electron Microscopy.* Characterization of the silane layer was carried out by an environmental scanning electron microscope using a Philips ESEM XL 30 FEG. This kind of SEM uses a chamber atmosphere of 1-3 Torr water vapour instead of high vacuum. Because the instrument is equipped with a special gaseous secondary electron detector (GSE detector), sputtering of the samples with conductive material like gold or carbon is not necessary. The incident electron beam produces also X-rays, thus energy dispersive X-ray spectroscopy (EDX) has been performed by using environmental scanning electron microscope at pressure of 1 Torr.

### 3.2 Chemicals

Chemicals used for silanization:

- 7-Octenyltrichlorosilane,  $C_8H_{15}SiCl_3$ , (95% contains 10-15% isomers) 7-OTCS, purchased from ABCR GmbH&Co. and used as received
- Toluene,  $C_6H_5CH_3$ , (99.9%), purchased from Sigma Aldrich
- Molecular sieve Dehydrate Fluka with indicator for drying solvents (beads).

Chemicals used for carboxyl group activation purchased from Sigma Aldrich:

- *N*-hydroxysuccinimide (NHS),  $C_4H_5NO_3$  (purity  $\geq 97.0\%$ )
- *N*-Cyclohexyl-*N*-(2-morpholinoethyl)-carbodiimide metho-*p*-toluenesulfonate,  $C_{14}H_{26}N_3O \cdot C_7H_7O_3S$ , CMC (purity  $\geq 99.0\%$ ).

Chemicals used for the determination of integrated molar absorption coefficients:

- Sodium-acetate,  $C_2H_3NaO_2$ , purchased from Sigma Aldrich
- *N*-acetyl-D-glucosamine (2-Acetamido-2-deoxy-D-glucose),  $C_8H_{15}NO_6$ , BioChemika,  $\geq 99.0\%$  (sum of enantiomers, HPLC) was purchased from Sigma Aldrich.

Chemicals used for amide bond formation:

- D-(+)-Glucosamine hydrochloride,  $C_6H_{13}NO_5 \cdot HCl$  (minimum 99%), purchased from Sigma Aldrich
- Amino-dextran molecular weight MW=40000, ~0.1 mmol primary amine per gram of dextran was purchased from CarboMer, Inc.
- Ethanolamine,  $C_2H_7NO$  (p.a. ACS:  $\geq 99.0\%$ ), purchased from Fluka
- Bovine Serum Albumin (BSA) (minimum 98%, electrophoresis), purchased from Sigma Aldrich
- Sodium dodecyl sulfate,  $C_{12}H_{25}NaO_4S$  (Assay  $\geq 99\%$ ), purchased from Fluka.

### 3.3 Methods

#### 3.3.1 Polishing and surface activation of Ge ATR MIRE

The aim of the Ge MIRE activation was to produce free hydroxyl groups at the surfaces which was a prerequisite for the reaction with chlorosilanes. The first step was polishing of both sides of the MIRE by machine (Logitech PM5, 60 rpm for 2 min) using a pella cloth immersed with 0.1  $\mu\text{m}$  diamond particle suspension (AB Technics, Tribuswinkel, Austria) followed by cleaning with ethanol. Remaining organic impurities could be then removed by plasma cleaning (Harrick Scientific Products, Inc., Pleasantville, NY 10570, U.S.A.) for 3 min in laboratory atmosphere. The resulting oxidized surface layer was activated by immersing the plates in ultra pure water for 30 min and drying it by a pure air flow. The MIRE was considered to be clean if the  $\nu(\text{CH}_2)$  bands at  $\sim 2920\text{ cm}^{-1}$  and  $\sim 2850\text{ cm}^{-1}$  disappeared completely in the FTIR ATR spectrum (single beam mode). The MIRE was mounted in the SBSR flow-through cell immediately after this procedure.

#### 3.3.2 Silanization of the Ge and CdTe MIREs

Silanization with 7-OTCS molecules critically depends on the solvent humidity. Since 7-OTCS molecules are very reactive and hydrolyze and polymerize even in a presence of small water traces, water free toluene was required. Moreover, a silanization apparatus (OPTISPEC, Switzerland) was built to enable handling in a completely dry atmosphere (Figure 13).

As first, toluene dehydrated by molecular sieve beads was directed throughout degassing unit and silanization apparatus tubes into separated reference (R) and sample (S) reservoirs. Before reaching the R channel of the SBSR cell, toluene from the R reservoir was degassed once more to avoid bubble formation. Silane solution was prepared by mixing toluene from S reservoir and 7-OTCS from a separate reservoir. Tubes leading to the SBSR cell were preconditioned by a short flow of 7-OTCS solution directed to waste.

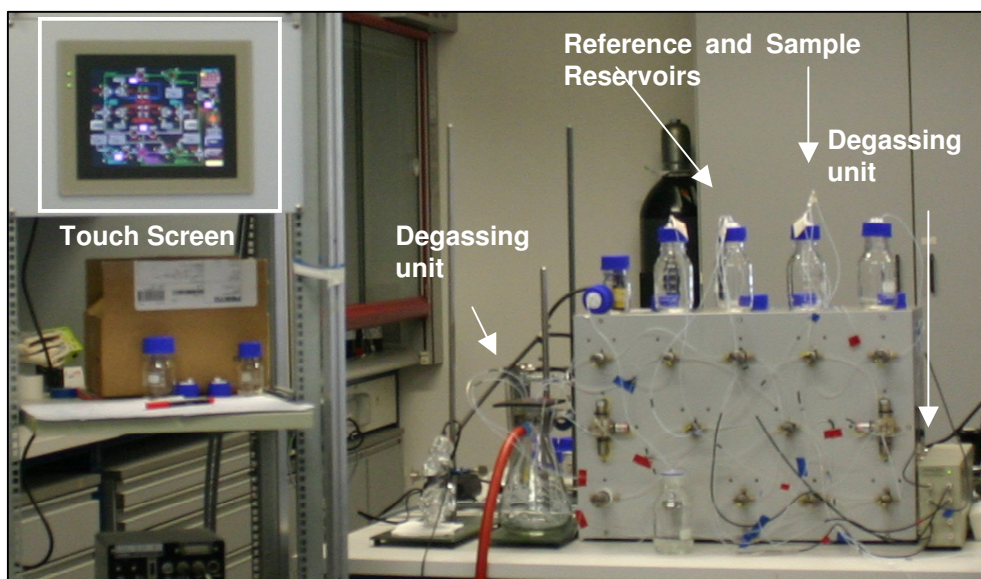


Figure 13. Silanization apparatus.

Measurement was performed in the following steps. First, both cuvettes R and S of Ge MIRE were empty for the measurement of the SBSR reference spectrum of dry hydroxylated plate. Then, both cuvettes were filled with toluene. The SBSR reference spectrum of toluene was recorded during toluene flow. Before starting the reaction in the S cuvettes, the R cuvettes were clamped and remained filled with toluene during the whole experiment. Silanization in the S cuvettes was initiated by a fast exchange of toluene, pumping a 1% solution of 7-OTCS at a flow rate of  $16.5 \mu\text{l/sec}$  leading to a complete exchange of the solution in S cuvettes within 4 sec. After few seconds, pumping rate was reduced to  $0.83 \mu\text{l/sec}$  and kept constant during the whole experiment acquiring time resolved single beam spectra over a period of  $\sim 90$  min.

### 3.3.3 Oxidation of terminal double bond of the silane layer by ozone

Oxidation of a dry layer by gaseous ozone at  $T=15^\circ\text{C}$  was monitored *in situ* using ATR FTIR spectroscopy. Double bond oxidation was performed by exposing the dry silane layer to Ar diluted ozone ( $\text{O}_3$ ). Mechanism of ozonization is given in Appendix 6.1.

The SBSR cell was connected via viton tubes to a homemade UV chamber containing a small Pen-Ray UV lamp emitting the mercury spectrum with the primary wavelength at 254 nm inside (Figure 14). Approximately 3 % of the intensity was due to emission at 184 nm which is responsible for the ozone generation. [101]



Figure 14. A homemade UV chamber containing a small Pen-Ray UV lamp emitting the mercury spectrum with the primary wavenlength at 254 nm inside.

The reference SBSR spectrum of dried layer was recorded in the stationary state just before oxidation. Time-resolved SBSR spectra were acquired over a time period of 30 min. The acquisition time for one spectrum was typically 220 sec corresponding to 200 scans at a resolution of  $4\text{ cm}^{-1}$ . After complete oxidation of the double bond the SBSR spectra of the dry oxidized layer were recorded with parallel and perpendicular polarized light.

### 3.3.4 Identification of the expected COOH group

Two independent experiments, stationary and ME, were performed in order to prove the existence of COOH groups produced by oxidation of a terminal ethylenic double bond of the silane layer. For that purpose the oxidized layer was investigated in aqueous environment at pH 4 and pH 8 at  $T=22^\circ\text{C}$ . If the end-standing group would be really -COOH one would expect deprotonation at pH 8 leading to two characteristic bands near  $1550$  and  $1400\text{ cm}^{-1}$  which result from asymmetric and symmetric stretching of  $\text{COO}^-$  group.

Stationary and ME experiments were performed on Bruker IFS 66 spectrometer. The SBSR cell was connected to two computer-controlled peristaltic pumps working alternatively at a flow rates of  $1\text{ ml/min}$ . Both, the R and S cuvettes were first exposed to a buffer solutions of pH 4 followed by exchange to pH 8, in order to induce periodic protonation and deprotonation of the carboxylic acid groups.

ME FTIR spectra were treated as if they were points of a periodic response of a stimulated system (for details see Section 3.1.3). To do that,  $N=32$  equidistant time-resolved single channel spectra, referred to as sample-point spectra, were recorded within each period of stimulation. Thus 16 sample-point spectra were associated with the half-period corresponding to pH 4 while the second 16 sample-point spectra were recorded in the half-period where solution at pH 8 was pumped throughout the cell. These spectra were co-added over 6 periods. The duration of one cycle ( $T$ ) was 5 min. Time Resolved Spectra were acquired by the “Rapid Scan Time Resolved Measure”-mode.

### 3.3.5 Activation of the carboxyl groups

The principle of the carboxyl group activation by *N*-hydroxysuccinimide (NHS) and *N*-Cyclohexyl-*N'*-(2-morpholinoethyl) carbodiimide metho-*p*-toluenesulfonate (CMC) is described in Figure 15 [102]. The combination of two chemicals, CMC and HNS, is often used to increase coupling efficiency or to create a stable amino-reactive product.

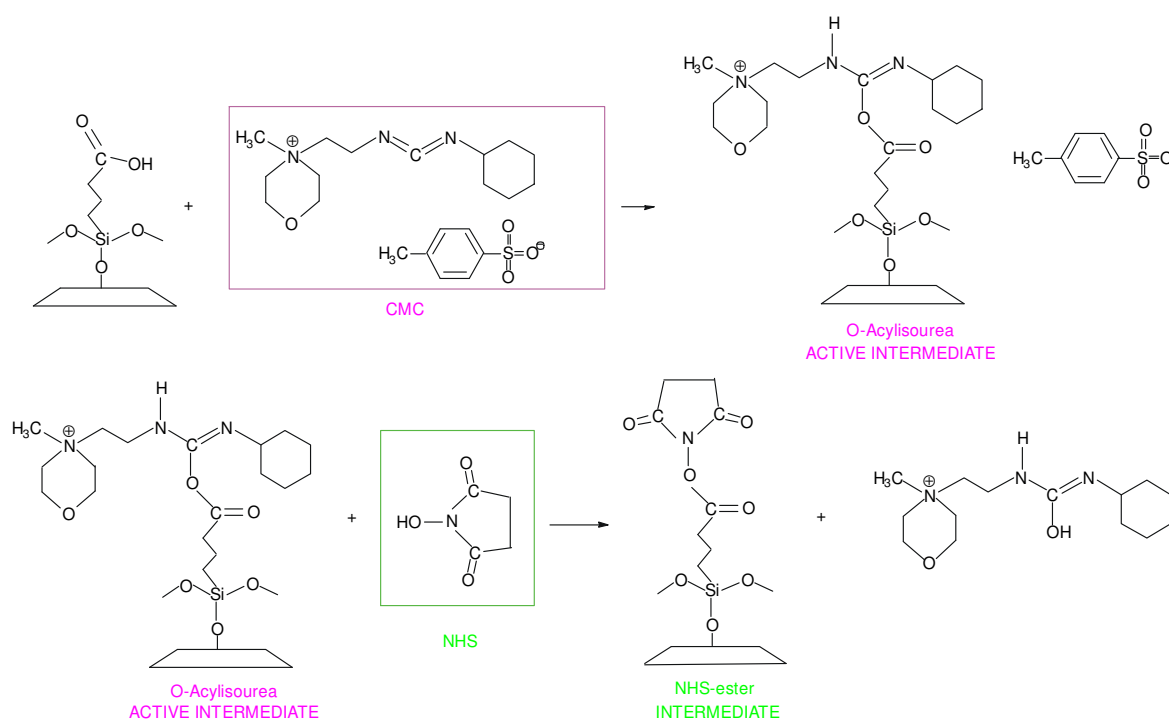


Figure 15. Principle of the COOH activation by a mixture of *N*-Cyclohexyl-*N'*-(2-morpholinoethyl) carbodiimide metho-*p*-toluenesulfonate (CMC) and *N*-hydroxysuccinimide (NHS).

The carbodiimide is the promoter, which converts the acid into the *O*-acylisourea intermediate while NHS is a catalyst that readily reacts with *O*-acylisourea



intermediate affording the *N*-hydroxysuccinimidyl ester (NHS-ester). [103] The NHS-ester is a well known species, which has been detected on silicon surface with ATR-FTIR. [104]

The carboxyl groups on the oxidized silane surface are transformed into reactive *N*-hydroxysuccinimide esters (NHS-esters) by injection of a mixture of 0.1 M NHS and 0.4 M CMC in water at pH=6.2 and T=25 °C for 20 min. The system was then washed with ultra-pure water and the SBSR spectrum of the NHS-ester terminated silane layer was recorded.

### 3.3.6 Amide bond formation between amino species and NHS-ester terminated silane layer

The reaction of amide bond formation between NHS-ester terminated silane layer and amino species is shown in Figure 16. Mechanism is given in Appendix 6.2.

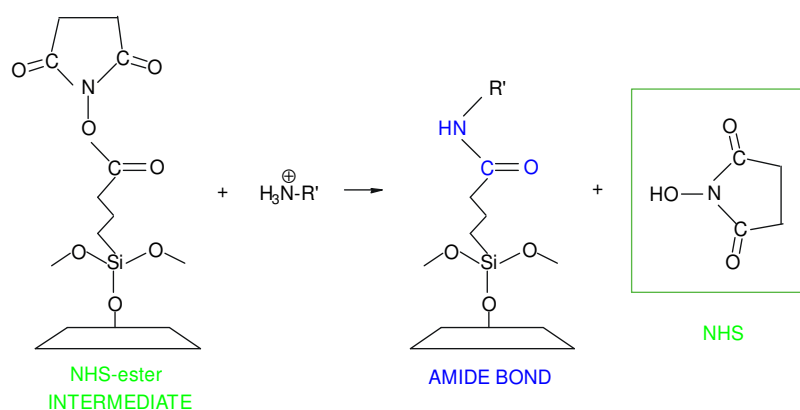


Figure 16. The coupling reaction between NHS-ester terminated silane layer and amino species.

Glucosamine hydrochloride (5 mM) was dissolved in a phosphate-buffered saline solution (PBS, containing 10 mM phosphate, 138 mM NaCl and 2.7 mM KCl in deionized water) at pH=7.20 reached by using  $\text{Na}_2\text{HPO}_4$  and passed over the NHS-esters activated silane surface in the S cuvettes over 75 min at pump velocity 0.2 ml/min and at T=25 °C. The R cuvettes were exposed only to the PBS solution at pH=7.2.

Amino-dextran in amount of 1 g was dissolved in 16 ml of ultra-pure  $\text{H}_2\text{O}$  in a presence of HCl and pH was adjusted by NaOH to 7.2. Prepared dextran solution was recirculating over the NHS-ester activated silane surface at pump velocity of 0.5 ml/min over 1 hour.

The SBSR spectra of the silane layer were measured before and after glucosamine and amino-dextran flow into the S cuvettes in both H<sub>2</sub>O and D<sub>2</sub>O environment in order to see the effect on the NHS-ester activated silane layer. The remaining reactive esters are transformed into amides by injection of 1 M ethanolamine hydrochloride at pH=8.5. [102]

### **3.3.7 Bovine Serum Albumin (BSA) adsorption**

Saccharide modified silane surfaces were exposed to 10 mM protein (Bovine Serum Albumin, BSA) solution at T=25°C in order to investigate the resistance of such surfaces against protein adsorption. Adsorption of BSA on clean Ge surface was used as a reference. Irreversibly adsorbed protein was cleaned by washing with SDS (10 mg/ml in PBS).

## Chapter 4 RESULTS AND DISCUSSION

### 4.1 SILANIZATION

#### 4.1.1 Surface activation of Ge MIRE

The existence of hydroxylated Ge surface was a prerequisite for the silanisation reaction with chlorosilanes. It was achieved by rinsing the oxidized Ge MIRE in deionized water (see Section 3.3.1).

Figure 17 shows the effect of Ge surface activation. The SBSR FTIR spectrum measured after the Ge MIRE was removed from the plasma cleaner and immediately placed in the sample compartment of the instrument is shown in Figure 17A. The SBSR FTIR spectrum measured after exposing the sample compartment of the Ge MIRE to deionized water and drying is presented in Figure 17B. The change of this spectrum results predominately from the sample, since the reference was exposed only to laboratory atmosphere.

The influence of the laboratory humidity on the oxidized Ge in the reference compartment is shown in Figure 17C where as reference the spectrum of oxidized Ge MIRE just after plasma treatment is taken. Correlated vibrations placed at  $\sim 3230$ ,  $1442$  and  $790\text{ cm}^{-1}$  are probably related to water layer hydrogen bonded to the oxidized Ge surface and may be assigned to OH vibration hydrogen bonded to Ge-O surface, the bending  $\delta(\text{OH})$  vibration and stretching  $\nu(\text{Ge-O-Ge})$  vibration where water molecules are hydrogen bonded to the oxygen atom, respectively. Bending  $\delta(\text{OH})$  vibration is placed at  $\sim 1650\text{ cm}^{-1}$ . Modification of the oxidized Ge surface is confirmed by negative vibrations at  $\sim 958$  and  $850\text{ cm}^{-1}$  assigned to  $\nu(\text{Ge-O})$  and  $\nu_{\text{as}}(\text{Ge-O-Ge})$ . [105] We could conclude that hydrogen bonded water layer was bound to the oxidized Ge surface only by exposing the oxidized Ge surface to ambient atmosphere.

Much stronger effect of deionized water on the oxidized Ge MIRE in the sample compartment is shown in Figure 17D (reference: oxidized Ge MIRE just after plasma treatment) documented by disappearing of  $\nu(\text{Ge-O})$  and  $\nu(\text{Ge-O-Ge})$  vibrations at  $958$  and  $850\text{ cm}^{-1}$  that probably correlate to band at  $1728\text{ cm}^{-1}$ . We suppose that the

water region between  $3700\text{--}2900\text{ cm}^{-1}$  consists of  $\nu(\text{OH})$  vibrations of Ge-hydroxide. Observed new positive band at  $3330\text{ cm}^{-1}$  probably resulted from  $\nu(\text{OH})$  stretching vibration of Ge-hydroxide formed during activation process. [106]

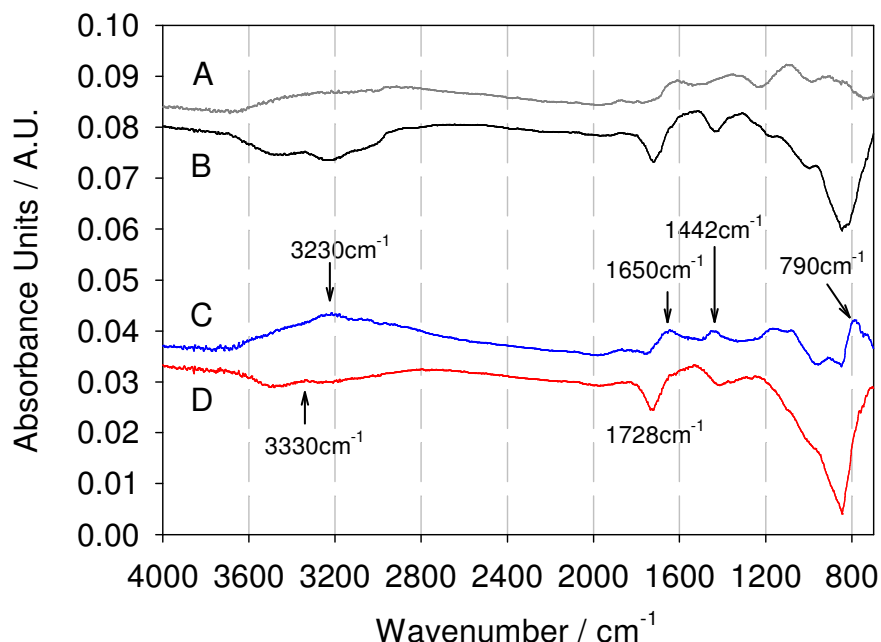


Figure 17. Effect of ultra-pure deionized water on a germanium MIRE. A. The SBSR FTIR spectrum of oxidized Ge MIRE by plasma cleaner. Baseline disturbance results from inhomogeneity of germanium surface; B. The SBSR FTIR spectrum measured after water activation only of the sample compartment of the Ge MIRE while reference was exposed to laboratory atmosphere; C. The absorbance FTIR spectrum reflecting the change of the Ge surface in the reference compartment due to exposition to laboratory air (reference and sample: Ge MIRE just after plasma treatment and after exposition to laboratory air, respectively); D. The absorbance FTIR spectrum showing the effect of water activation of the Ge surface in the sample compartment (reference and sample: oxidized Ge MIRE just after plasma treatment and after water activation, respectively). All spectra were measured in open delrin cell with parallel polarized light;  $T=15^{\circ}\text{C}$ ; Angle of incidence  $\theta=45^{\circ}$ ; Number of active internal reflections  $N=19.4$ .

#### 4.1.2 Silane layer preparation on Ge MIRE

Silanization reaction was stopped by exchange of 7-OTCS solution by pure toluene. Figure 18 shows the SBSR FTIR spectra of the final state of a typical silanization experiment. The silane layer was bound to the Ge MIRE only in the S channels, A. without and B. with toluene compensation according to eq. (33), while the R channels were filled with toluene. Details of toluene subtraction procedure are given in the next Section 4.1.3.

The broad negative band near  $3300\text{ cm}^{-1}$  and the negative band at  $1640\text{ cm}^{-1}$  are expected to result from an excess of hydrogen bonded water monolayer [107] produced by water activation of the Ge MIRE. This water layer was removed by the reaction with 7-OTCS, however, remained unaffected by dry toluene in the R channel. Some typical assignments should be mentioned:  $\nu_{\text{as}}(\text{CH}_2)$  and  $\nu_{\text{s}}(\text{CH}_2)$  at  $2927$  and  $2855\text{ cm}^{-1}$ ,  $\nu_{\text{as}}(\text{CH}=\text{CH}_2)$  at  $3077\text{ cm}^{-1}$ ,  $\nu(\text{C}=\text{C})$  at  $1641\text{ cm}^{-1}$  and  $\gamma_{\text{op}}(\text{CH}=\text{CH}_2)$  at  $911\text{ cm}^{-1}$ . The bands featuring chemical connection of 7-OTCS molecules to the Ge surface or 7-OTCS polymerization exhibit a broad low structured band between  $1250\text{--}975\text{ cm}^{-1}$  reflecting vibrations such as  $\nu(\text{Ge-O-Si})$ ,  $\nu(\text{Si-O-Si})$  and  $\nu(\text{Si-OH})$  [108].

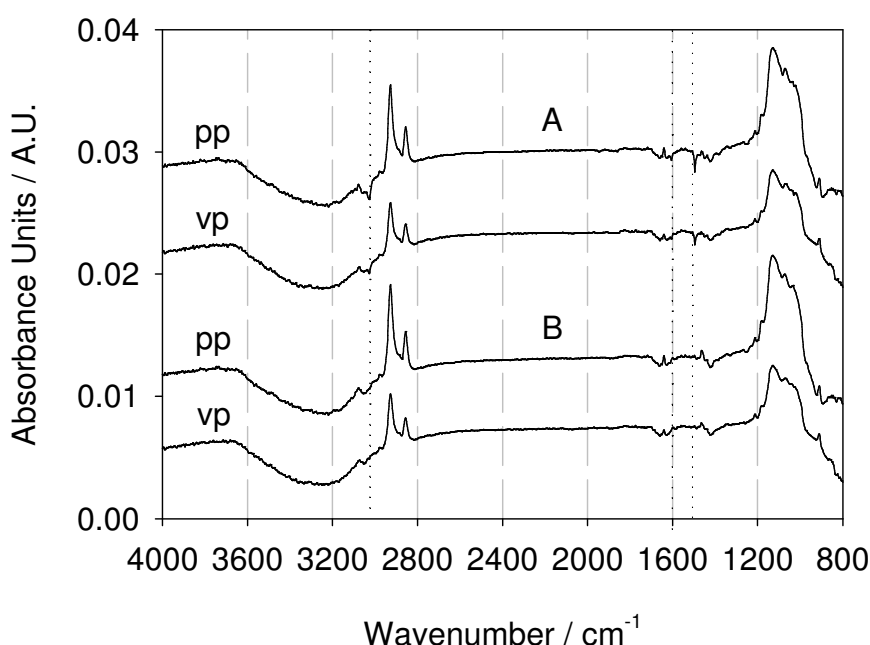


Figure 18. The SBSR FTIR spectra of a silane layer bound to the Ge MIRE only in the S cuvettes while the R cuvettes were filled with toluene, A. without and B. with toluene compensation. The broad negative band near  $3300\text{ cm}^{-1}$  and the negative band at  $1640\text{ cm}^{-1}$  are expected to result from a thin water layer removed in the S cuvettes due to chemical reaction with 7-OTCS; however, in the R cuvettes the water layer was too tightly attached at the Ge surface and could not be removed by dry toluene. Typical absorption bands of 7-OTCS may be assigned:  $\nu_{\text{as}}(\text{CH}_2)$  and  $\nu_{\text{s}}(\text{CH}_2)$  at  $2927\text{ cm}^{-1}$  and  $2855\text{ cm}^{-1}$ ,  $\delta(\text{CH}_2)$  at  $1463\text{ cm}^{-1}$ ,  $\nu_{\text{as}}(\text{CH}=\text{CH}_2)$  at  $3077\text{ cm}^{-1}$ ,  $\nu(\text{C}=\text{C})$  at  $1641\text{ cm}^{-1}$  and  $\gamma_{\text{op}}(\text{CH}=\text{CH}_2)$  at  $911\text{ cm}^{-1}$ . Finally the bands featuring connection of 7-OTCS to the Ge surface or 7-OTCS polymerization form a broad low structured band between  $1250\text{--}975\text{ cm}^{-1}$  reflecting vibration such as  $\nu(\text{Ge-O-Si})$ ,  $\nu(\text{Si-O-Si})$  and  $\nu(\text{Si-OH})$ . All spectra were measured with parallel (pp) and perpendicular (vp) polarized light.  $T=15^\circ\text{C}$ ; Angle of incidence  $\theta=45^\circ$ ; Number of active internal reflections  $N=19.4$ .

The relevant parameters used for quantitative analysis are summarized in Table 1. The surface concentration of the final state of the silane layer in the S-cuvettes was calculated by means of eq. (28) that is repeated for the convenience of the reader:

$$\Gamma = \frac{\int A_{pp/vp}(\tilde{\nu})d\tilde{\nu}}{3\nu \cdot N \cdot d_{e,pp/vp}^{rel,iso} \int \varepsilon(\tilde{\nu})d\tilde{\nu}} \left[ 2 - \frac{E_x^2}{E_z^2} + R \frac{E_y^2}{E_z^2} \right]$$

By using integrated absorbancies of symmetric and asymmetric CH<sub>2</sub> stretching vibrations (Table 2) the surface concentration resulted in  $\Gamma_{exp} = (6.33 \pm 0.70) \times 10^{-10}$  mol/cm<sup>2</sup>. From this quantity, one may estimate the mean layer thickness  $d$ , based on the film density of  $\rho \approx 0.90 \pm 0.10$  g/cm<sup>3</sup> [109] and the molecular mass  $M_r = 187.15$  g/mol to be  $d \approx (\Gamma_{exp} \times M_r) / \rho = 1.3 \pm 0.2$  nm. It should be noted that Si-Cl was replaced by Si-O when calculating  $M_r$ , since no Si-Cl vibrations were detectable in the final layer as documented by measurements with a CdTe MIRE, see later.

Table 1. Magnitudes and uncertainties of input parameters. For determination of integrated molar absorption coefficients of  $\nu_s(\text{CH}_2)$  and  $\nu_{as}(\text{CH}_2)$  see Appendix 6.3.

<i>Parameter, Symbol</i>	<i>Magnitude</i>
Angle of incidence, $\theta/\text{deg}$	$45.0 \pm 1.5$
Refractive index of germanium MIRE, $n_1$	$4.0 \pm 0.0$
Refractive index of an adsorbed/bound layer, $n_2$	$1.45 \pm 0.05$
Refractive index of toluene environment, $n_3$	$1.49 \pm 0.05$
Integrated molar absorption coefficient of $\nu_s(\text{CH}_2)$ , $\int \varepsilon(\tilde{\nu})d\tilde{\nu} / 10^5 \text{ cm/mol}$	$2.95 \pm 0.33$
Integrated molar absorption coefficient of $\nu_{as}(\text{CH}_2)$ , $\int \varepsilon(\tilde{\nu})d\tilde{\nu} / 10^5 \text{ cm/mol}$	$10.9 \pm 1.16$
Number of equal functional groups per molecule, $\nu$	$6 \pm 0$
Number of active internal reflections, $N$	$19.4 \pm 1$

For the estimation of upper and lower limits for the area per 7-OTCS molecule after immobilization on the Ge plate, two boundary states were considered from molecular modeling calculation, Figure 19 (HyperChem (TM), Hypercube, Inc., 1115 NW 4th Street, Gainesville, Florida 32601, USA). Aligning the hydrocarbon chain vertically (Figure 19A) would result in the minimum area of  $A_{min} = 34 \text{ \AA}^2$  per molecule which corresponds to a surface concentration of  $\Gamma_{max} = 4.88 \times 10^{-10}$  mol/cm<sup>2</sup>. If the molecules lie on the Ge plate (Figure 19B) they occupy an area of  $A_{max} = 69 \text{ \AA}^2$  per molecule which corresponds to a surface concentration of  $\Gamma_{min} = 2.41 \times 10^{-10}$  mol/cm<sup>2</sup>. The experimentally determined mean surface concentration of  $\Gamma_{exp} = 6.33 \times 10^{-10}$  mol/cm<sup>2</sup> is

about 30 % above the most densely packed monolayer coverage and indicates that most probably polymerization has occurred as a parallel reaction to covalent binding to the Ge surface.

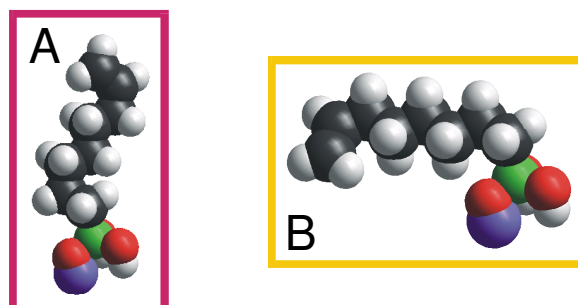


Figure 19. Two conformations of 7-OTCS molecules covalently bound to a Ge atom (violet) used for the estimation of upper and lower limits for the area per 7-OTCS molecule. The chemical structures were drawn with the help of Hyperchem.

The mean direction of the transition moments of symmetric  $\nu_s(\text{CH}_2)$  and asymmetric  $\nu_{as}(\text{CH}_2)$  stretching vibrations with respect to the z-axis may be estimated from the corresponding experimentally determined dichroic ratios  $R$ , according to eq. (19). The relevant data are summarized in Table 2. Averaging the dichroic ratios of both vibrations results in  $R_{\text{exp}}=1.60\pm0.09$  which results in a mean angle between the corresponding transitions moments and the z-axis of  $\Theta=61.6^\circ\pm0.3^\circ$ . Since these transition moments are normal to the local molecular axis one may estimate the mean direction of the hydrocarbon chains of the silane assembly to be inclined by  $\delta=28.4^\circ\pm0.3^\circ$  against the normal to the MIRE (z-axis). It should be noted that an isotropic thin layer would exhibit a dichroic ratio of  $R_{\text{iso}}=2.13\pm0.27$  which is significantly different from the experimental value. This finding is supported by the calculation of the mean segmental order parameter of the hydrocarbon chain  $S_{\text{seg}}=-0.16\pm0.01$  and the corresponding molecular order parameter  $S_{\text{mol}}=0.64\pm0.34$ . For perfect alignment of the hydrocarbon chain along the normal to the plate one would expect  $S_{\text{seg},z}=-0.50$  and  $S_{\text{mol},z}=1.00$ , see Table 2 and ref. [91].

Table 2. Quantitative data summary of surface concentration and orientation of silane layer based on the evaluation of CH<sub>2</sub> symmetric and asymmetric stretching vibrations.

	$\nu_s(\text{CH}_2)$	$\nu_{as}(\text{CH}_2)$
Integration limits/cm <sup>-1</sup>	2873-2823	2968-2898
$\int A_{pp}(\tilde{\nu}) d\tilde{\nu}$	$0.044 \pm 0.003$	$0.192 \pm 0.001$
$\int A_{vp}(\tilde{\nu}) d\tilde{\nu}$	$0.028 \pm 0.002$	$0.117 \pm 0.006$
$R_{\text{exp}}$	$1.55 \pm 0.15$	$1.64 \pm 0.08$
$\Gamma_{\text{exp}}/10^{-10} \text{ mol/cm}^2$	$5.92 \pm 0.69$	$6.75 \pm 0.69$
$d/\text{nm}$	$1.28 \pm 0.14$	$1.48 \pm 0.16$
$\langle \cos^2 \Theta \rangle$	0.21	0.24
$\Theta /^\circ$	$62.4 \pm 0.5$	$60.9 \pm 0.4$
$S_{\text{seg}}$	$-0.17 \pm 0.01$	$-0.145 \pm 0.009$
$S_{\text{mol}}$	$0.71 \pm 0.37$	$0.57 \pm 0.30$

### 4.1.3 Background compensation

#### 4.1.3.1 Background compensation of the final OCS-layer

In a typical silanization experiment the silane layer was bound to the Ge MIRE in the S channel, while R channel served as reference. Corresponding SBSR pp- and vp-spectra of the final silane layer in toluene are shown in Figure 20 featuring background (toluene) overcompensation. This background overcompensation occurred due to the existence of a surface layer in the S channel which has displaced toluene.



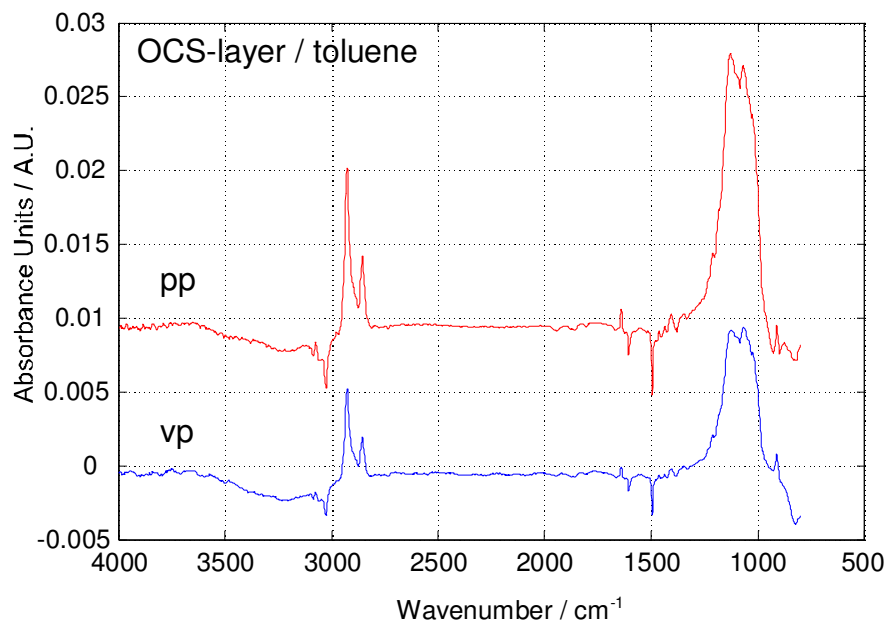


Figure 20. SBSR FTIR pp- and vp-spectra of the OCS-layer in toluene bound to the Ge MIRE only in the S cuvettes while R cuvettes were filled with pure toluene.  $T=15^{\circ}\text{C}$ ; Angle of incidence  $\theta=45^{\circ}$ ; Number of active internal reflections  $N=19.4$ .

Overcoming of the overcompensation could not be simply done since the evanescent wave penetrates proportionally to its wavelength into the rarer medium. Therefore, a linear scaling of the pure toluene spectrum was required.

Subtraction procedure required the absorbance spectrum of toluene displaced by the layer of thickness  $d_0$ . Calculation of this toluene spectrum (ranging from 0 to  $d_0$ ) was performed by scaling down measured pure toluene spectrum (from 0 to  $\infty$ ) by the scaling factor  $\kappa_1$  (eq. (33)). For convenience of the reader the relevant equation is repeated:

$$\kappa_1 = 4\pi\sqrt{n_1^2\sin^2\theta - n_3^2} \cdot d_0 \cdot \tilde{\nu}$$

where  $n_1$  denotes refractive index of Ge MIRE,  $n_3$  the refractive index of bulk,  $\theta$  the angle of incidence,  $d_0$  the layer thickness,  $\tilde{\nu}$  the wavenumber.

Before the scaling of the spectrum, limits of the linear baseline for a chosen solvent marker band had to be accurately set avoiding overlapping with other real bands. For toluene marker band at  $1496\text{ cm}^{-1}$  baseline limits were set to  $1510$  and  $1480\text{ cm}^{-1}$ . The scaling of the overcompensated measured spectrum was performed in small portions (Figure 21) till undercompensation was achieved resulting in a set of integrals depending on  $d_0$ . The adequate  $d_0$  value was obtained when the integral became zero. When such toluene spectrum was added to the SBSR spectrum of the

final OCS-layer complete background compensation was achieved with the known amount of added toluene. Corresponding spectra are shown in Figure 22.

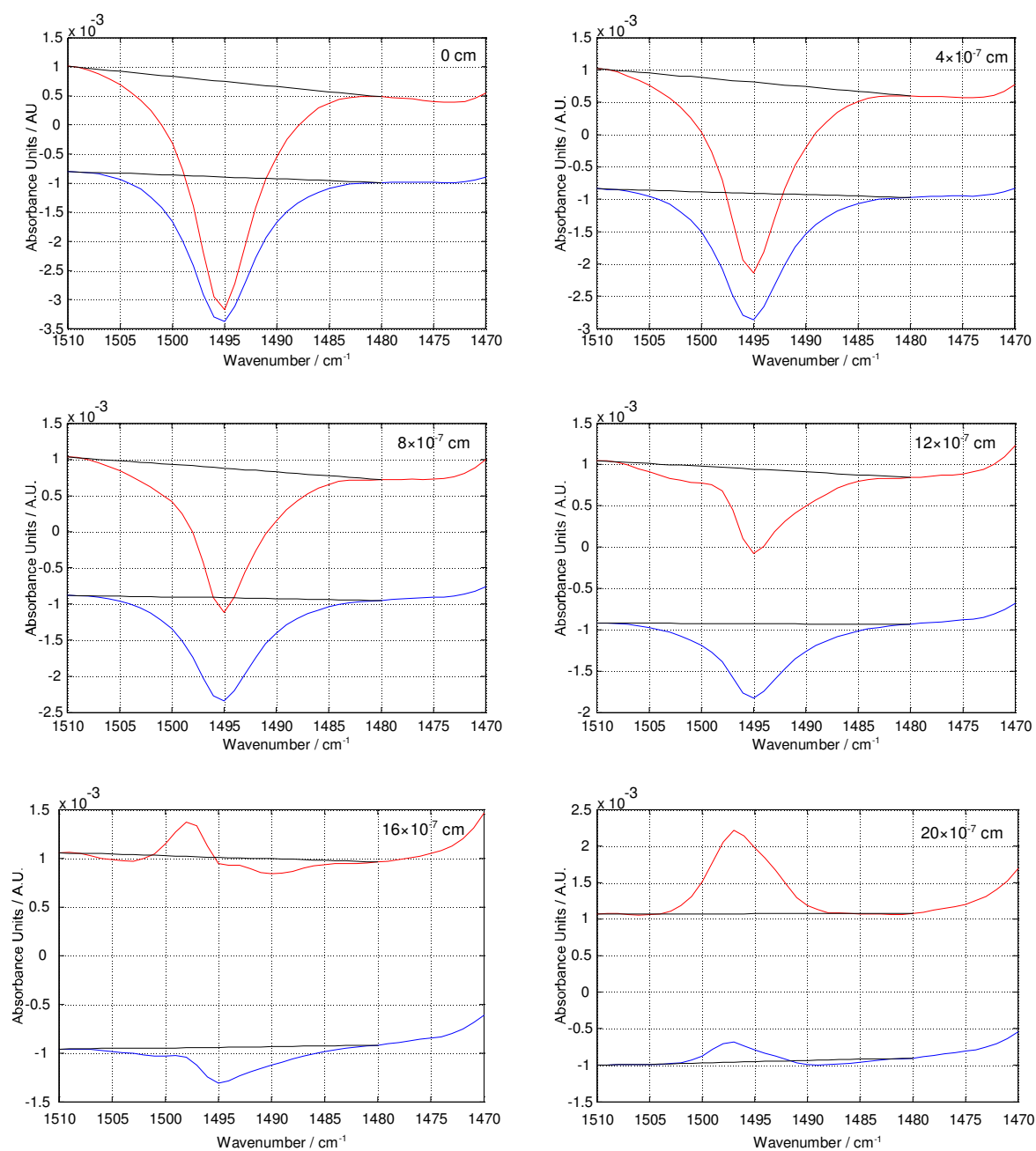


Figure 21. Automatic integration of the solvent marker band at  $1496\text{ cm}^{-1}$  for different toluene thicknesses: 0, 4, 8, 12, 16 and  $20 \times 10^{-7}\text{ cm}$ . SBSR FTIR pp- and vp- spectra of the final silane layer in toluene in the S cuvette, pure toluene in the R cuvettes.

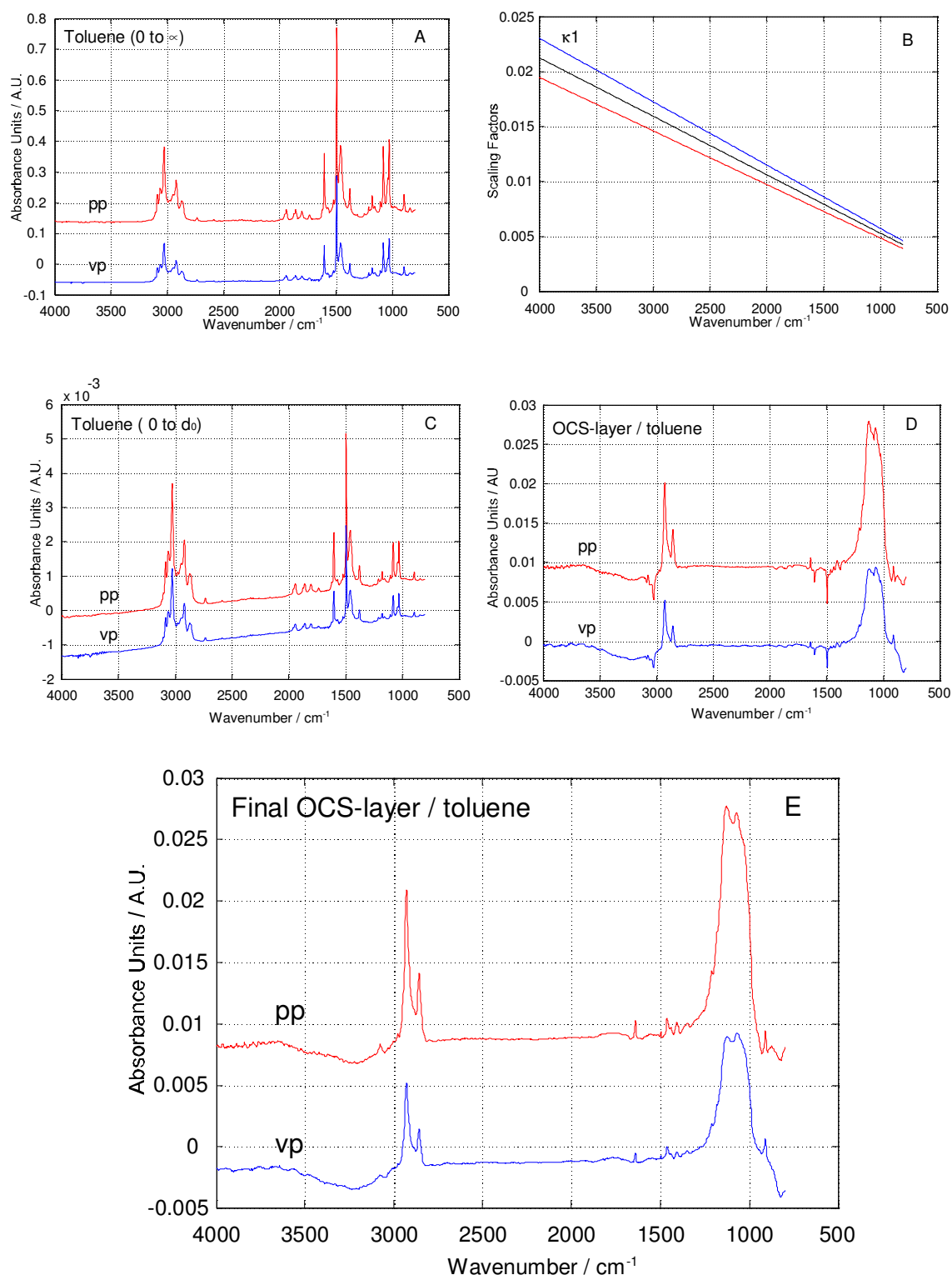


Figure 22. A. Absorbance FTIR pp- and vp-spectra of toluene, reference: clean Ge MIRE; B. The scaling factor  $\kappa_1$ ; C. Calculated absorbance FTIR pp- and vp-spectra of toluene displaced by the layer of thickness  $d_0$ ; D. SBSR pp- and vp-spectra of OCS-layer in toluene, reference: toluene; E. Compensated SBSR pp- and vp-spectra of the final OCS-layer in toluene, reference: toluene.  $T=15^\circ\text{C}$ ; Angle of incidence  $\theta=45^\circ$ ; Number of active internal reflections  $N=19.4$ .

Figure 23 shows integral of pp- and vp-marker band incompensation depending on toluene thickness.

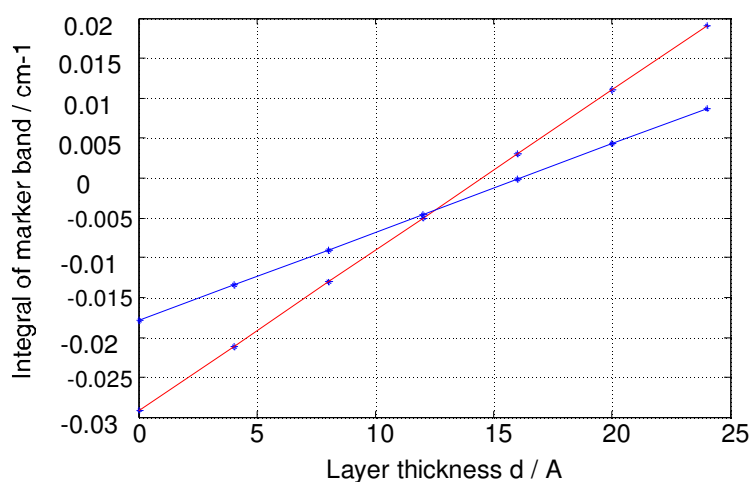


Figure 23. Integral of pp- and vp-marker band incompensation depending on assumed toluene thickness.

The zero-crossing of the integration of toluene marker band from Figure 23 corresponds to toluene thicknesses of 14.50 and 16.11 Å calculated separately for pp- and vp-spectrum. The mean toluene thickness displaced by the silane layer results in 15.31 Å.

#### 4.1.3.2 Background compensation of the time-resolved spectra of OCS-layer growth

The background overcompensation of the time-resolved spectra occurred due to 7-OTCS solution displacement by the growing layer as well as toluene dilution by 7-OTCS molecules. Time-resolved spectra of the growing OCS-layer in contact with 7-OCTS solution in the S channels are shown in Figure 24 (the R channels: pure toluene). In this case 7-OCTS solution formed the background during the layer growth.

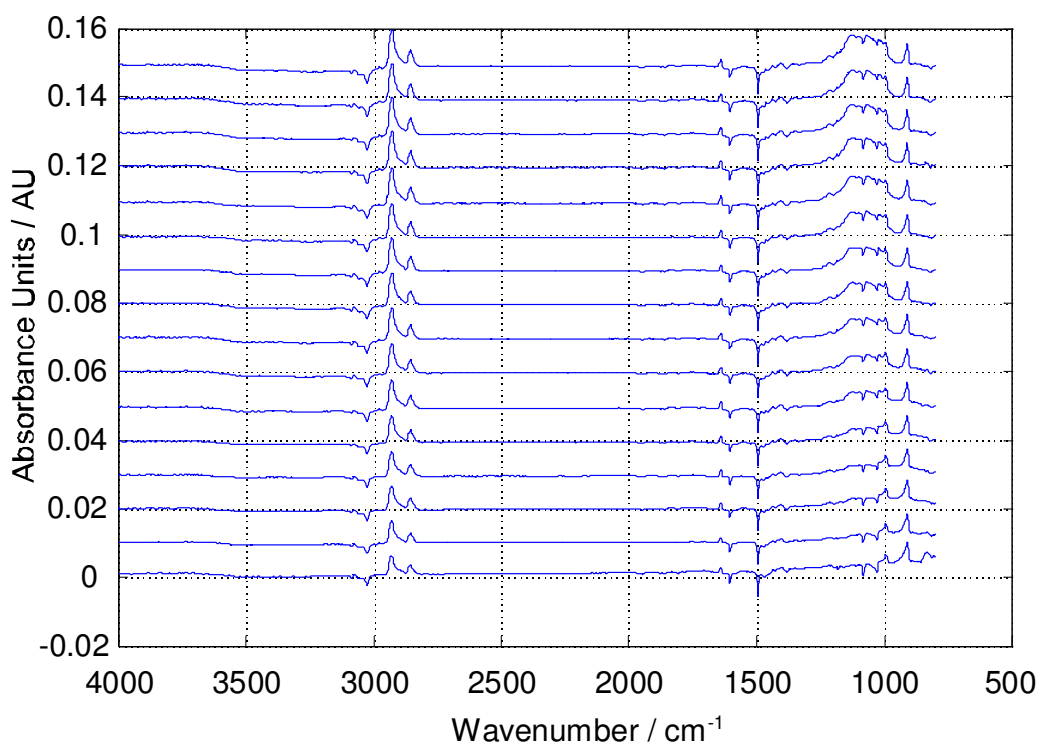


Figure 24. Measured time-resolved SBSR pp-spectra of the OCS-layer growth in contact with 7-OTCS solution in the S channel; pure toluene as reference in the R channels.

$T=15^{\circ}\text{C}$ ; Angle of incidence  $\theta=45^{\circ}$ ; Number of active internal reflections  $N=19.4$ .

In order to perform adequate background compensation of time-resolved spectra a reference spectrum reflecting only dissolved 7-OTCS was required. Since there was no direct experimental possibility to get such reference spectrum due to high reactivity of 7-OTCS molecules to Ge MIRE, theoretical reconstruction of such a reference spectrum was performed.

The compensated SBSR spectrum of the silane layer in the range from 0 to  $d_0$  (Figure 22, E) was subtracted from the last measured time-resolved spectrum of the OCS-layer in contact with 7-OTCS solution resulting in the 7-OTCS solution spectrum ranging from  $d_0$  to infinity. Calculated spectrum was scaled down by scaling factor  $\kappa_2$  (eq. (36)) to 7-OTCS solution spectrum ranging from 0 to  $\infty$ . The equation of the scaling factor  $\kappa_2$  is repeated for the convenience of the reader:

$$\kappa_2 = e^{\frac{2 \cdot d_0}{d_p}}$$

Corresponding spectra are shown in Figure 25.

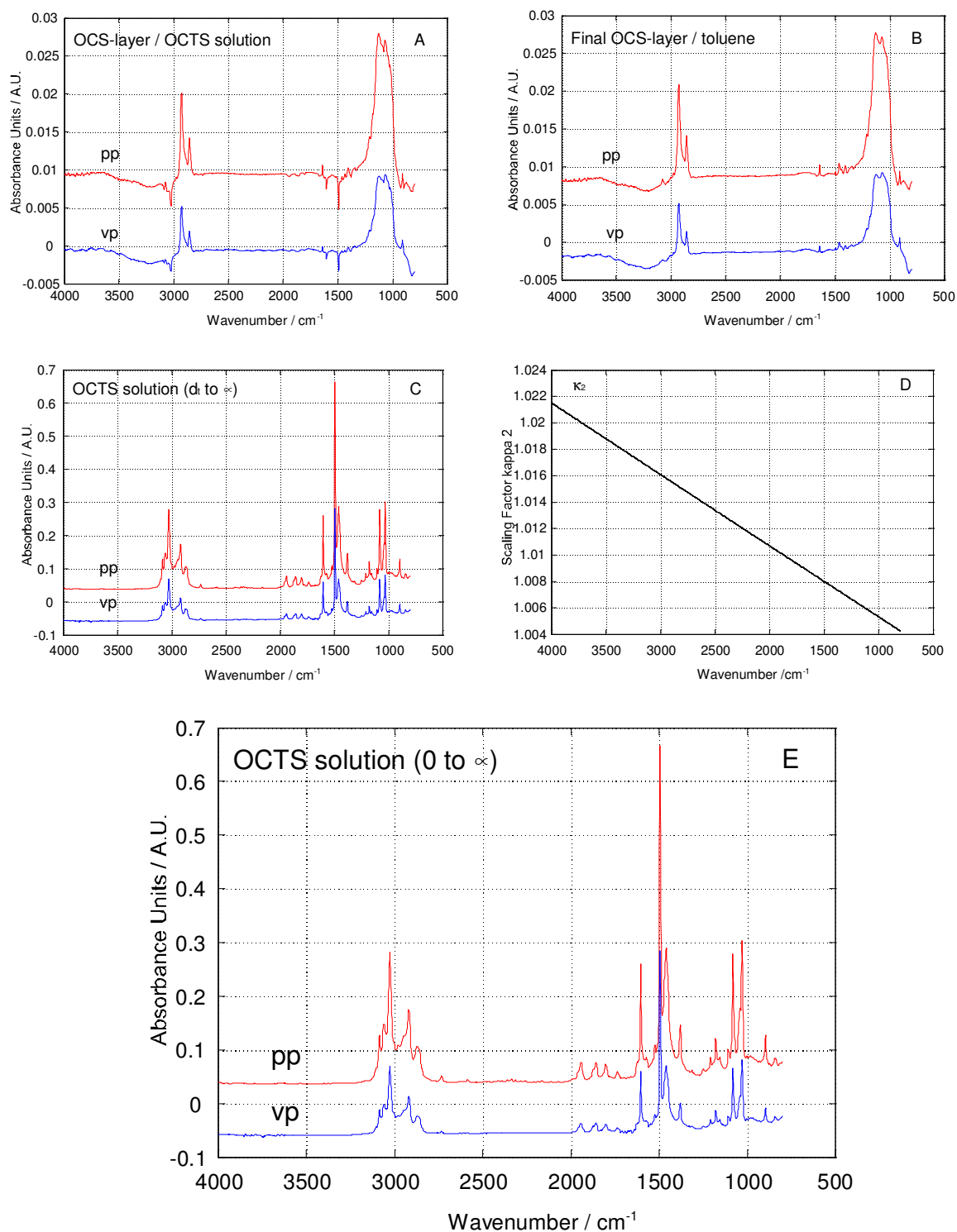


Figure 25. Calculation of the experimentally not accessible pp- and vp-spectra of 7-OTCS solution ranging from zero to infinity. A. SBSR spectra of OCS-layer in 7-OTCS solution in the S channel, pure toluene as reference in the R channel; B. SBSR spectra of the final OCS-layer in toluene in the S channel, pure toluene as reference in the R channel; C. Calculated spectra of 7-OTCS solution ranging from  $d_0$  to  $\infty$ ; D. Scaling factor  $\kappa_2$ ; E. Calculated spectra of 7-OTCS solution ranging from 0 to  $\infty$ . T=15°C; Angle of incidence  $\theta=45^\circ$ ; Number of active internal reflections N=19.4.

This calculated spectrum of 7-OCTS solution (0 to  $\infty$ ) is used as a new artificial reference for background subtraction of time-resolved spectra. For each time point artificial reference spectrum is scaled down by scaling factor  $\kappa_1$  and added to the corresponding time-resolved spectrum removing background overcompensation. Final compensated time-resolved spectra of OCS-layer are shown in Figure 26.

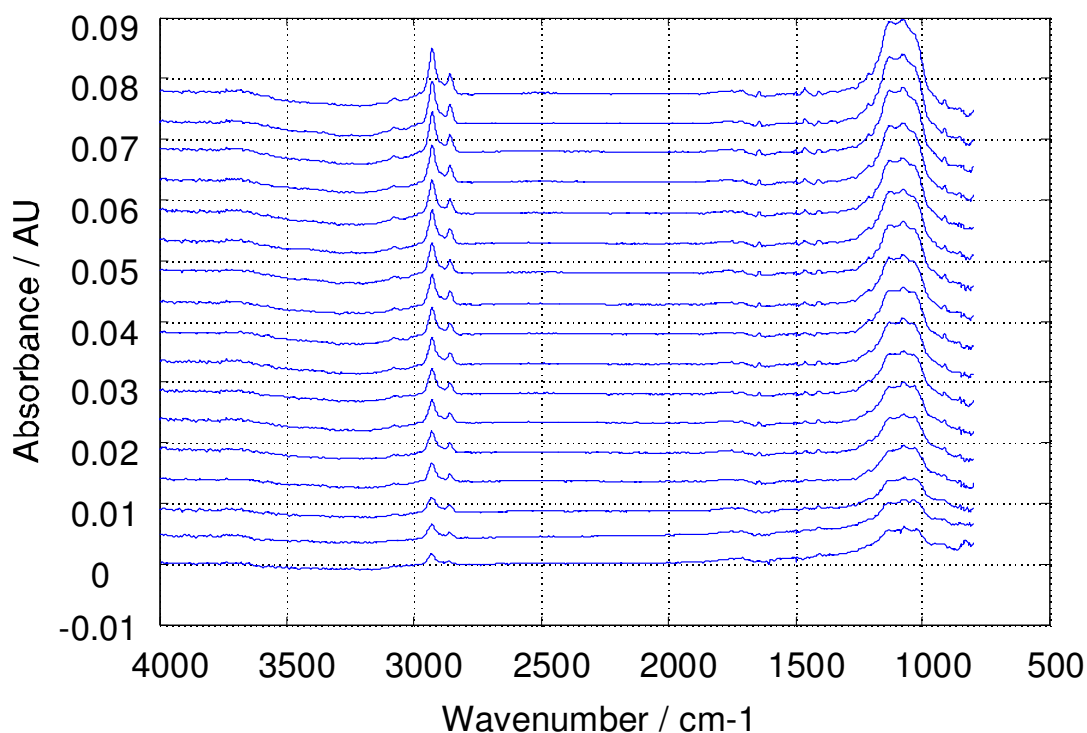


Figure 26. Background compensated time-resolved FTIR pp-spectra of the growing OCS-layer in the S channels, toluene in the R channels as reference.  $T=15^{\circ}\text{C}$ ; Angle of incidence  $\theta=45^{\circ}$ ; Number of active internal reflections  $N=19.4$ .

#### 4.1.4 Kinetics of the silane layer formation

In Figure 27 integrated absorbances of  $\nu_s(\text{CH}_2)$ ,  $\nu_{as}(\text{CH}_2)$ , and  $\nu(\text{C}=\text{C})$  vibrations are fitted according to already suggested exponential growth of silane layers (eq. (40)) consisting of two kinetic regions:

$$I = \left[ A \left( 1 - e^{-\frac{t_f}{\tau_1}} \right) + B \left( 1 - e^{-\frac{t_f}{\tau_2}} \right) \right] \quad (40)$$

where  $I$  denotes integrated absorbance,  $A$  and  $B$  are constants related to the relative amounts of bound monolayer and polymerized multilayer, respectively;  $t_f$  (sec) is a certain time point during the reaction.

Different time constants  $\tau_1$  and  $\tau_2$  indicate different kinetics for both parts of the kinetic curves. Time constant  $\tau_1$  is related to a fast initial attachment of 7-OTCS molecules to the hydroxylated Ge surface while time constant  $\tau_2$  shows much slower rearrangement of attached silane molecules and probably multilayer formation.

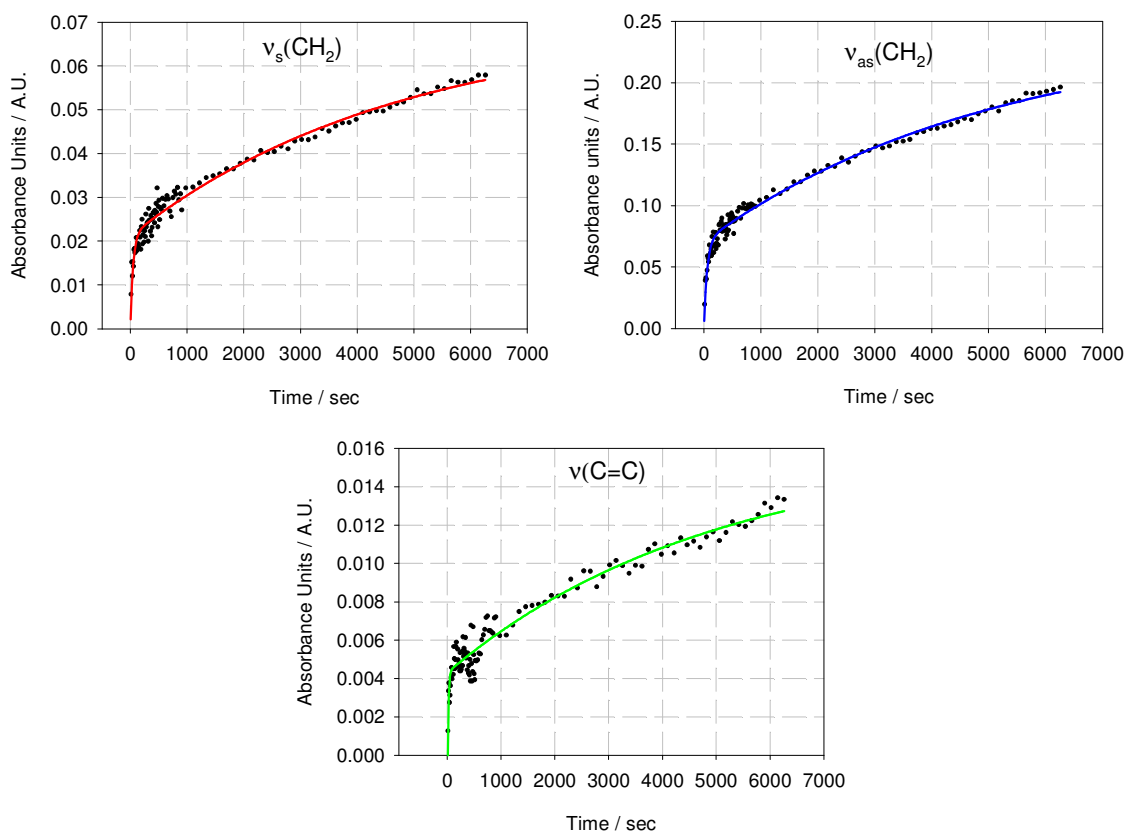


Figure 27. Integrated absorbances (pp) of  $\nu_s(\text{CH}_2)$ ,  $\nu_{as}(\text{CH}_2)$  and  $\nu(\text{C}=\text{C})$  during the layer growth (points) as a function of time. Fitting of data (solid line) is performed according to eq. (40). For the time-resolved SBSR spectra, the growing of the OCS-layer in 7-OTCS solution is used as sample and pure toluene spectrum as reference.

For determination of kinetic constants of symmetric and asymmetric  $\text{CH}_2$  vibrations as well as of a double bond  $\text{C}=\text{C}$  vibration time dependant integrated absorbances have been used (Figure 27). Table 3 shows time constants  $\tau_1$  and  $\tau_2$  as well as constants A and B for different vibrations  $\nu_s(\text{CH}_2)$ ,  $\nu_{as}(\text{CH}_2)$  and  $\nu(\text{C}=\text{C})$ . By using these calculated constants fitting of experimental data was performed separately for two kinetic regions (Figure 28).



Table 3. Time constant of symmetric and asymmetric  $\nu(\text{CH}_2)$  stretching vibrations and  $\nu(\text{C}=\text{C})$  vibration for the layer growth.

Vibration	Time constant, $\tau_1$ ( $\text{sec}^{-1}$ )	Time constant, $\tau_2$ ( $\text{sec}^{-1}$ )	A	B
$\nu_s(\text{CH}_2)$	48	4720	0.021	0.048
$\nu_{as}(\text{CH}_2)$	57	5102	0.071	0.172
$\nu(\text{C}=\text{C})$	36	5492	0.004	0.012

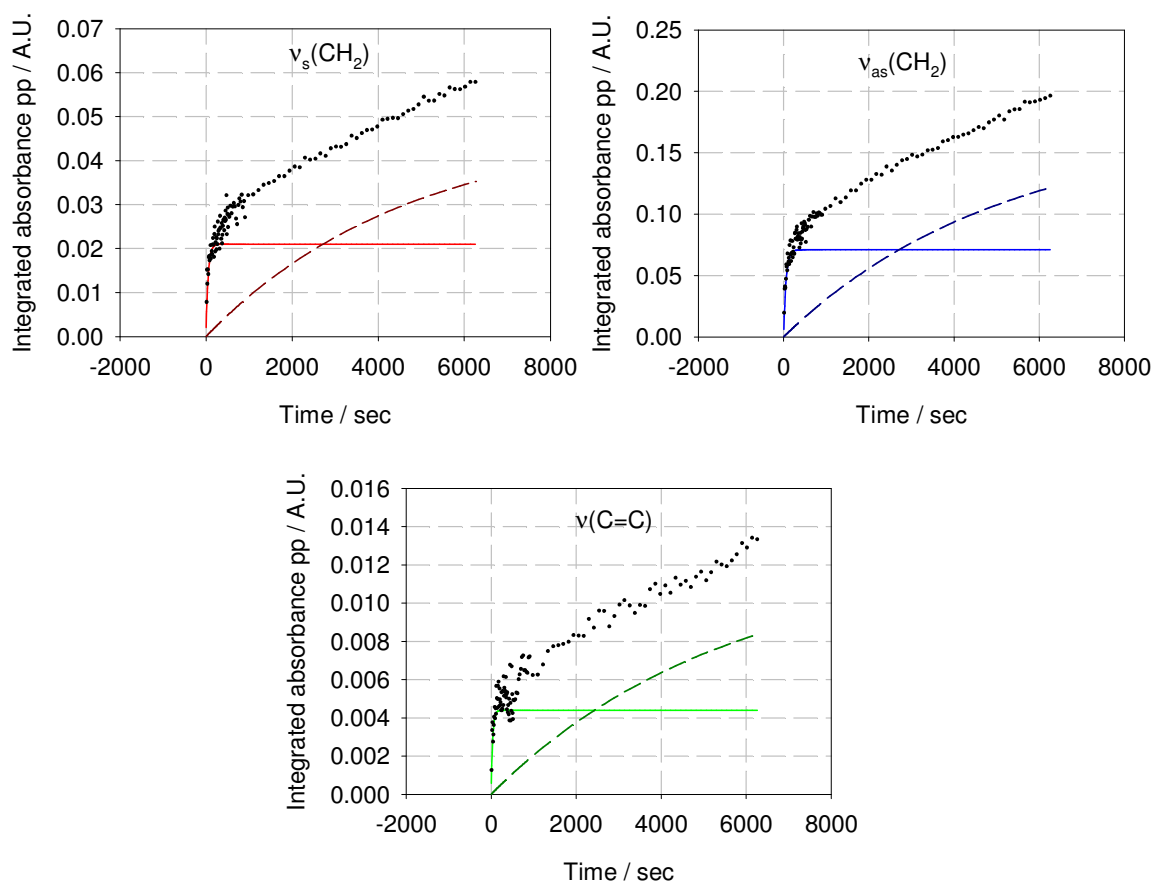


Figure 28. Fitting of experimental data (black points) by two separated kinetic regions related to fast initial attachment of 7-OTSC molecules to the hydroxylated Ge MIRE (solid line) and rearrangement of the attached silane molecules on the surface (dashed line).

In Figure 28 two parallel reactions are separated from each other during silanization. When very reactive 7-OTCS molecules reached Ge surface, very fast reaction related to the formation only of Ge-O-Si bonds occurred within approx. 50sec (solid line). The second one was much slower process related to the rearrangement of chemisorbed molecules via Si-O-Si bonds formation at  $1200\text{ cm}^{-1}$  as well as polymerization (dashed line).

## 4.2 OXIDATION OF THE SILANE LAYER

### 4.2.1 Oxidation of terminal ethylenic double bond of the silane layer by ozone

The results of oxidation are shown in Figure 29. On top there are 4 selected spectra measured 2, 14, 21 and 32 min after the onset of the ozone flow. The disappearance of typical absorption bands of the double bond is visible at 3077, 1641 and 911  $\text{cm}^{-1}$  (dotted green line). This effect is paralleled by the appearance of a new band at 1718  $\text{cm}^{-1}$  which is tentatively assigned to  $\nu(\text{C}=\text{O})$  of  $-\text{COOH}$  or to an aldehyde  $-\text{CHO}$  (dashed green line). Spectra of the dry layer after oxidation were measured with pp- and vp-polarized incident light and are shown on the bottom of Figure 29. It should be noted that oxidation did not stop completely after removing the end-standing double bond; about 46 % of the saturated hydrocarbon chains have also been removed under the applied conditions.

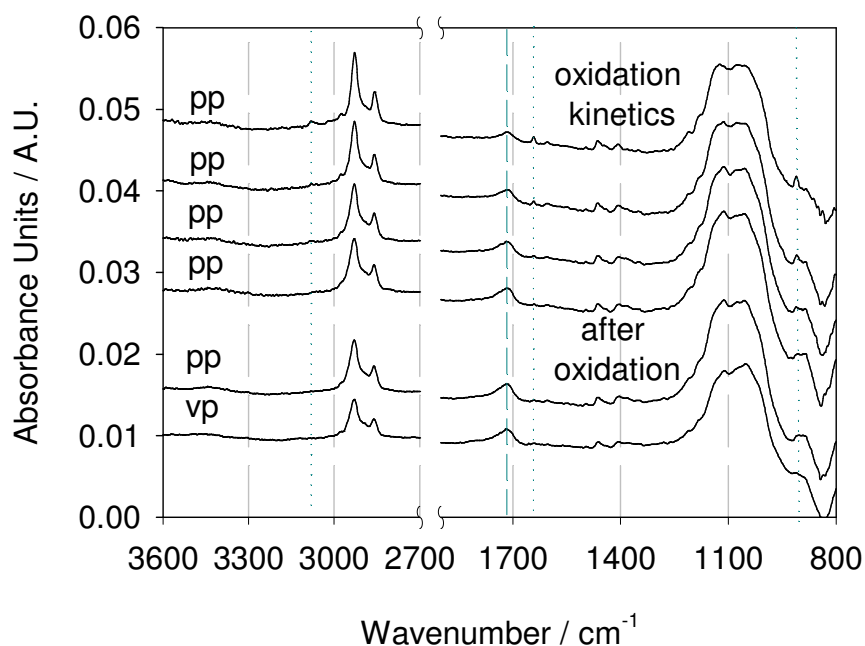


Figure 29. Oxidation of the dry silane layer by ozone produced by means of UV irradiation of an  $\text{Ar}/\text{O}_2$  mixture. On top there are time-resolved SBSR spectra recorded after 2, 14, 21 and 32 min of exposure to ozone. The last two spectra on bottom are SBSR spectra measured after complete oxidation of the double bond. A new band appeared at 1718  $\text{cm}^{-1}$  featuring the reaction product  $-\text{COOH}$ . However, it should be noted that  $\nu_s(\text{CH}_2)$  decreased also by 46 % reflecting that even parts of the saturated hydrocarbon chains have been oxidized during ozone exposure. Reference for all spectra: dried Ge MIRE.  $T=15^\circ\text{C}$ ; Angle of incident light  $\theta=45^\circ$ ; Number of active internal reflections  $N=19.4$ .

#### 4.2.2 Proof of the existence of end-standing COOH groups

Validation of the existence of end-standing COOH groups was performed by exposing oxidized layer to aqueous solutions at pH 4 and pH 8, respectively, at  $T=22\text{ }^{\circ}\text{C}$ . Two independent experiments, stationary and ME, were performed.

In Figure 30 stationary SBSR FTIR spectra show a reversible protonation and deprotonation of COOH groups during exposition to different buffer solutions. Top: difference between the SBSR spectra of the oxidized silane layer in different buffer solutions of pH 8 and pH 4 above the oxidized silane layer in the S cuvettes; corresponding buffer solution above clean Ge MIRE in the R cuvettes. Bottom: difference between the SBSR spectra of the oxidized silane layer in different buffer solutions of pH 4 and pH 8 above the oxidized silane layer in the S cuvettes; corresponding buffer solution above clean Ge MIRE in the R cuvettes. Deprotonation features symmetric  $\nu_s(\text{COO}^-)$  and asymmetric  $\nu_{as}(\text{COO}^-)$  stretching vibrations placed at  $1406$  and  $1550\text{ cm}^{-1}$ , respectively, while protonation is characterized by  $\nu(\text{C=O})$  of carboxyl stretching vibration near  $1713\text{ cm}^{-1}$ . This reversible response between carboxyl and carboxylate groups unambiguously confirmed existence of the end-standing COOH groups of the silane layer.

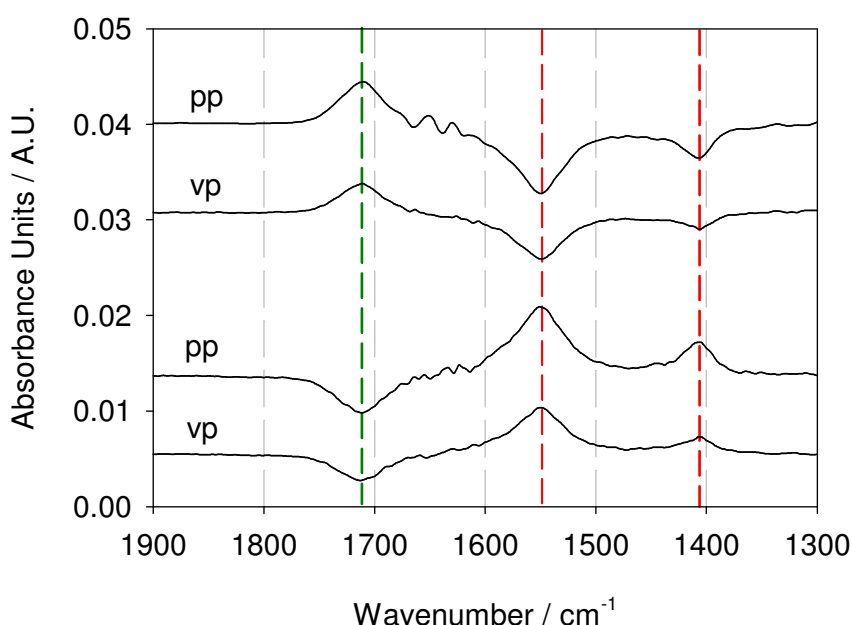


Figure 30. The reversible change between carboxyl stretching vibrations at  $1713\text{ cm}^{-1}$  and carboxylate asymmetric and symmetric stretching vibrations at  $1550$  and  $1406\text{ cm}^{-1}$  of the oxidized silane layer, respectively. Top: difference between the SBSR spectra of the oxidized silane layer in different buffer solutions of pH 8 and pH 4 above the oxidized

silane layer in the S cuvettes; corresponding buffer solution above clean Ge MIRE in the R cuvettes. Bottom: difference between the SBSR spectra of the oxidized silane layer in different buffer solutions of pH 4 and pH 8 above the oxidized silane layer in the S cuvettes; corresponding buffer solution above clean Ge MIRE in the R cuvettes. The reversible response of the oxidized layer unambiguously confirms the existence of COOH and COO<sup>-</sup>. T=22°C; Angle of incident light  $\theta=45^\circ$ ; Number of active internal reflections N=19.4.

The most sensitive technique, i.e., chemical modulated excitation (c-ME), has also been applied. The results are presented in Figure 31 and Figure 32. The excitation of the immobilized layer was performed by periodic exchanges of the buffer solutions (pH 4 and 8) in the S-cuvettes. Since the two buffer solutions are expected to have different IR spectra, the same ME was also performed in the R-cuvettes as a reference. Phase resolved spectra according to eq. (39) are presented in Figure 31A and B, while Figure 32A and B represent difference ME spectra of Figure 31B and A, revealing the layer response to pH changes. The result is unambiguous: pH 8 results in the two expected stretching vibrations of the -COO<sup>-</sup> group, while pH 4 restores reversibly the protonated state of the silane layer.

For the sake of clarity, some remarks concerning ME technique should be made. (i) Demodulation was performed only in the fundamental, i.e. for  $k=1$  in eq. (39), (ii) At operators phase setting  $\phi_k^{\text{PSD}} \approx 82^\circ$ , all signals vanish in the whole spectral range. According to eq. (39) this means that the systems response exhibits the same phase shift  $\phi_k \approx 82^\circ$  for all bands. As a consequence this experiment does not reveal any phase resolution, i.e., kinetic information on protonation and deprotonation, as to be expected when considering the excitation period of  $T = 5$  min. The phase delay of  $\phi_k \approx 82^\circ$  results from the mean time needed to exchange the solutions in the cuvettes of the SBSR flow through cell. (iii) Attention should be drawn to the high stability of background compensation. Even the very intense OH stretching band at  $3400 \text{ cm}^{-1}$  is experimentally completely compensated. Software supported baseline correction is not necessary over the spectral range documenting the high reliability of ME spectra even in the micro-absorbance range.

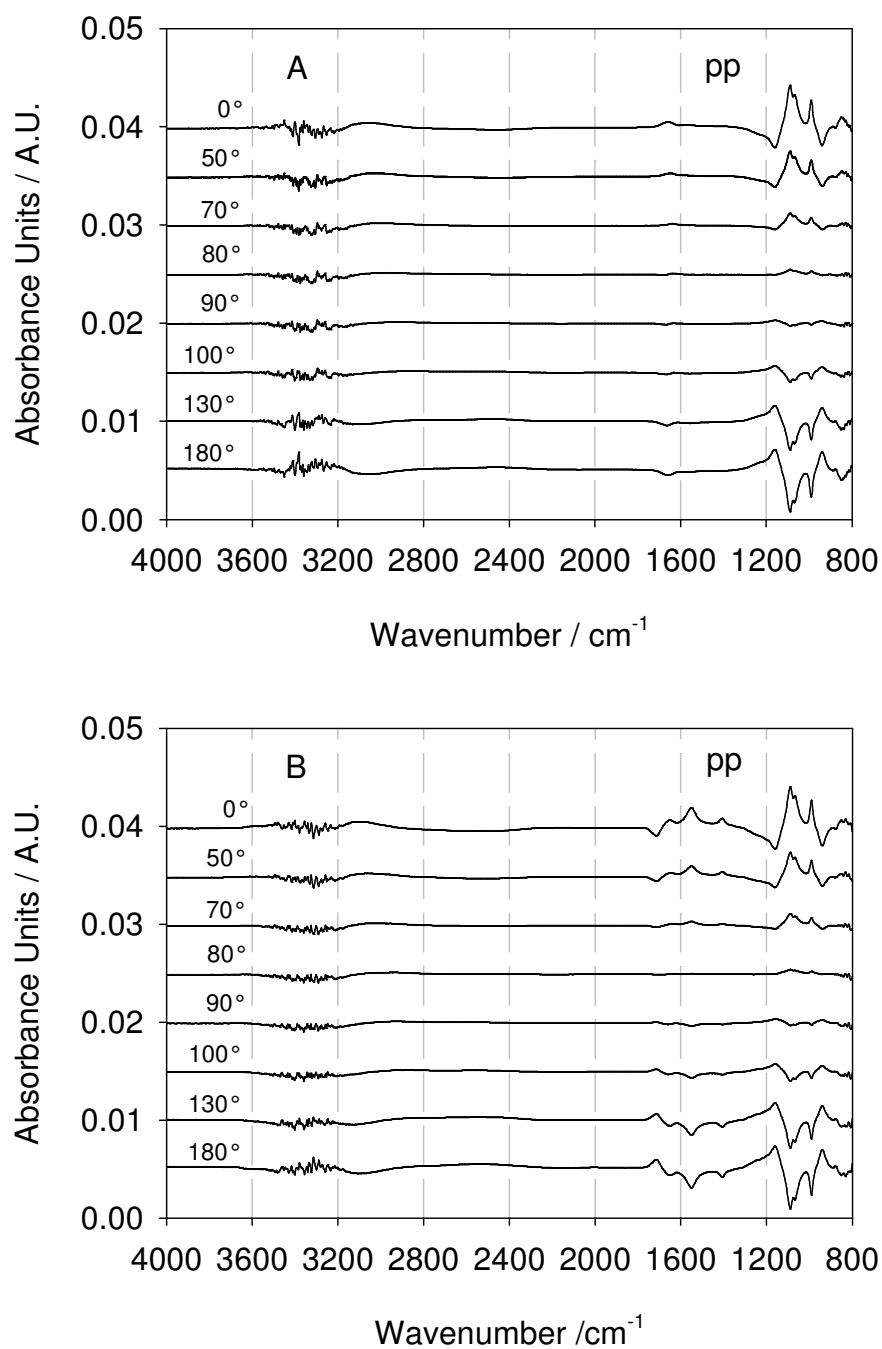


Figure 31. Parallel polarized (pp) phase-resolved absorbance spectra according to eq. (39) obtained by periodic exchange of the buffer solutions (pH 4 and pH 8) in the R cuvettes without layer (A) and in the S cuvettes containing the oxidized layer (B). Modulation period  $T=5$  min;  $T=22^{\circ}\text{C}$ ; Ge MIRE; Angle of incidence  $\theta=45^{\circ}$ ; Number of active internal reflections  $N=19.4$ .

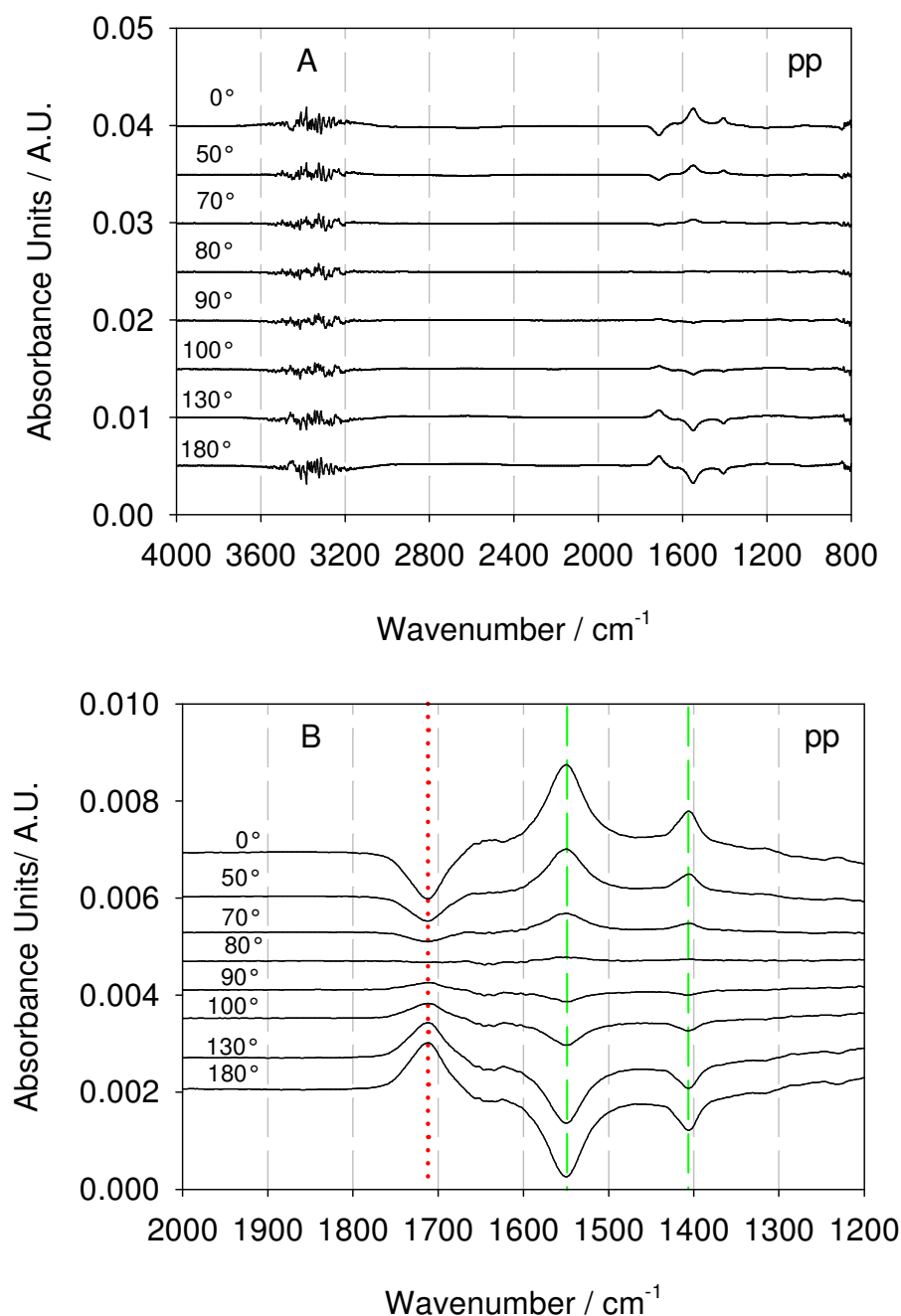


Figure 32. Parallel polarized (pp) phase-resolved difference spectra between the spectra shown in Figure 31B and A, presenting the unperturbed response of the oxidized layer to the periodic pH-change (pH 4, pH 8). Spectra show a reversible change between carboxyl stretching vibration at 1713  $\text{cm}^{-1}$  and carboxylate asymmetric and symmetric stretching vibrations at 1550 and 1406  $\text{cm}^{-1}$ , respectively. A. Full spectral range; B. Expanded spectral range between 2000 and 1200  $\text{cm}^{-1}$ . Note the excellent baseline stability of ME-techniques, which is achieved by pure hardware method. Modulation period  $T=5$  min; Ge MIRE;  $T=22^\circ\text{C}$ ; Angle of incidence  $\theta=45^\circ$ ; Number of active internal reflections  $N=19.4$ .

The relevant parameters used for quantitative analysis of carboxylate vibrations are summarized in Table 4. The surface concentrations of carboxylate  $\nu_{\text{as}}(\text{COO}^-)$  groups of the silane layer calculated by means of eq. (28) was found to be  $\Gamma_{\text{exp}} = (2.43 \pm 0.40) \times 10^{-10} \text{ mol/cm}^2$ .

Table 4. Magnitudes and uncertainties of input parameters. For determination of integrated molar absorption coefficients of  $\nu_{\text{as}}(\text{COO}^-)$  see Appendix 6.4.

<i>Parameter, Symbol</i>	<i>Magnitude</i>
Angle of incidence, $\theta/\text{deg}$	$45.0 \pm 1.5$
Refractive index of germanium MIRE, $n_1$	$4.0 \pm 0.0$
Refractive index of an adsorbed/bound layer, $n_2$	$1.45 \pm 0.05$
Refractive index of bulk (water), $n_3$	$1.31 \pm 0.05$
Integrated molar absorption coefficient of $\nu_{\text{as}}(\text{COO}^-)$ , $\int \epsilon(\tilde{\nu}) d\tilde{\nu} / 10^7 \text{ cm/mol}$	$2.68 \pm 0.33$
Number of equal functional groups per molecule, $\nu$	$1 \pm 0$
Number of active internal reflections, $N$	$27.97 \pm 1$

### 4.3 ACTIVATION OF THE CARBOXYLIC ACID TERMINATED SILANE LAYER

The SBSR spectra of 0.1 M *N*-hydroxysuccinimide (NHS) and 0.4 M *N*-Cyclohexyl-*N'*-(2-morpholinoethyl) carbodiimide metho-*p*-toluenesulfonate (CMC) in water used for the activation of COOH silane layer groups are presented in Figure 33. Typical absorptions in-phase and out-of-phase  $\nu_s(\text{C=O})$  at 1780 and  $\nu_{as}(\text{C=O})$  1709  $\text{cm}^{-1}$  as well as  $\delta(\text{OH})$  vibration at 1630  $\text{cm}^{-1}$  are associated with *N*-hydroxysuccinimide molecule. The *N*-hydroxysuccinimidyl vibrations such as stretching  $\nu(\text{C-N-C})$  and  $\nu(\text{N-C-O})$  were observed at 1230 and 1086  $\text{cm}^{-1}$ , respectively [78]. The spectrum representing CMC displays characteristic bands such as asymmetric stretching of imide  $-\text{N}=\text{C}=\text{N}-$  at 2130  $\text{cm}^{-1}$  and sulphate vibrations between 1300-1000  $\text{cm}^{-1}$ .

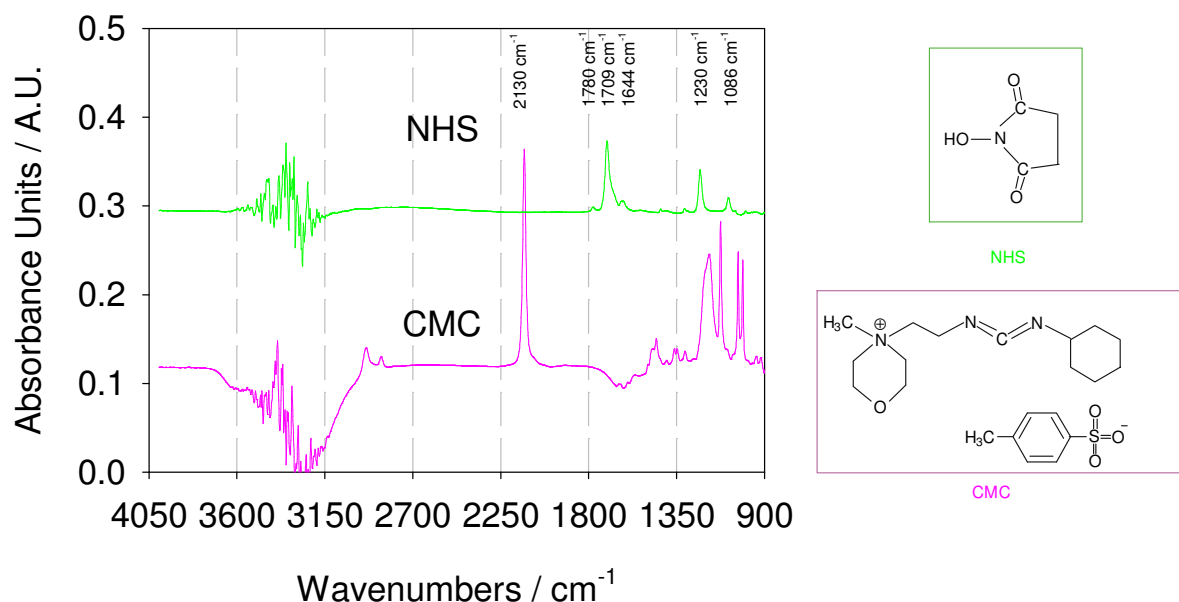


Figure 33. Parallel polarized SBSR FTIR spectra of 0.1M NHS and 0.4M CMC in water, separately, above Ge MIRE in the S cuvettes; water in the R cuvettes.  $T=25^{\circ}\text{C}$ ; Angle of incidence  $\theta=45^{\circ}$ ; Number of active internal reflections  $N=27.97$ .

#### 4.3.1 NHS effect on the carboxyl silane layer groups

Activation of the carboxylic acid terminated silane surface was achieved by transformation of the COOH groups into NHS-esters by passing the activation mixture of 0.1 M NHS and 0.4 M CMC at  $\text{pH}=6.1$  over the surface for about 30 min at  $T=25^{\circ}\text{C}$ . Since this activation step took place in an aqueous environment, the SBSR spectrum of carboxylic acid terminated silane layer in ultra-pure deionised water and the SBSR spectrum of NHS-ester modified silane layer served as reference and



sample, respectively. Difference between these two spectra represents the effect of activation, i.e. NHS-ester formation on the silanized Ge surface (Figure 34).

NHS activation effect on the carboxylic terminated silane layer presented in Figure 34 features characteristic  $\nu(\text{C}=\text{O})$  stretching ester vibration at  $1814\text{ cm}^{-1}$  while other typical absorptions such as  $\nu(\text{C}=\text{O})$  symmetric and asymmetric stretchings of the succinimidyl endgroup are placed at  $1781$  and  $1734\text{ cm}^{-1}$ . [78,110,111,112,113] Other absorptions are listed in Table 5.

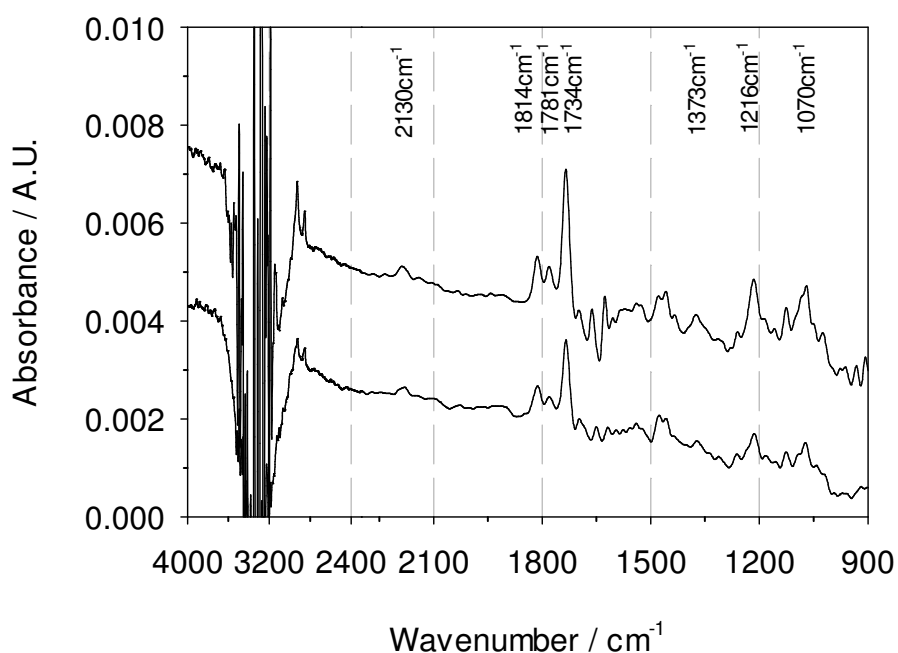


Figure 34. The NHS activation effect. Difference between the SBSR FTIR spectra of the NHS-ester terminated silane layer (sample) and the SBSR FTIR spectra of the carboxylic acid terminated silane layer (reference) in ultra-pure deionised water measured with parallel (pp) and perpendicular (vp) polarized light.  $T=25^{\circ}\text{C}$ ; Angle of incidence  $\theta=45^{\circ}$ ; Number of active internal reflections  $N=26.7$ .

Table 5. Characteristic NHS and CMC vibrations.

Wavenumber / $\text{cm}^{-1}$	Band assignment
2130	$\nu(\text{-N}=\text{C}=\text{N-})$ succinimide stretch
1464	$\delta(\text{CH}_2)$ methylene scissors deformation
1373	$\nu_s(\text{C-N-C})$ symm. succinimide stretch
1216	$\nu_{as}(\text{C-N-C})$ asymm. succinimide stretch
1070	$\nu(\text{C-O-N})$ succinimide stretch
1300-1100	sulphate vibrations

### 4.3.2 The NHS-ester stability

The stability of NHS-esters of a silane layer in water media monitored over 3 days at 25°C is presented in Figure 35. NHS-esters were stable in ultra-pure water approx. 30 min after which slow hydrolyzation occurred during time. It was found that decreasing of  $\nu(\text{C}=\text{O})$  ester vibration at 1814  $\text{cm}^{-1}$  and  $\nu(\text{C}=\text{O})$  symmetric and asymmetric vibrations of succinimidyl endgroup at 1781 and 1734  $\text{cm}^{-1}$  was followed by the appearance of free  $\nu(\text{C}=\text{O})$  vibrations at 1711  $\text{cm}^{-1}$  and  $\delta(\text{OH})$  at 1640  $\text{cm}^{-1}$  related to released carboxylic groups of the silane layer.

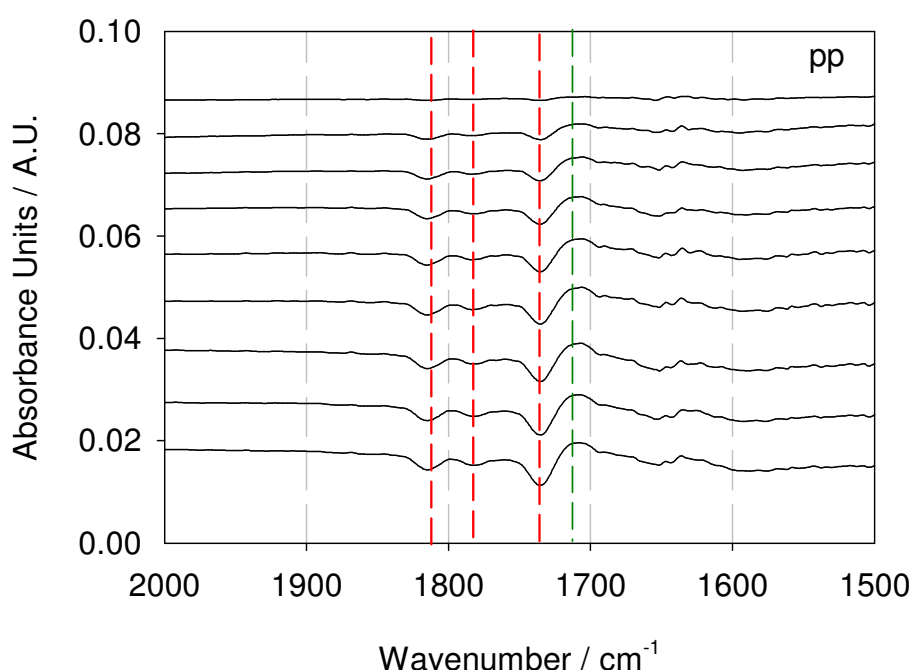


Figure 35. Selected time-resolved parallel polarised (pp) SBSR FTIR spectra of the NHS-ester hydrolyzation in water. The SBSR spectra represent difference between NHS-ester terminated silane layer immediately after its formation (reference) and the SBSR spectra of NHS-ester decomposition measured after 0.38, 7.9, 15.4, 22.6, 30.1, 37.6, 41.4, 48.6 and 56.1 hours (sample). Disappearance of NHS-esters vibrations at 1814, 1781 and 1734  $\text{cm}^{-1}$  was followed by appearance of  $\nu(\text{C}=\text{O})$  and  $\delta(\text{OH})$  vibrations of carboxyl terminated silane layer at 1711 and 1640 $\text{cm}^{-1}$ , respectively. Ge MIRE; T=25°C; Angle of incidence  $\theta=45^\circ$ ; Number of active internal reflections N=25.33.

Kinetic curve fitting of NHS-ester hydrolyzation of the silane layer in water is shown in Figure 36. Integrated absorbances of  $\nu(\text{C}=\text{O})$  ester stretch at 1814  $\text{cm}^{-1}$  and  $\nu(\text{C}=\text{O})$  hydroxysuccinimidyl stretch vibration at 1734  $\text{cm}^{-1}$  were monitored over time. Time constants related to NHS-esters decomposition were determined according to the following exponential equation:

$$A = A_0 + a \left( 1 - e^{-\frac{t}{\tau}} \right) \quad (41)$$

where  $A_0$  denotes initial integrated absorbance,  $a$  constant,  $t$  is reaction time and  $\tau$  is time constant. Time constants related to NHS-ester decompositions were found to be approx. 20 and 30 hours.

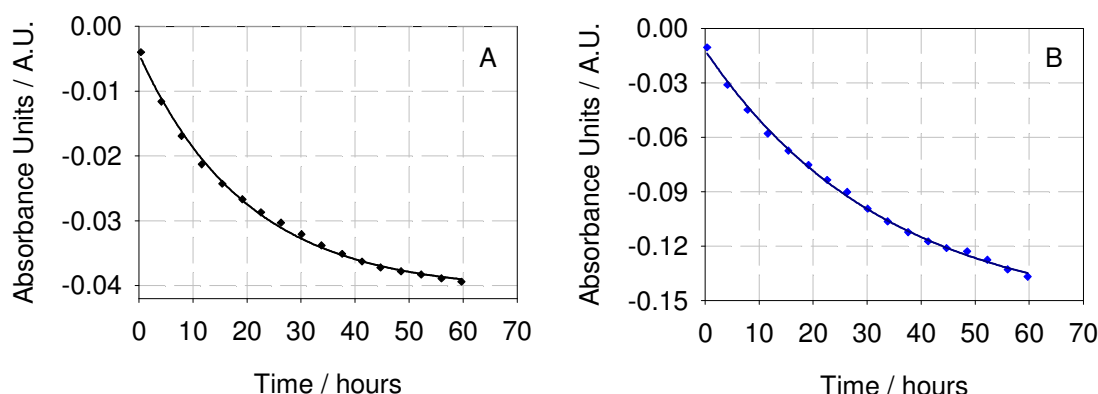


Figure 36. NHS-ester hydrolyzation. Integrated absorbances of  $\nu(\text{C}=\text{O})$  ester stretch vibration at  $1814 \text{ cm}^{-1}$  (A) and  $\nu(\text{C}=\text{O})$  N-hydroxysuccinimidyl stretch vibration at  $1734 \text{ cm}^{-1}$  (B). Initial integrated absorbancies  $A_0$  have found to be 0.041 and 0.16, constants  $a$  0.037 and 0.147, while time constant  $\tau$  related to hydrolyzation kinetic 20 and 30 hours.

### 4.3.3 NHS-ester terminated silane layer

The SBSR spectra of NHS-ester terminated silane layer in  $\text{H}_2\text{O}$  and  $\text{D}_2\text{O}$  are shown in Figure 37. NHS-ester vibrations such as  $\nu(\text{C}=\text{O})$  ester stretching and  $\nu(\text{C}=\text{O})$  symmetric and asymmetric stretchings of the succinimidyl endgroup are placed at  $1814$ ,  $1781$  and  $1734 \text{ cm}^{-1}$ , respectively. We suppose that during  $\text{H}_2\text{O}$  exchange by  $\text{D}_2\text{O}$  a certain amount of NHS-esters was decomposed. Therefore, appearing of a small band at  $\sim 1540 \text{ cm}^{-1}$  indicates probably carboxylate  $\nu_{\text{as}}(\text{COO}^-)$  vibration that has been released during  $\text{H}_2\text{O}$  and  $\text{D}_2\text{O}$  circulation. On the other side, the shoulder of NHS-esters placed at  $1703 \text{ cm}^{-1}$  can be related to  $\nu(\text{C}=\text{O})$  vibration of released or unreacted  $\text{COOH}$  groups of the silane layer. This indicates the mixture of protonated and deprotonated state of the  $\text{COOH}$  groups on the silane surface. The surface concentration of the carboxylate groups of the silane layer in  $\text{D}_2\text{O}$  calculated by means of eq. (28) was found to be  $\Gamma_{\text{exp}} = (0.043 \pm 0.005) \times 10^{-10} \text{ mol/cm}^2$  that is only  $\sim 2\%$  of overall groups produced by oxidation not taking into account protonated  $\text{COOH}$ . The relevant parameters used for quantitative analysis are summarized in Table 6.

Since there was a small D<sub>2</sub>O contamination by H<sub>2</sub>O indicated by the existence of  $\nu(\text{OH})$  vibration at  $\sim 3400\text{ cm}^{-1}$ , vibration at  $1640\text{ cm}^{-1}$  could be assigned to  $\delta(\text{OH})$ .

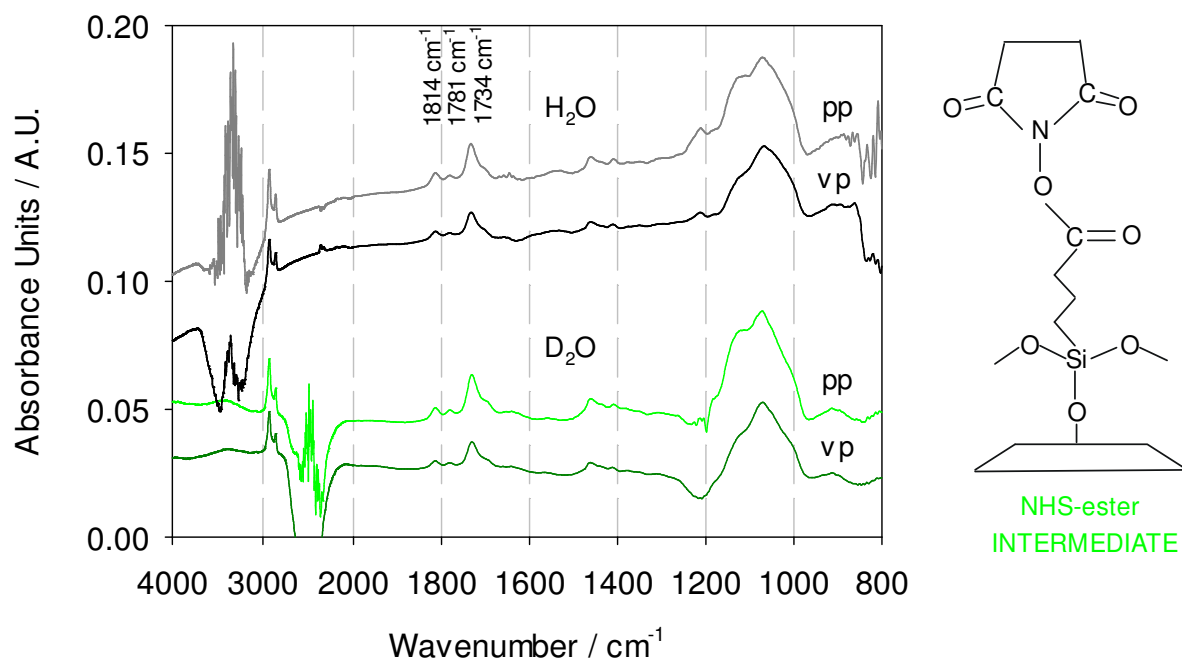


Figure 37. The SBSR FTIR spectra of NHS-ester terminated silane layer thickness of 3.9 nm in H<sub>2</sub>O (top) and D<sub>2</sub>O (bottom) in the S cuvettes, corresponding solvents (H<sub>2</sub>O and D<sub>2</sub>O) in the R cuvettes. NHS-ester vibrations such as  $\nu(\text{C}=\text{O})$  stretching and  $\nu(\text{C}=\text{O})$  succinimidyl symmetric and asymmetric stretchings are placed at 1814, 1781 and 1734  $\text{cm}^{-1}$ , respectively. Ge MIRE; T=25°C; Angle of incidence  $\theta=45^\circ$ ; Number of active internal reflections N=27.97.

Table 6. Magnitudes and uncertainties of input parameters for  $\nu_{\text{as}}(\text{COO}^-)$ . Integrated molar absorption coefficient of  $\nu_{\text{as}}(\text{COO}^-)$  overtaken from ref. [114].

Parameter, Symbol	Magnitude
Angle of incidence, $\theta/\text{deg}$	$45.0 \pm 1.5$
Refractive index of germanium MIRE, $n_1$	$4.0 \pm 0.0$
Refractive index of an adsorbed/bound layer, $n_2$	$1.45 \pm 0.05$
Refractive index of bulk (D <sub>2</sub> O), $n_3$	$1.31 \pm 0.05$
Integrated molar absorption coefficient of $\nu_{\text{as}}(\text{COO}^-)$ , $\int \epsilon(\tilde{\nu}) d\tilde{\nu} / 10^7\text{ cm/mol}$	$6.10 \pm 0.10$
Integrated absorbance, $\int A_{\text{pp/vp}}(\tilde{\nu}) d\tilde{\nu} / \text{cm}^{-1}$	$0.014 \pm 0.001$
Integration range $1589 \pm 1 - 1521 \pm 1\text{ cm}^{-1}$	$0.008 \pm 0.001$
Number of equal functional groups per molecule, $\nu$	$1 \pm 0$
Number of active internal reflections, N	$27.97 \pm 1$

#### 4.4 AMIDE BOND FORMATION

The SBSR pp- and vp-spectra of 0.1 M glucosamine hydrochloride dissolved in ultra-pure deionized water at pH=4.05 are shown in Figure 38. Spectra are divided by 20 corresponding to 5 mM glucosamine solution which will be used later. Vibrations at 1630 and 1537  $\text{cm}^{-1}$  are assigned to asymmetric  $\delta_{\text{as}}(\text{NH}_3^+)$  and symmetric  $\delta_{\text{s}}(\text{NH}_3^+)$  bending vibrations, where the intensity of the first one is overlapped by  $\delta(\text{OH})$  vibrations of glucosamine molecule as well as disturbed by water incompensation. The very weak band at 2065  $\text{cm}^{-1}$  representing the combination of symmetric  $\delta_{\text{s}}(\text{NH}_3^+)$  bending and  $\delta(\text{CCN})$  bending is typical for the existence of the  $-\text{NH}_3^+$  groups [115]. Spectral region between 1484-1300  $\text{cm}^{-1}$  consists of  $\text{CH}_2$  bending,  $\text{CH}_2$  scissoring, C-H and C-O-H deformation, C-O-H bending, and  $\text{CH}_2$  twisting vibrations. The band at 1098  $\text{cm}^{-1}$  is attributed to the C-O-H bending mode. The most intense peak placed at 1046  $\text{cm}^{-1}$  is related to  $\nu(\text{C-O})$  stretch of glucose ring. [116] The region between 3000-2800  $\text{cm}^{-1}$  consists of asymmetric  $\nu_{\text{as}}(\text{CH}_2)$  and symmetric  $\nu_{\text{s}}(\text{CH}_2)$  stretching modes.

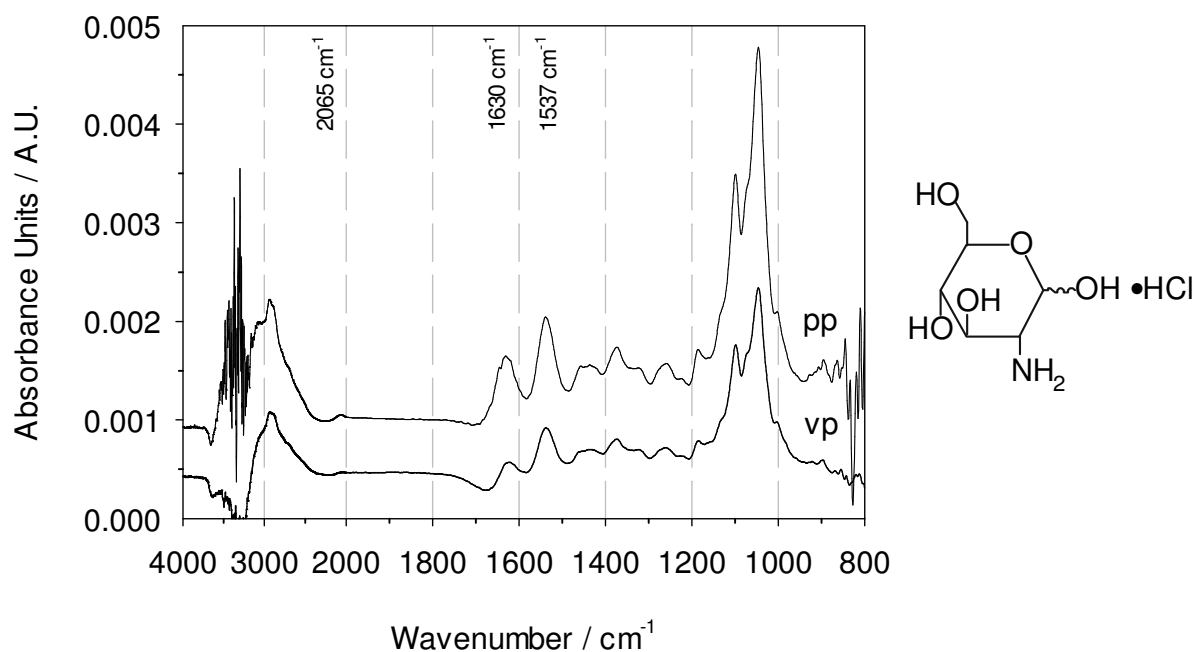


Figure 38. The SBSR FTIR pp- and vp-polarised spectra of 0.1 M glucosamine hydrochloride dissolved in ultra-pure water at pH=4.05 and measured above a clean Ge MIRE in the S channels, water in the R channels. Spectra are divided by 20 corresponding to 5 mM glucosamine solution. T=25°C; Angle of incidence  $\theta=45^\circ$ ; Number of active internal reflections N=25.33.

#### 4.4.1 Glucosamine hydrochloride binding to a silane layer via amide bonds

Coupling procedure of glucosamine hydrochloride to NHS-ester terminated silane layer is already described in Section 3.3.6. The SBSR spectra representing glucosamine effect on the NHS-ester activated silane surface were measured in both H<sub>2</sub>O and D<sub>2</sub>O environment (Figure 39). NHS-ester groups were partially removed from the silane surface due to the coupling reaction of glucose amino-groups to the carboxylic groups of the silane layer that is confirmed by negative NHS-ester vibrations between 1840-1700cm<sup>-1</sup>. In the regions of strong H<sub>2</sub>O and D<sub>2</sub>O absorption ( $\nu(\text{H}_2\text{O}) \approx 3400 \text{ cm}^{-1}$ ,  $\delta(\text{H}_2\text{O}) \approx 1640 \text{ cm}^{-1}$ ,  $\nu(\text{D}_2\text{O}) \approx 2500 \text{ cm}^{-1}$ ,  $\delta(\text{D}_2\text{O}) \approx 1200 \text{ cm}^{-1}$ ) there is a solvent overcompensation resulting from the solvent displacement by bound glucose. Spectra in H<sub>2</sub>O feature amide II vibration (  $\approx 60\%$  NH-bending) shifted from 1537 to 1547 cm<sup>-1</sup> comparing to amino-groups of free glucosamine molecule while amide I band (  $\approx 80\%$  C=O stretching) at 1646 cm<sup>-1</sup> is overlapped by  $\delta(\text{OH})$  due to the water overcompensation. Because of both NHS-ester short time stability during the solvent flow and its reactivity with glucosamine, we suppose that amide II is overlapped with released carboxylate asymmetric stretching vibration,  $\nu_{\text{as}}(\text{COO}^-)$ , at 1547 cm<sup>-1</sup> while carboxylate symmetric stretching vibration,  $\nu_{\text{s}}(\text{COO}^-)$ , is hidden by  $\delta(\text{CH})$  at 1400 cm<sup>-1</sup>.

Therefore, amide analysis is more relevant in D<sub>2</sub>O environment.

Water exchange by D<sub>2</sub>O was complete since there were no  $\nu(\text{OH})$  vibrations at 3400 cm<sup>-1</sup>. As a consequence, vibration at 1631 cm<sup>-1</sup> is undisturbed by the solvent and reflects amide I'  $\nu(\text{C=O})$  vibration of the bound glucose. The amide II' band consisting mostly of the  $\delta(\text{N-D})$  bending vibration is shifted to 1464 cm<sup>-1</sup> and overlapped with  $\nu_{\text{s}}(\text{COO}^-)$ . Since a certain amount of NHS-esters was probably decomposed without binding to glucosamine, the vibration between amide I' and amide II' placed at 1555 cm<sup>-1</sup> we could assign to released  $\nu_{\text{as}}(\text{COO}^-)$ .

The relevant parameters used for quantitative analysis of amide I' and carboxylate  $\nu_{\text{as}}(\text{COO}^-)$  bands in D<sub>2</sub>O are summarized in Table 7. The surface concentration of produced amide I' bonds was found to be  $\Gamma_{\text{exp}} = (1.01 \pm 0.15) \times 10^{-10} \text{ mol/cm}^2$  and of released silane layer carboxylate groups  $\Gamma_{\text{exp}} = (0.31 \pm 0.03) \times 10^{-10} \text{ mol/cm}^2$ . Comparing to the free carboxylate groups produced in the oxidation step,  $\Gamma_{\text{exp}} = (2.43 \pm 0.40) \times 10^{-10}$

mol/cm<sup>2</sup>, approx. 13 % of these groups was released in reaction with glucosamine while ~ 87 % remained still bound to both NHS and glucose.

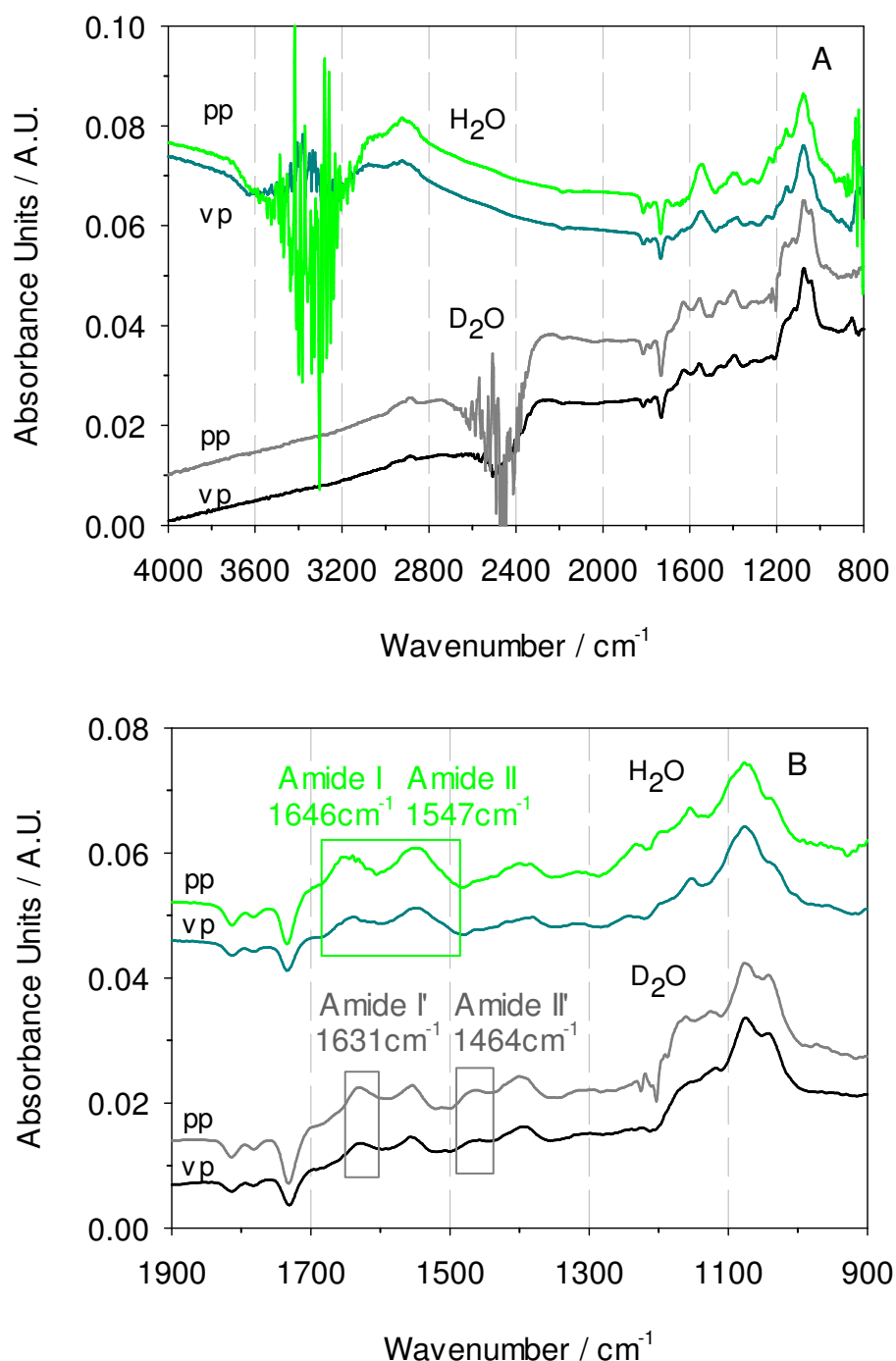


Figure 39. The SBSR FTIR pp- and vp-polarised spectra of glucosamine effect on NHS-ester terminated silane layer in H<sub>2</sub>O and D<sub>2</sub>O in the S channels, corresponding solvents (H<sub>2</sub>O and D<sub>2</sub>O) in the R channels. Decomposition of NHS-esters occurred in the region between 1840-1700 cm<sup>-1</sup>. Amide II vibration,  $\delta(\text{NH})$ , is placed at 1547 cm<sup>-1</sup> while amide I band,  $\nu(\text{C}=\text{O})$ , at 1646 cm<sup>-1</sup> is overlapped by  $\delta(\text{OH})$  in H<sub>2</sub>O environment. Amide I' and amide II'  $\delta(\text{ND})$  vibrations are placed at 1631 and 1464 cm<sup>-1</sup> in D<sub>2</sub>O, respectively. A. Full

spectral range; B. Expanded spectral range between 1900 and 900 $\text{cm}^{-1}$ . Ge MIRE; T=25°C; Angle of incidence  $\theta=45^\circ$ ; Number of active internal reflections N=27.97.

Table 7. Magnitudes and uncertainties of input parameters for amide I' and  $\nu_{\text{as}}(\text{COO}^-)$  vibrations in  $\text{D}_2\text{O}$  produced in the reaction with glucosamine hydrochloride. Integrated molar absorption coefficient of  $\nu_{\text{as}}(\text{COO}^-)$  as a rough approximation obtained from sodium polyglutamate and sodium acetate as well as the wavelength-dependent refractive indices of liquid  $\text{D}_2\text{O}$  approximated from those of liquid  $\text{H}_2\text{O}$  are overtaken from ref. [114]. Integrated molar absorption coefficient of amide I' was experimentally determined (see Appendix 6.5).

<i>Parameter, Symbol</i>	<i>Magnitude</i>
Angle of incidence, $\theta/\text{deg}$	$45.0 \pm 1.5$
Refractive index of germanium MIRE, $n_1$	$4.0 \pm 0.0$
Refractive index of an adsorbed/bound layer, $n_2$	$1.45 \pm 0.05$
Refractive index of bulk ( $\text{D}_2\text{O}$ ) at $1631\text{cm}^{-1}$ , $n_3$	$1.32 \pm 0.05$
Refractive index of bulk ( $\text{D}_2\text{O}$ ) at $1555\text{cm}^{-1}$ , $n_3$	$1.31 \pm 0.05$
Integrated molar absorption coefficient of amide I' ( $\text{C}=\text{O}$ ), $\int \epsilon(\tilde{\nu}) d\tilde{\nu} / 10^7 \text{ cm/mol}$	$1.57 \pm 0.17$
Integrated molar absorption coefficient of $\nu_{\text{as}}(\text{COO}^-)$ , $\int \epsilon(\tilde{\nu}) d\tilde{\nu} / 10^7 \text{ cm/mol}$	$6.10 \pm 0.10$
Integrated absorbance of amide I' ( $\text{C}=\text{O}$ ), $\int A_{\text{pp/vp}}(\tilde{\nu}) d\tilde{\nu} / \text{cm}^{-1}$	$0.086 \pm 0.004$
Integration range $1655 \pm 1 - 1592 \pm 1 \text{ cm}^{-1}$	$0.049 \pm 0.002$
Integrated absorbance of $\nu_{\text{as}}(\text{COO}^-)$ , $\int A_{\text{pp/vp}}(\tilde{\nu}) d\tilde{\nu} / \text{cm}^{-1}$	$0.092 \pm 0.005$
Integration range $1589 \pm 1 - 1521 \pm 1 \text{ cm}^{-1}$	$0.067 \pm 0.003$
Number of equal functional groups per molecule, $\nu$	$1 \pm 0$
Number of active internal reflections, N	$27.97 \pm 1$

The final SBSR FTIR spectra of glucose coated silane layer in  $\text{H}_2\text{O}$  and  $\text{D}_2\text{O}$  are shown in Figure 40. Besides amide bonds, spectra feature the  $\nu(\text{C}=\text{O})$  vibration at  $1703 \text{ cm}^{-1}$  resulting probably from the unreacted protonated  $\text{COOH}$  groups of the silane layer. Due to NHS-ester non-stability during the solvent flow the surface concentration of released carboxylate  $\nu_{\text{as}}(\text{COO}^-)$  groups was calculated again and it was found to be  $\Gamma_{\text{exp}} = (0.35 \pm 0.04) \times 10^{-10} \text{ mol/cm}^2$  that is approx. 14 % of the free carboxylate groups produced in the oxidation step. Slightly increased concentration suggests that NHS-ester decomposition has continued in  $\text{H}_2\text{O}$  and  $\text{D}_2\text{O}$ . Relevant parameters used for quantification of the overall released  $\nu_{\text{as}}(\text{COO}^-)$  groups in reaction with glucosamine are summarized in Table 8.



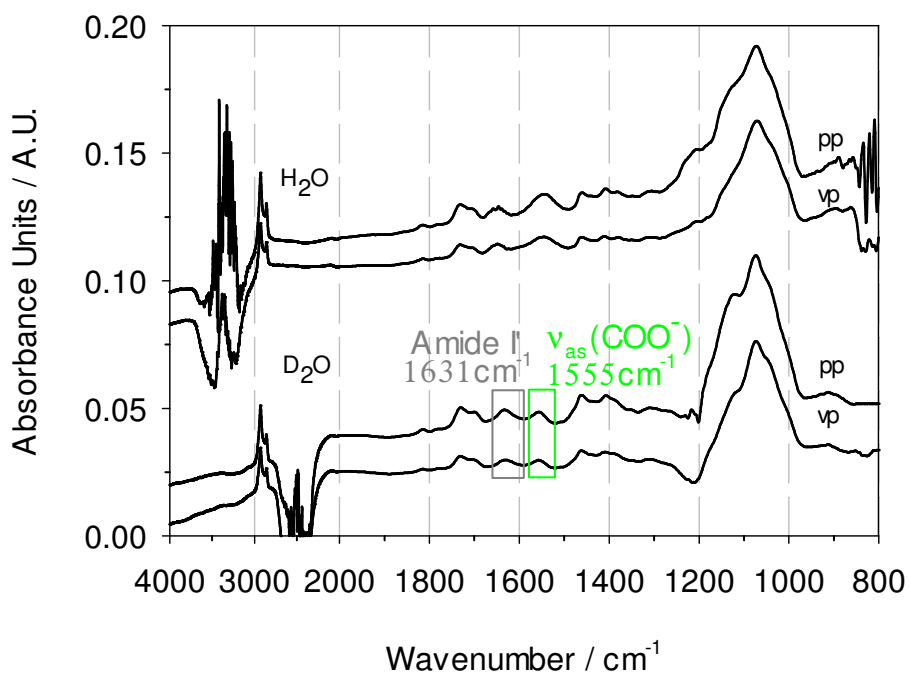


Figure 40. The SBSR FTIR pp- and vp-spectra of glucose coated silane layer in H<sub>2</sub>O and D<sub>2</sub>O separately in the S channels, corresponding solvents (H<sub>2</sub>O and D<sub>2</sub>O) in the R channels. Ge MIRE; T=25°C; Angle of incidence  $\theta=45^\circ$ ; Number of active internal reflections  $N=27.97$ .

Table 8. Magnitudes and uncertainties of input parameters for the overall released  $\nu_{as}(\text{COO}^-)$  groups after glucose binding to the silane layer. Integrated molar absorption coefficient of  $\nu_{as}(\text{COO}^-)$  vibration overtaken from ref. [114].

Parameter, Symbol	Magnitude
Angle of incidence, $\theta/\text{deg}$	$45.0 \pm 1.5$
Refractive index of germanium MIRE, $n_1$	$4.0 \pm 0.0$
Refractive index of an adsorbed/bound layer, $n_2$	$1.45 \pm 0.05$
Refractive index of D <sub>2</sub> O, $n_3$	$1.31 \pm 0.05$
Integrated molar absorption coefficient of $\nu_{as}(\text{COO}^-)$ , $\int \epsilon(\tilde{\nu}) d\tilde{\nu} / 10^7 \text{ cm/mol}$	$6.10 \pm 0.10$
Integrated absorbencies, $\int A_{pp/vp}(\tilde{\nu}) d\tilde{\nu} / \text{cm}^{-1}$	$0.106 \pm 0.005$
Integration range $1589 \pm 1 - 1521 \pm 1 \text{ cm}^{-1}$	$0.075 \pm 0.004$
Number of equal functional groups per molecule, $\nu$	$1 \pm 0$
Number of active internal reflections, $N$	$27.97 \pm 1$

#### 4.4.2 Deactivation of remained NHS-ester groups of the silane layer by ethanolamine

The residual NHS-ester groups were deactivated by treatment with 1 M ethanolamine (pH=8.5-9.0). The removing of NHS-ester was followed by a new amide bond formation indicating ethanolamine binding. During this step remnants of sulphate and succinimide were washed out that is confirmed by the negative bands in 1130-960  $\text{cm}^{-1}$  region. The effect of ethanolamine on glucose coated silane layer in  $\text{H}_2\text{O}$  and  $\text{D}_2\text{O}$  environment is shown in Figure 41 where the SBSR spectrum of glucose coated silane layer and the SBSR spectrum of ethanolamine treated glucose coated silane layer are taken as reference and sample, respectively. Amide II and amide I vibrations at 1557 and 1643  $\text{cm}^{-1}$  dominate in  $\text{H}_2\text{O}$  spectra while the spectra measured in  $\text{D}_2\text{O}$  are characterised by amide II' and amide I' vibrations at 1475 and 1631  $\text{cm}^{-1}$ , respectively. Because of both NHS-ester non-stability during the solvent flow and its reactivity with ethanolamine, we suppose that amide II is overlapped with released carboxylate asymmetric  $\nu_{\text{as}}(\text{COO}^-)$  vibration at 1555  $\text{cm}^{-1}$  while carboxylate symmetric  $\nu_{\text{s}}(\text{COO}^-)$  vibration is visible as a small peak at  $\sim 1400 \text{ cm}^{-1}$  in  $\text{H}_2\text{O}$  spectra. Water exchange by  $\text{D}_2\text{O}$  was complete since there were no  $\nu(\text{OH})$  vibrations at  $3400 \text{ cm}^{-1}$  and vibration at 1631  $\text{cm}^{-1}$  originates only from amide I'  $\nu(\text{C=O})$  bond.

Quantitative analysis related to  $\nu_{\text{as}}(\text{COO}^-)$  and amide I' was performed using the spectra measured in  $\text{D}_2\text{O}$  environment. The surface concentration of produced amide I' bonds by ethanolamine was found to be  $\Gamma_{\text{exp}} = (1.02 \pm 0.15) \times 10^{-10} \text{ mol/cm}^2$  indicating approximately the same amount of formed amide I' bonds as with glucosamine. The surface concentration of  $\nu_{\text{as}}(\text{COO}^-)$  that became released from NHS in reaction with ethanolamine was found to be  $\Gamma_{\text{exp}} = (0.09 \pm 0.01) \times 10^{-10} \text{ mol/cm}^2$  that is approx. 4 % of overall amount of carboxylate vibrations produced by ozone. The relevant parameters used for quantitative analysis are summarized in Table 9.

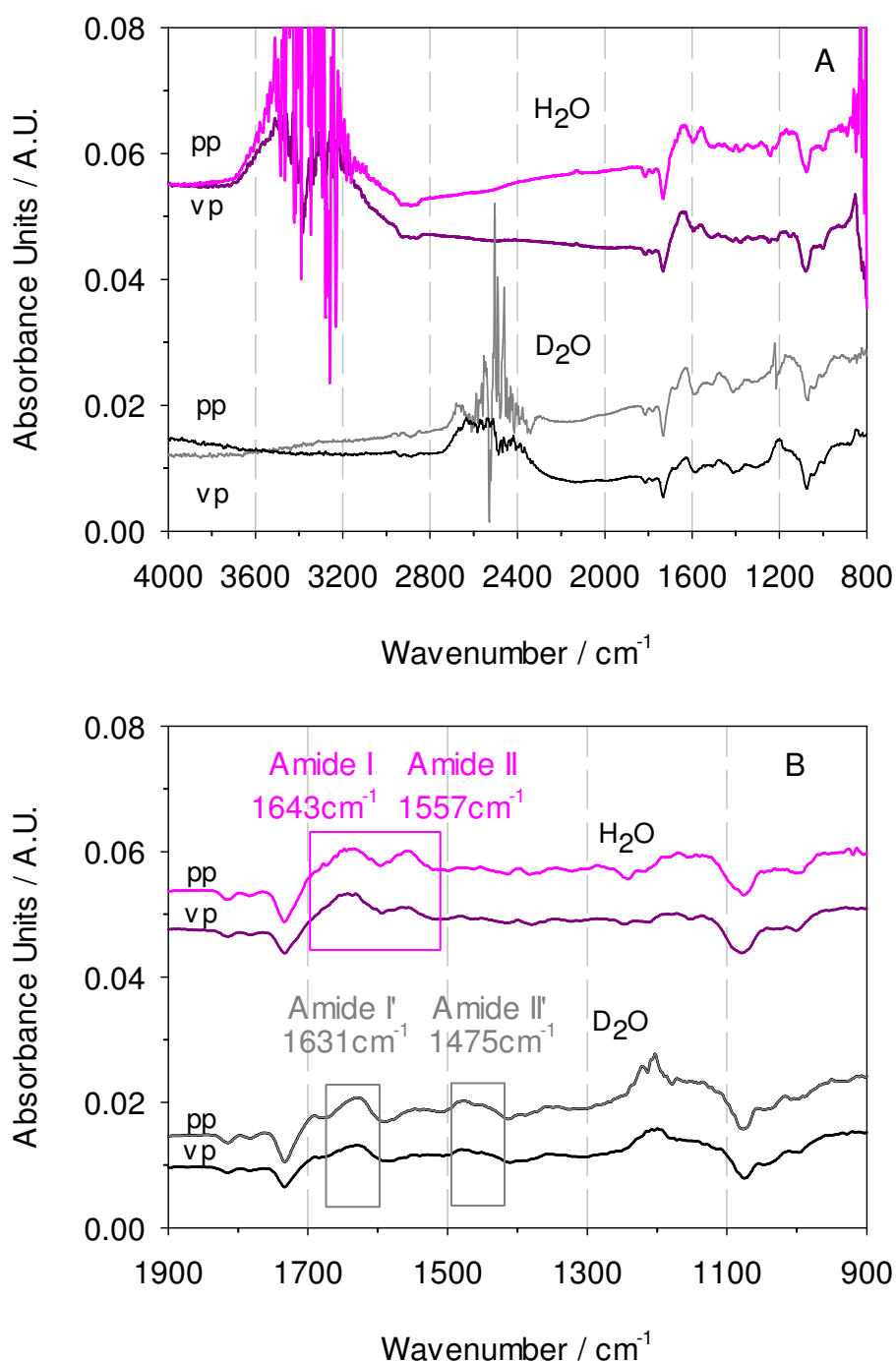


Figure 41. Ethanolamine effect on glucose coated silane layer presented as a difference between the SBSR spectra of glucose coated silane layer (reference) and ethanolamine treated glucose coated silane layer (sample). Further decomposition of NHS-esters occurred in the NHS-ester region between 1840-1700  $\text{cm}^{-1}$ . Spectra measured in  $\text{H}_2\text{O}$  are characterized by amide I and amide II vibrations at 1643 and 1557  $\text{cm}^{-1}$ , respectively, while in  $\text{D}_2\text{O}$  these vibrations are separated by  $\nu_{\text{as}}(\text{COO}^-)$  vibration at 1555  $\text{cm}^{-1}$  which was released from NHS by ethanolamine reaction. Ge MIRE;  $T=25^\circ\text{C}$ ; Angle of incidence  $\theta=45^\circ$ ; Number of active internal reflections  $N=27.97$ .

Table 9. Magnitudes and uncertainties of input parameters for produced amide I' and released  $\nu_{\text{as}}(\text{COO}^-)$  vibrations in the reaction with ethanolamine. Integrated molar absorption coefficient of  $\nu_{\text{as}}(\text{COO}^-)$  vibration is overtaken from ref. [114] while for amide I' it was experimentally determined (see Appendix 6.5).

<i>Parameter, Symbol</i>	<i>Magnitude</i>
Angle of incidence, $\theta/\text{deg}$	$45.0 \pm 1.5$
Refractive index of germanium MIRE, $n_1$	$4.0 \pm 0.0$
Refractive index of an adsorbed/bound layer, $n_2$	$1.45 \pm 0.05$
Refractive index of bulk ( $\text{D}_2\text{O}$ ) at $1631\text{cm}^{-1}$ , $n_3$	$1.32 \pm 0.05$
Refractive index of bulk ( $\text{D}_2\text{O}$ ) at $1555\text{cm}^{-1}$ , $n_3$	$1.31 \pm 0.05$
Integrated molar absorption coefficient of amide I' ( $\text{C=O}$ ), $\int \epsilon(\tilde{\nu}) d\tilde{\nu} / 10^7 \text{ cm/mol}$	$1.57 \pm 0.17$
Integrated molar absorption coefficient of $\nu_{\text{as}}(\text{COO}^-)$ , $\int \epsilon(\tilde{\nu}) d\tilde{\nu} / 10^7 \text{ cm/mol}$	$6.10 \pm 0.10$
Integrated absorbance of amide I' ( $\text{C=O}$ ), $\int A_{\text{pp/vp}}(\tilde{\nu}) d\tilde{\nu} / \text{cm}^{-1}$	$0.086 \pm 0.004$
Integration range $1655 \pm 1 - 1592 \pm 1 \text{ cm}^{-1}$	$0.050 \pm 0.003$
Integrated absorbance of $\nu_{\text{as}}(\text{COO}^-)$ , $\int A_{\text{pp/vp}}(\tilde{\nu}) d\tilde{\nu} / \text{cm}^{-1}$	$0.029 \pm 0.001$
Integration range $1573 \pm 1 - 1508 \pm 1 \text{ cm}^{-1}$	$0.017 \pm 0.001$
Number of equal functional groups per molecule, $\nu$	$1 \pm 0$
Number of active internal reflections, $N$	$27.97 \pm 1$

#### 4.4.3 Overall amount of formed amide bonds

At the end, irreversibly adsorbed glucose molecules were cleaned by washing with sodium dodecyl sulphate solution (10 mg/ml SDS in PBS). The SBSR spectra of the final state of glucose and ethanol terminated silane layer in  $\text{H}_2\text{O}$  and  $\text{D}_2\text{O}$  environment are shown in Figure 42.

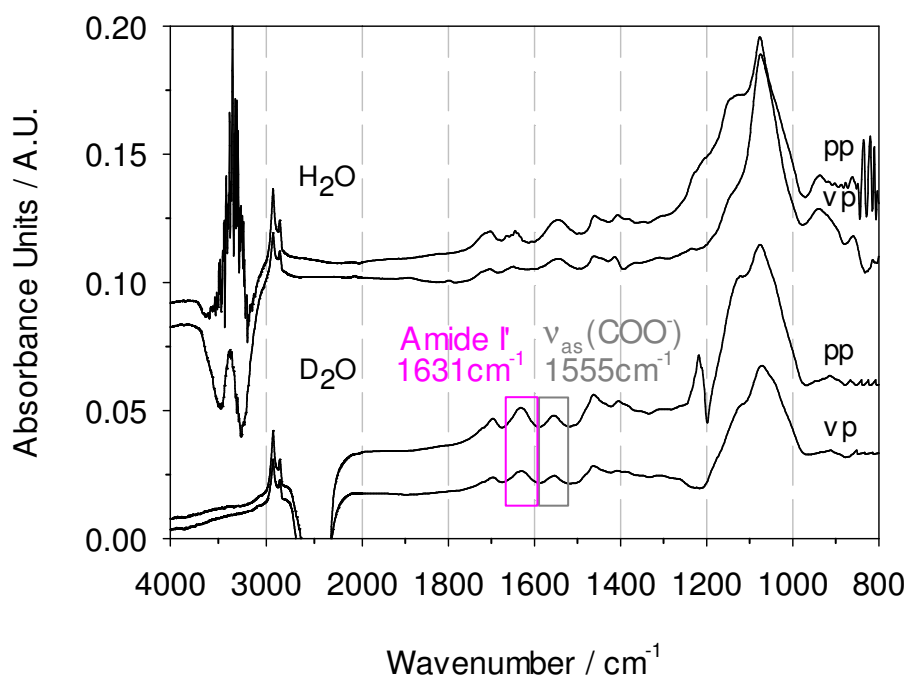


Figure 42. The SBSR FTIR pp- and vp-spectra of both glucose and ethanol coated silane layer in H<sub>2</sub>O and D<sub>2</sub>O environment in the S channels, corresponding solvents (H<sub>2</sub>O and D<sub>2</sub>O) in the R channels. Ge MIRE; T=25°C; Angle of incidence  $\theta=45^\circ$ ; Number of active internal reflections N=27.97.

At the end of the experiment, the overall surface concentration of amide I' bonds produced by both glucosamine and ethanolamine was found to be  $\Gamma_{\text{exp}}=(2.23\pm0.32)\times10^{-10}$  mol/cm<sup>2</sup> (the relevant parameters are summarized in Table 10). This concentration is slightly increased comparing to the sum of the amide I' surface concentrations produced separately by glucosamine and ethanolamine,  $\Gamma_{\text{exp}}=2.03\times10^{-10}$  mol/cm<sup>2</sup>, due to a small D<sub>2</sub>O contamination by H<sub>2</sub>O and therefore amide I' disturbances by  $\delta(\text{OH})$  vibrations.

By comparing the amount of COOH groups produced by ozone,  $\Gamma_{\text{exp}}=2.43\times10^{-10}$  mol/cm<sup>2</sup>, and overall sum of produced amide I' bonds,  $\Gamma_{\text{exp}}=2.03\times10^{-10}$  mol/cm<sup>2</sup>, we could conclude that ~ 84% of COOH groups was used for amide bond formation with glucosamine (~ 42%) and ethanolamine (~ 42 %) while ~ 16% of COOH groups remained free. This finding is in agreement with the overall calculated surface concentrations of carboxylate groups not reacted with glucosamine and ethanolamine (Table 10) that was found to be  $\Gamma_{\text{exp}}=(0.41\pm0.10)\times10^{-10}$  mol/cm<sup>2</sup> representing ~ 17% of the overall COO<sup>-</sup> groups.

Table 10. Magnitudes and uncertainties of input parameters for overall amide I' and  $\nu_{\text{as}}(\text{COO}^-)$  vibrations produced by both glucosamine and ethanolamine. Integrated molar absorption coefficient of  $\nu_{\text{as}}(\text{COO}^-)$  vibration is overtaken from ref. [114] while for amide I' it was experimentally determined (see Appendix 6.5).

<i>Parameter, Symbol</i>	<i>Magnitude</i>
Angle of incidence, $\theta/\text{deg}$	$45.0 \pm 1.5$
Refractive index of germanium MIRE, $n_1$	$4.0 \pm 0.0$
Refractive index of an adsorbed/bound layer, $n_2$	$1.45 \pm 0.05$
Refractive index of bulk ( $\text{D}_2\text{O}$ ) at $1631\text{cm}^{-1}$ , $n_3$	$1.32 \pm 0.05$
Refractive index of bulk ( $\text{D}_2\text{O}$ ) at $1555\text{cm}^{-1}$ , $n_3$	$1.31 \pm 0.05$
Integrated molar absorption coefficient of amide I' ( $\text{C}=\text{O}$ ), $\int \epsilon(\tilde{\nu}) d\tilde{\nu} / 10^7 \text{ cm/mol}$	$1.57 \pm 0.17$
Integrated molar absorption coefficient of $\nu_{\text{as}}(\text{COO}^-)$ , $\int \epsilon(\tilde{\nu}) d\tilde{\nu} / 10^7 \text{ cm/mol}$	$6.10 \pm 0.10$
Integrated absorbance of amide I' ( $\text{C}=\text{O}$ ), $\int A_{\text{pp/vp}}(\tilde{\nu}) d\tilde{\nu} / \text{cm}^{-1}$	$0.186 \pm 0.009$
Integration range $1655 \pm 1 - 1592 \pm 1 \text{ cm}^{-1}$	$0.114 \pm 0.006$
Integrated absorbance of $\nu_{\text{as}}(\text{COO}^-)$ , $\int A_{\text{pp/vp}}(\tilde{\nu}) d\tilde{\nu} / \text{cm}^{-1}$	$0.131 \pm 0.006$
Integration range $1589 \pm 1 - 1521 \pm 1 \text{ cm}^{-1}$	$0.082 \pm 0.004$
Number of equal functional groups per molecule, $\nu$	$1 \pm 0$
Number of active internal reflections, $N$	$27.97 \pm 1$

#### 4.5 Bovin Serum Albumin (BSA) ADSORPTION on glucose covered silane layer

The effectiveness of glucose covered silane layer towards non-specific protein Bovine Serum Albumin (BSA) adsorption was investigated. The protein solution (10 mg BSA/10 ml PBS) was passed above a clean Ge MIRE as well as over the glucose modified silane surface. The corresponding SBSR spectra of adsorbed protein are shown in Figure 43. The most prominent vibrations of BSA are amide I  $\nu(\text{C}=\text{O})$  stretching at  $1650\text{ cm}^{-1}$  and amide II  $\delta(\text{N-H})$  bending vibration at  $1546\text{ cm}^{-1}$ . Glucose modified silane surface shows significant lower non-specific adsorption compared to the clean Ge MIRE.

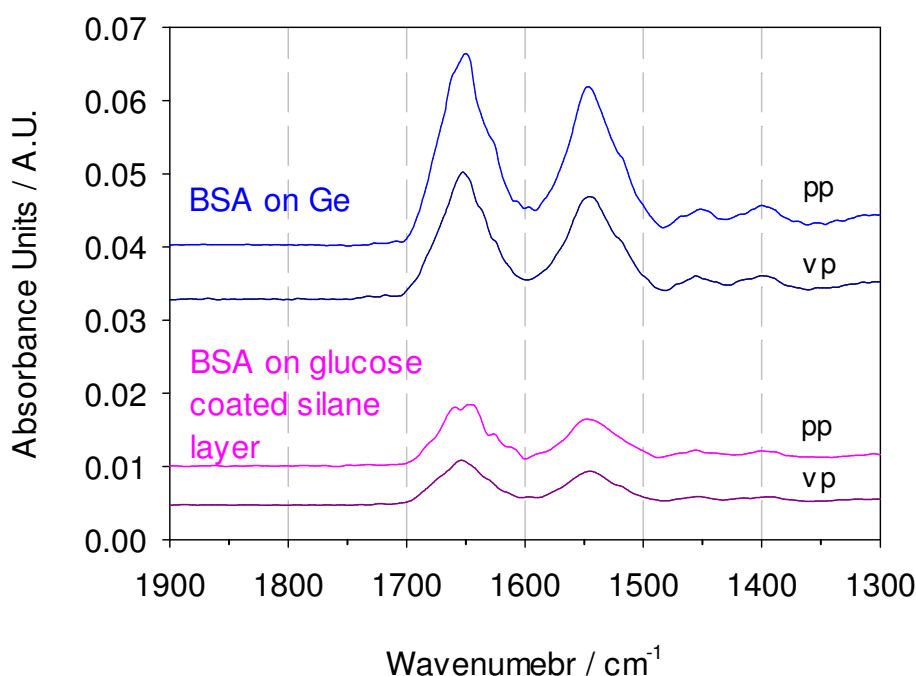


Figure 43. The SBSR FTIR pp- and vp-spectra of adsorbed BSA in  $\text{H}_2\text{O}$  on a clean Ge MIRE and on the glucose coated silane layer in the S channels, water in the R channels. Ge MIRE;  $T=25^\circ\text{C}$ ; Angle of incidence  $\theta=45^\circ$ ; Number of active internal reflections  $N=27.97$ .

The surface concentrations of amide II bonds of adsorbed BSA on the clean Ge MIRE was found to be  $\Gamma_{\text{exp}}=(3.47\pm0.65)\times10^{-12}\text{ mol/cm}^2$  while on glucose covered silane layer  $\Gamma_{\text{exp}}=(1.02\pm0.19)\times10^{-12}\text{ mol/cm}^2$ . Comparison of these surface concentrations shows that glucose has reduced adsorption of BSA approx. 70 % in comparison to the clean Ge plate. The relevant parameters used for quantitative analysis are summarized in Table 11.

Table 11. Magnitudes and uncertainties of input parameters for amide II vibration of protein BSA. Integrated molar absorption coefficient of amide II is overtaken from ref. [114].

<i>Parameter, Symbol</i>	<i>Magnitude</i>
Angle of incidence, $\theta/\text{deg}$	$45.0 \pm 1.5$
Refractive index of germanium MIRE, $n_1$	$4.0 \pm 0.0$
Refractive index of an adsorbed/bound layer, $n_2$	$1.45 \pm 0.05$
Refractive index of bulk ( $\text{D}_2\text{O}$ ) at $1555\text{cm}^{-1}$ , $n_3$	$1.31 \pm 0.05$
Integrated molar absorption coefficient of BSA amide II, $\int \varepsilon(\tilde{\nu}) d\tilde{\nu} / 10^6 \text{ cm/mol}$	$8.25 \pm 1.24$
Integrated absorbance of BSA amide II band on Ge MIRE, $\int A_{\text{pp/vp}}(\tilde{\nu}) d\tilde{\nu} / \text{cm}^{-1}$	$0.846 \pm 0.042$
Integration range $1592 \pm 1 - 1484 \pm 1 \text{ cm}^{-1}$	$0.575 \pm 0.029$
Integrated absorbance of BSA amide II on the silane layer, $\int A_{\text{pp/vp}}(\tilde{\nu}) d\tilde{\nu} / \text{cm}^{-1}$	$0.244 \pm 0.012$
Integration range $1592 \pm 1 - 1484 \pm 1 \text{ cm}^{-1}$	$0.176 \pm 0.009$
Number of equal functional groups per molecule, $\nu$	$582 \pm 0$
Number of active internal reflections, $N$	$27.97 \pm 1$

For the estimation of upper and lower boundaries for the average area per BSA molecule after its adsorption on the Ge MIRE, outer shape of BSA molecule is approximated as a cuboid with a base area of  $40\text{\AA} \times 40\text{\AA} = 1600\text{\AA}^2$  and a height of  $140\text{\AA}$  [117]. Two boundary states can be considered. (1) The molecules adsorb with the lateral surface which results in  $40\text{\AA} \times 140\text{\AA} = 5600\text{\AA}$  per molecule corresponding to a surface concentration of  $\Gamma_{\text{min}} \approx 3.0 \times 10^{-10} \text{ mol/cm}^2$ . (2) The molecules adsorb with the base plane and occupy an area of about  $1600\text{\AA}^2$  per molecule corresponding to a surface concentration of  $\Gamma_{\text{max}} \approx 10.4 \times 10^{-10} \text{ mol/cm}^2$ .

The experimentally determined surface concentration of BSA on a clean Ge MIRE indicates monolayer formation of BSA via its lateral surface. Comparing to the surface concentration of BSA on glucose coated silane layer it can be concluded that such surface significantly reduced BSA adsorption to a submonolayer level.



## 4.6 Preliminary experiments with amino-dextrans

The SBSR pp-spectrum of 0.81 g amino-dextran (Molecular Weight 5000) dissolved in 16 ml of ultra-pure H<sub>2</sub>O (corresponding to amino-groups concentration of 5 mM) at adjusted pH=7.2 is shown in Figure 44. Vibration at 1655 cm<sup>-1</sup> is assigned to  $\delta(\text{OH})$  and vibration at 1555 cm<sup>-1</sup> to  $\delta(\text{NH})$  bending mode. Spectral region between 1500-1300 cm<sup>-1</sup> consists of CH<sub>2</sub> bending, CH<sub>2</sub> scissoring, C-H and C-O-H deformation, C-O-H bending, and CH<sub>2</sub> twisting vibrations. The most intense vibrations in the region between 1200-970 cm<sup>-1</sup> correspond to glucose ring vibrations. [116] The region between 3000-2800 cm<sup>-1</sup> is related to asymmetric  $\nu_{\text{as}}(\text{CH}_2)$  and symmetric  $\nu_{\text{s}}(\text{CH}_2)$  stretching modes.

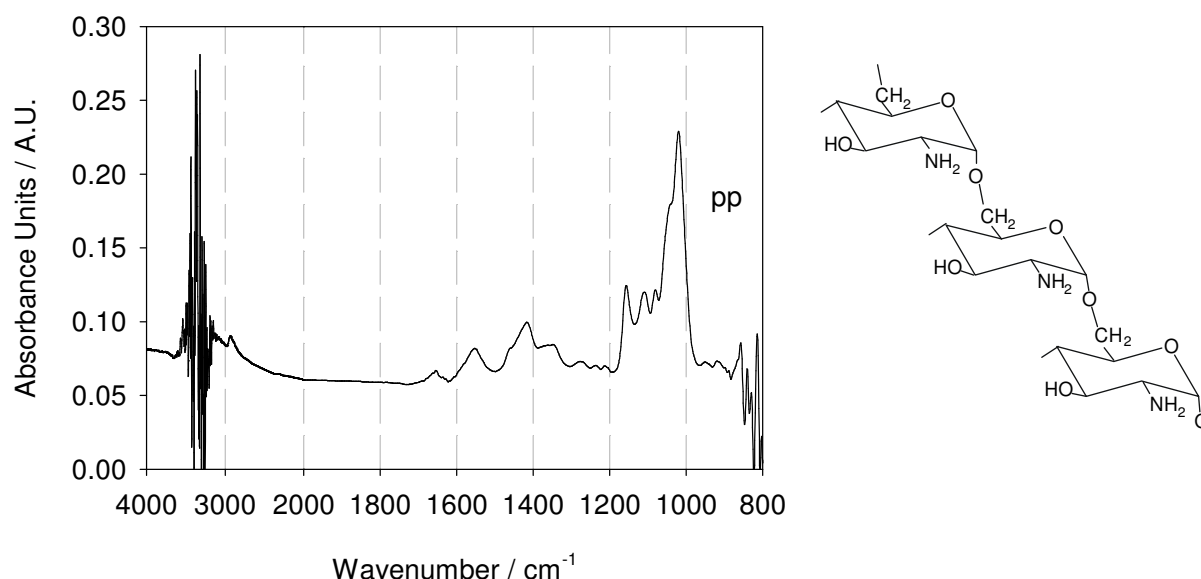


Figure 44. The SBSR FTIR pp-spectrum of 0.81 g amino-dextran dissolved in 16 ml of ultra-pure water at pH=7.2 above NHS-ester terminated silane layer. In order to subtract silane layer the SBSR FTIR pp-spectrum of NHS-ester terminated silane layer was used as a reference. Ge MIRE; T=25°C; Angle of incidence  $\theta=45^\circ$ ; Number of active internal reflections N=27.29.

### 4.6.1 Dextran binding to the silane layer via amide bonds

Coupling procedure for binding of amino-dextran to the NHS-ester terminated silane layer is already described in Section 3.3.6. The SBSR spectra of amino-dextran effect were measured in both H<sub>2</sub>O and D<sub>2</sub>O environment (Figure 45). NHS-ester groups were partially removed from the silane surface due to the coupling reaction of dextran amino-groups to carboxylic groups of the silane layer as well as to NHS-ester

decomposition during the solvent flow that is documented by negative NHS-ester vibrations in the region between 1840-1700  $\text{cm}^{-1}$  and by amide bond formation. Spectra measured in  $\text{H}_2\text{O}$  feature a very weak amide II vibration ( $\approx 60\%$  NH-bending) at 1540  $\text{cm}^{-1}$  while amide I band ( $\approx 80\%$  C=O stretching) at 1649  $\text{cm}^{-1}$  is overlapped by  $\delta(\text{OH})$  due to the water overcompensation and existing OH groups of amino-dextran.

Because of both NHS-ester non-stability during the solvent flow and its reactivity with amino-dextran we suppose that amide II is overlapped with released carboxylate asymmetric stretching vibration,  $\nu_{\text{as}}(\text{COO}^-)$ , at 1540  $\text{cm}^{-1}$ . Carboxylate symmetric stretching vibration  $\nu_{\text{s}}(\text{COO}^-)$  appears as a weak band overlapped by  $\delta(\text{CH})$  at 1400  $\text{cm}^{-1}$ .

As in the case of glucosamine, in the regions of strong  $\text{H}_2\text{O}$  and  $\text{D}_2\text{O}$  absorption ( $\nu(\text{H}_2\text{O}) \approx 3400 \text{ cm}^{-1}$ ;  $\delta(\text{H}_2\text{O}) \approx 1640 \text{ cm}^{-1}$ ;  $\nu(\text{D}_2\text{O}) \approx 2500 \text{ cm}^{-1}$ ;  $\delta(\text{D}_2\text{O}) \approx 1200 \text{ cm}^{-1}$ ) there is a solvent overcompensation resulting from the solvent displacement by bound dextran.

Water exchange by  $\text{D}_2\text{O}$  was complete since there were no  $\nu(\text{OH})$  vibrations at 3400  $\text{cm}^{-1}$ . As a consequence, the vibration at 1634  $\text{cm}^{-1}$  should be undisturbed by the solvent and reflect only amide I'. The amide II' band consisting mostly of the  $\delta(\text{ND})$  bending vibration is shifted to 1464  $\text{cm}^{-1}$  and overlapped with  $\nu_{\text{s}}(\text{COO}^-)$ . Since the regions of amide I' and  $\nu_{\text{as}}(\text{COO}^-)$  are not well resolved unabling determination of the limits for band integration, presented spectra are used only qualitatively.

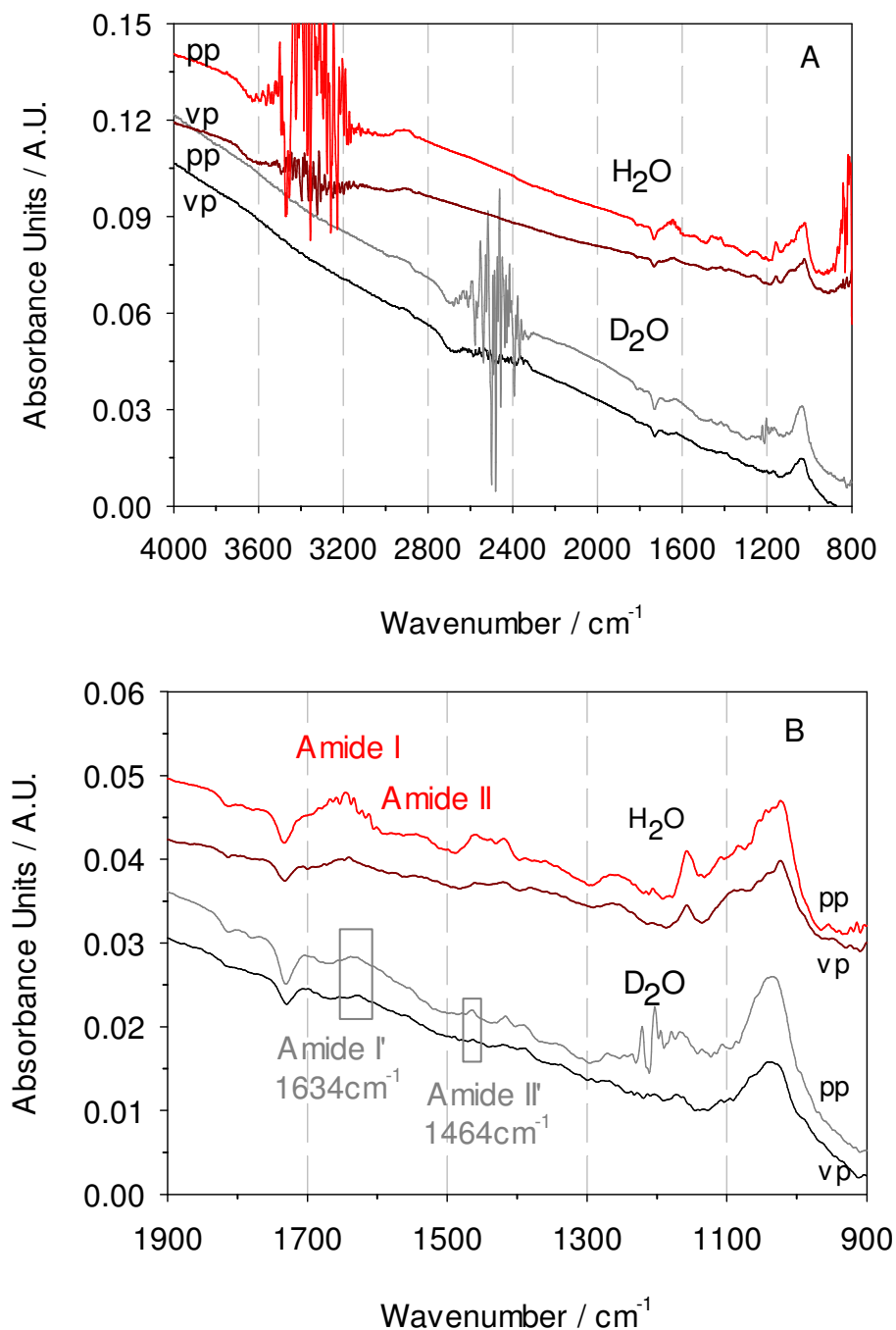


Figure 45. The SBSR FTIR pp- and vp-polarised spectra of amino-dextran effect on NHS-ester terminated silane layer in H<sub>2</sub>O and D<sub>2</sub>O in the S channels, corresponding solvents (H<sub>2</sub>O and D<sub>2</sub>O) in the R channels. Decomposition of NHS-esters occurred in the region between 1840-1700  $\text{cm}^{-1}$ . Expected amide II  $\delta(\text{N-H})$  vibration should be placed at 1540  $\text{cm}^{-1}$  while amide I  $\nu(\text{C=O})$  at 1649  $\text{cm}^{-1}$  is overlapped by  $\delta(\text{OH})$  in H<sub>2</sub>O environment. Amide I'  $\nu(\text{C=O})$  and amide II' (N-D) vibrations are expected at 1634 and 1464  $\text{cm}^{-1}$  in D<sub>2</sub>O environment. Due to unresolved amide I' and  $\nu_{\text{as}}(\text{COO}^-)$  bands, presented spectra are used only qualitatively as an evidence for amide bond formation. A. Full spectral range; B. Expanded spectral range between 1900-900  $\text{cm}^{-1}$ . Ge MIRE; T=25°C; Angle of incidence  $\theta=45^\circ$ ; Number of active internal reflections  $N=27.97$ .

The final SBSR FTIR spectra of dextran coated silane layer in H<sub>2</sub>O and D<sub>2</sub>O environment shown in Figure 46 give much better insight into amide bond formation and, therefore, they are used quantitatively. Relevant parameters used for quantification are summarized in Table 12. The surface concentration of produced amide I' groups was found to be  $\Gamma_{\text{exp}}=(0.74\pm0.11)\times10^{-10}$  mol/cm<sup>2</sup> while the surface concentration of released  $\nu_{\text{as}}(\text{COO}^-)$  groups  $\Gamma_{\text{exp}}=(0.071\pm0.10)\times10^{-10}$  mol/cm<sup>2</sup> corresponding to  $\sim 5\%$  of free  $\text{COO}^-$  groups produced by ozone ( $\Gamma_{\text{exp}}=(1.59\pm0.24)\times10^{-10}$  mol/cm<sup>2</sup>). For the quantification of  $\nu_{\text{as}}(\text{COO}^-)$  groups of the used silane layer, see Appendix 6.6.

Table 12. Magnitudes and uncertainties of input parameters for the calculation of the surface concentration of  $\nu_{\text{as}}(\text{COO}^-)$  and amide I' in D<sub>2</sub>O. Integrated molar absorption coefficient of  $\nu_{\text{as}}(\text{COO}^-)$  vibration is overtaken from ref. [114] while for amide I' it was experimentally determined (see Appendix 6.5).

<i>Parameter, Symbol</i>	<i>Magnitude</i>
Angle of incidence, $\theta/\text{deg}$	$45.0\pm1.5$
Refractive index of germanium MIRE, $n_1$	$4.0\pm0.0$
Refractive index of an adsorbed/bound layer, $n_2$	$1.45\pm0.05$
Refractive index of D <sub>2</sub> O, $n_3$	$1.31\pm0.05$
Integrated molar absorption coefficient of $\nu_{\text{as}}(\text{COO}^-)$ , $\int \epsilon(\tilde{\nu})d\tilde{\nu}/10^7$ cm/mol	$6.10\pm0.10$
Integrated absorbencies of $\nu_{\text{as}}(\text{COO}^-)$ , $\int A_{\text{pp/vp}}(\tilde{\nu})d\tilde{\nu}/\text{cm}^{-1}$	$0.027\pm0.001$
Integration range $1589\pm1$ - $1521\pm1\text{cm}^{-1}$	$0.0090\pm0.0005$
Integrated molar absorption coefficient of amide I' (C=O), $\int \epsilon(\tilde{\nu})d\tilde{\nu}/10^7$ cm/mol	$1.57\pm 0.17$
Integrated absorbance of amide I' (C=O), $\int A_{\text{pp/vp}}(\tilde{\nu})d\tilde{\nu}/\text{cm}^{-1}$	$0.059\pm0.003$
Integration range $1670\pm1$ - $1610\pm1\text{cm}^{-1}$	$0.041\pm0.002$
Number of equal functional groups per molecule, $\nu$	$1\pm0$
Number of active internal reflections, $N$	$27.97\pm1$

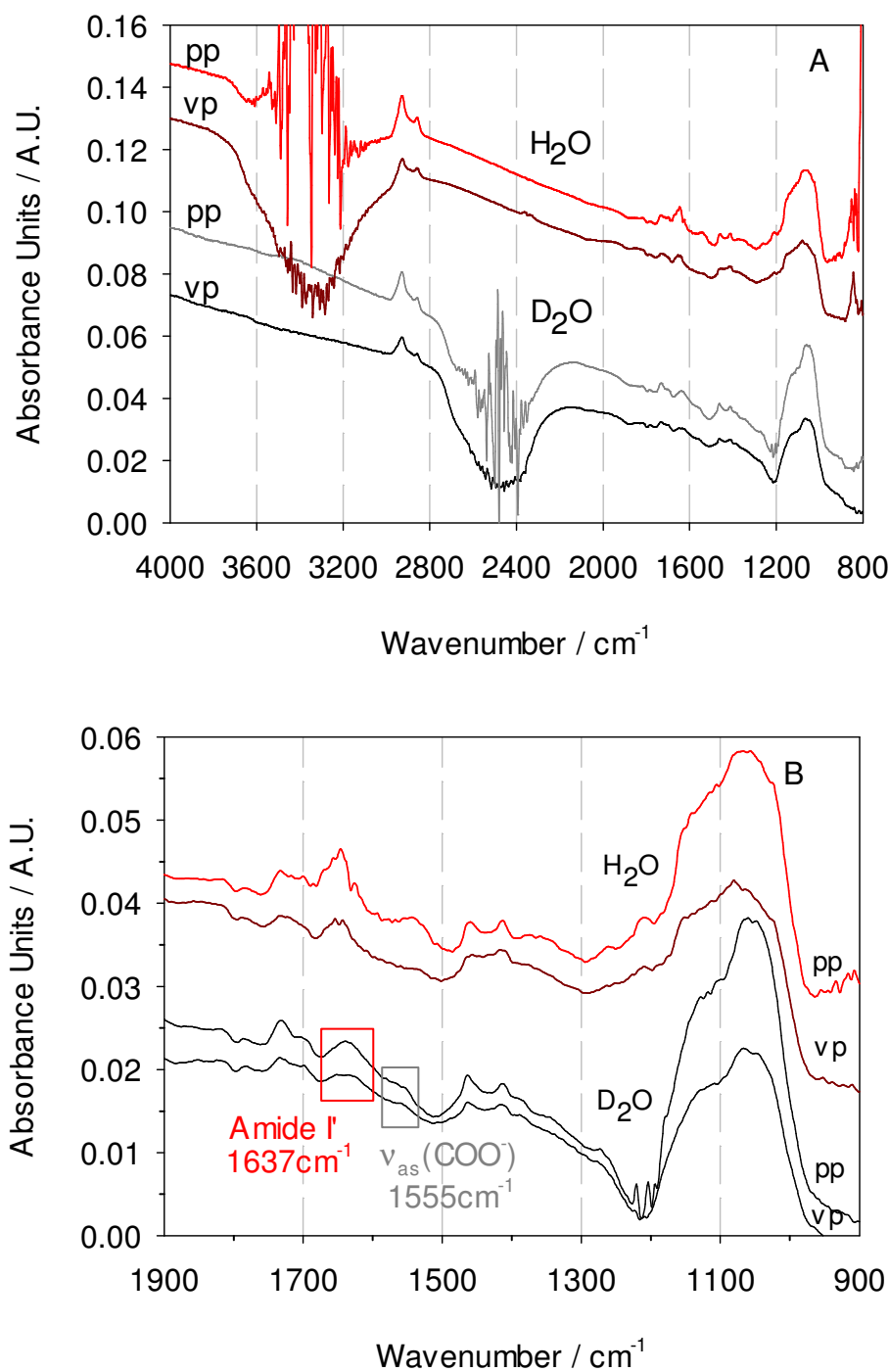


Figure 46. The SBSR FTIR pp- and vp-spectra of dextran coated silane layer in H<sub>2</sub>O and D<sub>2</sub>O in the S channels, corresponding solvent (H<sub>2</sub>O and D<sub>2</sub>O) in the R channels. Spectra measured in D<sub>2</sub>O are used for the quantitative analysis of amide I' at 1637 cm<sup>-1</sup> and still very weak ν<sub>as</sub>(COO<sup>-</sup>) vibration at 1555 cm<sup>-1</sup>. A. Full spectral range; B. Expanded spectral range between 1900-900 cm<sup>-1</sup>. Ge MIRE; T=25°C; Angle of incidence θ=45°; Number of active internal reflections N=27.97.

#### 4.6.2 Deactivation of remained NHS-ester groups of the silane layer by ethanolamine

The remained NHS-ester groups after dextran coating of the silane layer were deactivated by treatment with 1 M ethanolamine (pH=8.5-9.0). The effect of ethanolamine on dextran coated silane surface in H<sub>2</sub>O and D<sub>2</sub>O environment is shown in Figure 47 where the reference is the SBSR spectrum of dextran coated silane layer and the sample is the SBSR spectrum of ethanolamine treated dextran coated silane layer. Decomposition of NHS-ester groups in the region between 1840-1700 cm<sup>-1</sup> was followed by new amide bond formation indicating ethanolamine binding.

Amide II vibration at 1558 cm<sup>-1</sup> dominate in the SBSR spectra measured in H<sub>2</sub>O while the SBSR spectra in D<sub>2</sub>O are characterised by amide I' vibration at 1632 cm<sup>-1</sup> (Figure 47). During ethanolamine treatment the remnants of sulphate and succinimide were washed out that is confirmed by the negative vibrations in 1130-960 cm<sup>-1</sup> region. Water exchange by D<sub>2</sub>O was almost complete since there was a very weak  $\nu(\text{OH})$  vibration at 3400 cm<sup>-1</sup> and vibration at 1632 cm<sup>-1</sup> should originate mostly from amide I'  $\nu(\text{C=O})$  band.

The surface concentrations of produced amide I' bond by ethanolamine on dextran coated silane layer was found to be  $\Gamma_{\text{exp}} = (0.71 \pm 0.10) \times 10^{-10}$  mol/cm<sup>2</sup>.

The surface concentration of  $\nu_{\text{as}}(\text{COO}^-)$  that became released from NHS after reaction with ethanolamine was found to be  $\Gamma_{\text{exp}} = (0.023 \pm 0.003) \times 10^{-10}$  mol/cm<sup>2</sup> that is approx. 2 % of overall amount of carboxylate vibrations produced by ozone.

The relevant parameters used for quantitative analysis are summarized in Table 13.

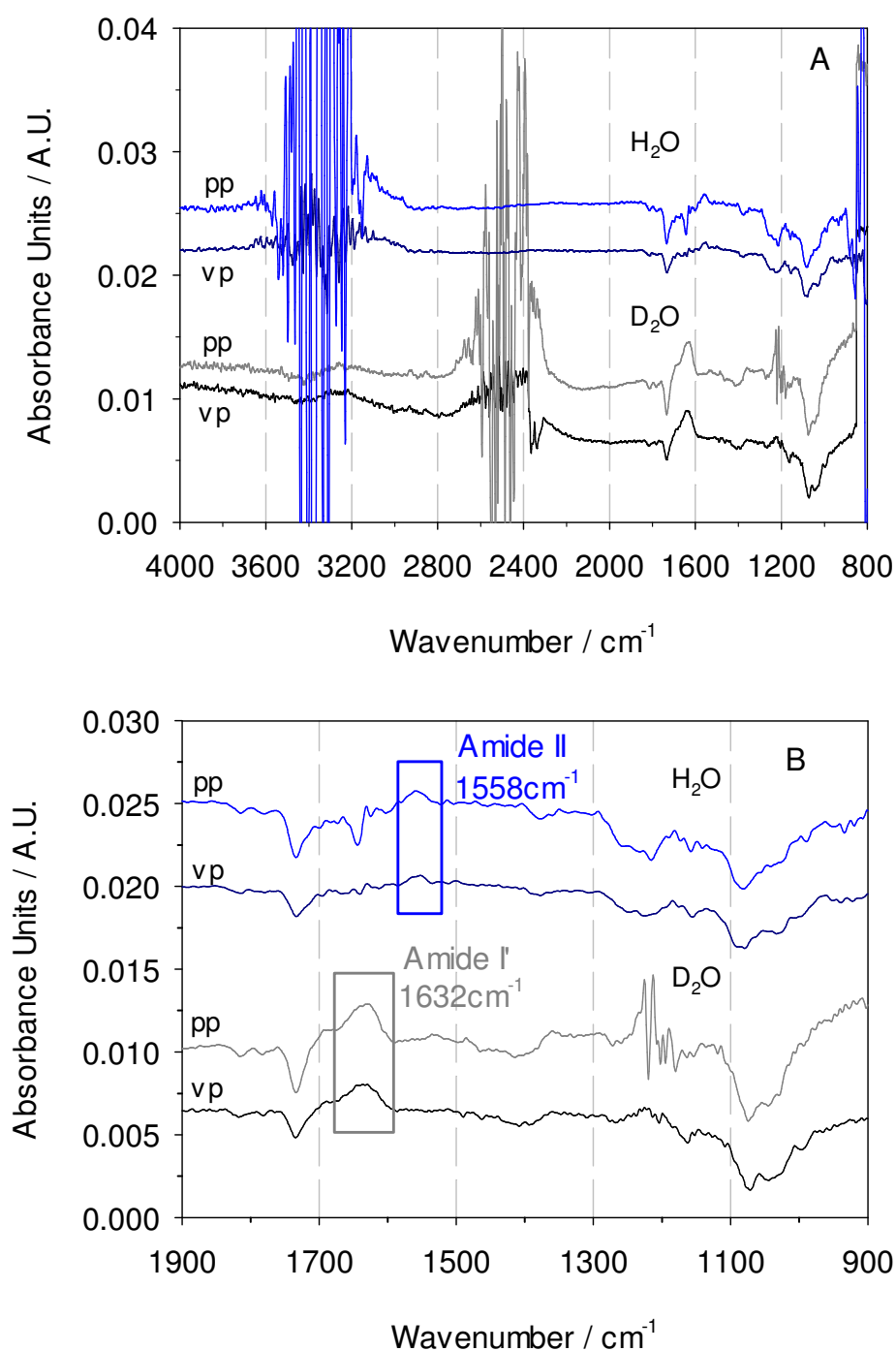


Figure 47. Ethanolamine effect on dextran coated silane layer presented as a difference between the SBSR FTIR spectra of dextran coated silane layer and the SBSR FTIR spectra of ethanolamine treated dextran coated silane layer which are taken as reference and sample, respectively. Spectra measured in  $\text{H}_2\text{O}$  are characterized by amide II bond at 1558  $\text{cm}^{-1}$  overlapping with a small amount of released  $\nu_{\text{as}}(\text{COO}^-)$  groups while amide I bond is disturbed by  $\delta(\text{OH})$ . Amide I' bond in  $\text{D}_2\text{O}$  spectra is placed at 1632  $\text{cm}^{-1}$ . Removing of the sulphate and succinimide remnants is documented by the region 1130-960  $\text{cm}^{-1}$ . A. Full spectral range; B. Expanded spectral range between 1900-900  $\text{cm}^{-1}$ . Ge MIRE;  $T=25^\circ\text{C}$ ; Angle of incidence  $\theta=45^\circ$ ; Number of active internal reflections  $N=27.97$ .

Table 13. Magnitudes and uncertainties of input parameters for amide I' and  $\nu_{as}(\text{COO}^-)$  vibrations in  $\text{D}_2\text{O}$  environment produced in the reaction with ethanolamine. Integrated molar absorption coefficient of  $\nu_{as}(\text{COO}^-)$  vibration is overtaken from ref. [114] while for amide I' see 6.5.

<i>Parameter, Symbol</i>	<i>Magnitude</i>
Angle of incidence, $\theta/\text{deg}$	$45.0 \pm 1.5$
Refractive index of germanium MIRE, $n_1$	$4.0 \pm 0.0$
Refractive index of an adsorbed/bound layer, $n_2$	$1.45 \pm 0.05$
Refractive index of bulk ( $\text{D}_2\text{O}$ ) at $1631\text{cm}^{-1}$ , $n_3$	$1.32 \pm 0.05$
Refractive index of bulk ( $\text{D}_2\text{O}$ ) at $1555\text{cm}^{-1}$ , $n_3$	$1.31 \pm 0.05$
Integrated molar absorption coefficient of amide I' ( $\text{C=O}$ ), $\int \epsilon(\tilde{\nu}) d\tilde{\nu} / 10^7 \text{ cm/mol}$	$1.57 \pm 0.17$
Integrated molar absorption coefficient of $\nu_{as}(\text{COO}^-)$ , $\int \epsilon(\tilde{\nu}) d\tilde{\nu} / 10^7 \text{ cm/mol}$	$6.10 \pm 0.10$
Integrated absorbance of amide I' ( $\text{C=O}$ ), $\int A_{pp/vp}(\tilde{\nu}) d\tilde{\nu} / \text{cm}^{-1}$	$0.056 \pm 0.003$
Integration range $1670 \pm 1 - 1610 \pm 1 \text{ cm}^{-1}$	$0.039 \pm 0.002$
Integrated absorbance of $\nu_{as}(\text{COO}^-)$ , $\int A_{pp/vp}(\tilde{\nu}) d\tilde{\nu} / \text{cm}^{-1}$	$0.008 \pm 0.001$
Integration range $1573 \pm 1 - 1508 \pm 1 \text{ cm}^{-1}$	$0.0030 \pm 0.0002$
Number of equal functional groups per molecule, $\nu$	$1 \pm 0$
Number of active internal reflections, $N$	$27.97 \pm 1$

#### 4.6.3 Overall amount of formed amide bonds produced by both dextran and ethanolamine

At the end of the experiments, irreversibly adsorbed dextran was cleaned by washing with sodium dodecyl sulphate solution (10 mg/ml SDS in PBS). The SBSR spectra of the final state of the silane layer coated with both dextran and ethanol in  $\text{H}_2\text{O}$  and  $\text{D}_2\text{O}$  environment are shown in Figure 48.



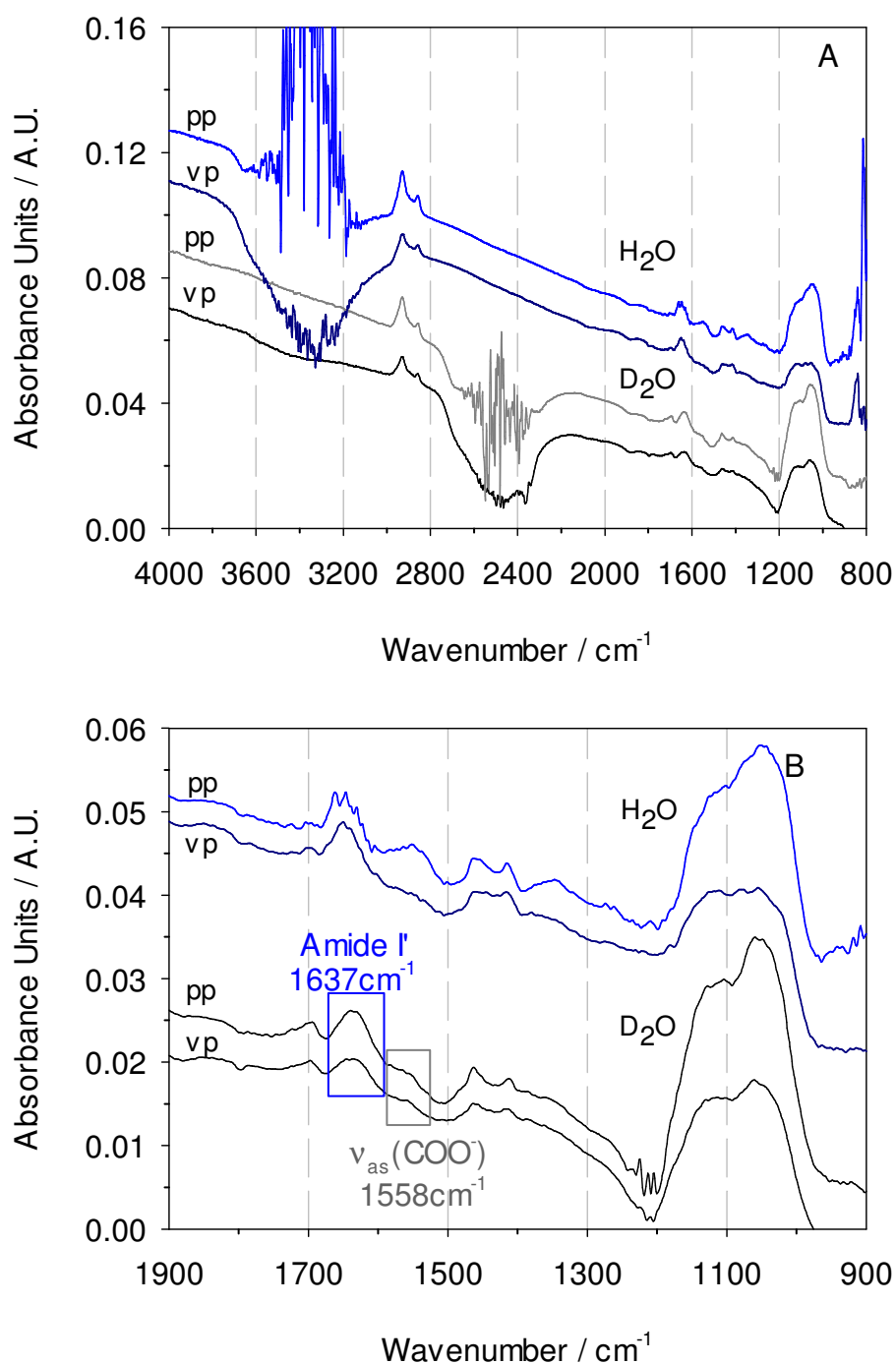


Figure 48. The SBSR FTIR pp and vp-spectra of both dextran and ethanol coated silane layer in H<sub>2</sub>O and D<sub>2</sub>O in the S channels, corresponding solvents (H<sub>2</sub>O and D<sub>2</sub>O) in the R channels. A. Full spectral range; B. Expanded spectral range between 1900-900 cm<sup>-1</sup>. Ge MIRE; T=25°C; Angle of incidence  $\theta=45^\circ$ ; Number of active internal reflections N=27.97.

Although the experiment with dextran should be treated as preliminary one, presented spectra show an evidence for amide bond formation between the carboxylic groups of the silane layer and both amino-groups of dextran and ethanolamine. It was found that optimum dextran binding is possible to reach using

dextran solution of pH=7.2 without its physisorption. Still, the binding procedure should be optimised in order to avoid baseline shift and to get better resolved amide I' and  $\nu_{as}(\text{COO}^-)$  bands in  $\text{D}_2\text{O}$  environment.

Results of the quantitative analysis should not be treated as exact ones due to manipulation with very weak and unresolved bands. The overall surface concentration of amide I' bonds produced by both amino-dextran and ethanolamine was found to be  $\Gamma_{\text{exp}}=(1.51\pm0.22)\times10^{-10}$  mol/cm<sup>2</sup>. This concentration is very close to the sum of the separately calculated surface concentrations of amide I' bonds produced by amino-dextran  $\Gamma_{\text{exp}}=(0.74\pm0.11)\times10^{-10}$  mol/cm<sup>2</sup> and ethanolamine  $\Gamma_{\text{exp}}=(0.71\pm0.10)\times10^{-10}$  mol/cm<sup>2</sup>. The overall calculated surface concentrations of carboxylate groups not reacted with amino-dextran and ethanolamine was found to be  $\Gamma_{\text{exp}}=(0.084\pm0.014)\times10^{-10}$  mol/cm<sup>2</sup> that represent ~ 5 % of the overall  $\text{COO}^-$  groups. The relevant parameters used for quantitative analysis are summarized in Table 14.

The surface concentration of  $\text{COO}^-$  groups of oxidized silane layer,  $1.59\times10^{-10}$  mol/cm<sup>2</sup>, and of the formed amide I' bonds,  $1.45\times10^{-10}$  mol/cm<sup>2</sup>, are very close to each other indicating probably amide bond formation.

Table 14. Magnitudes and uncertainties of input parameters for the final amide I' and  $\nu_{as}(\text{COO}^-)$  vibrations in  $\text{D}_2\text{O}$  environment. Integrated molar absorption coefficients of  $\nu_{as}(\text{COO}^-)$  vibration is overtaken from ref. [114] while for amide I' it was experimentally determined (see Appendix 6.5).

<i>Parameter, Symbol</i>	<i>Magnitude</i>
Angle of incidence, $\theta/\text{deg}$	45.0 $\pm$ 1.5
Refractive index of germanium MIRE, $n_1$	4.0 $\pm$ 0.0
Refractive index of an adsorbed/bound layer, $n_2$	1.45 $\pm$ 0.05
Refractive index of $\text{D}_2\text{O}$ , $n_3$	1.31 $\pm$ 0.05
Integrated molar absorption coefficient of $\nu_{as}(\text{COO}^-)$ , $\int \epsilon(\tilde{\nu})d\tilde{\nu}/10^7$ cm/mol	6.10 $\pm$ 0.10
Integrated absorbencies of $\nu_{as}(\text{COO}^-)$ , $\int A_{\text{pp/vp}}(\tilde{\nu})d\tilde{\nu}/\text{cm}^{-1}$	0.033 $\pm$ 0.002
Integration range 1589 $\pm$ 1-1521 $\pm$ 1cm <sup>-1</sup>	0.0090 $\pm$ 0.0005
Integrated molar absorption coefficient of amide I' (C=O), $\int \epsilon(\tilde{\nu})d\tilde{\nu}/10^7$ cm/mol	1.57 $\pm$ 0.17
Integrated absorbance of amide I' (C=O), $\int A_{\text{pp/vp}}(\tilde{\nu})d\tilde{\nu}/\text{cm}^{-1}$	0.120 $\pm$ 0.006
Integration range 1670 $\pm$ 1-1610 $\pm$ 1cm <sup>-1</sup>	0.085 $\pm$ 0.004
Number of active internal reflections, N	27.97 $\pm$ 1

#### 4.6.4 Bovine Serum Albumin (BSA) adsorption on dextran coated silane layer

The effectiveness of dextran covered silane layer towards non-specific protein BSA (Bovine Serum Albumin) adsorption was investigated. The protein solution (10 mg BSA/10 ml PBS) was passed above the clean Ge MIRE as well as over the dextran modified silane surface. The corresponding SBSR spectra of adsorbed protein are shown in Figure 49. The most prominent vibrations of BSA are amide I  $\nu(\text{C=O})$  stretching at  $1650\text{ cm}^{-1}$  and amide II  $\delta(\text{N-H})$  bending vibration at  $1546\text{ cm}^{-1}$ . Compared to the clean Ge MIRE dextran modified surface show significant lower non-specific adsorption.

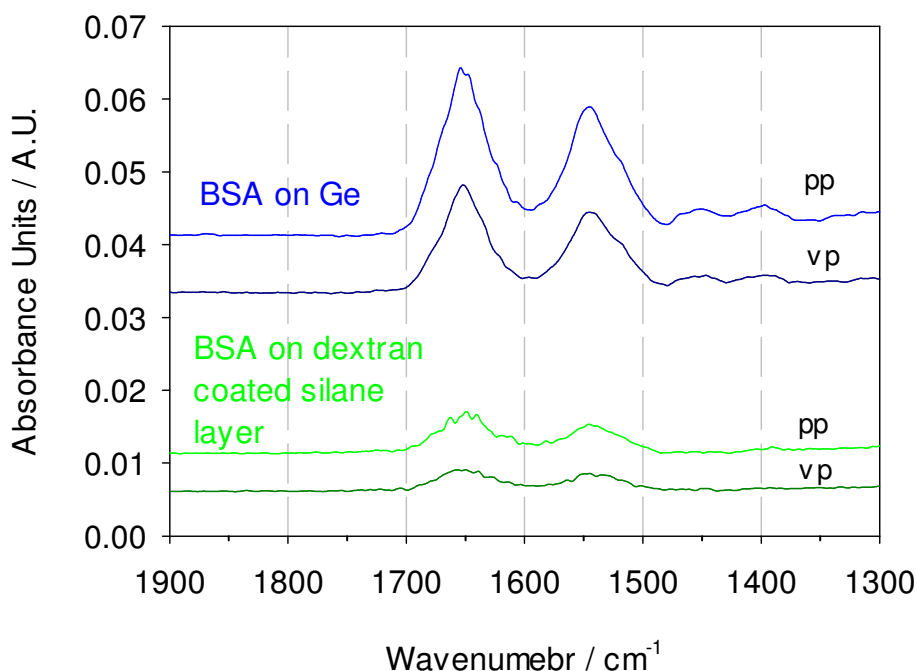


Figure 49. The SBSR FTIR pp- and vp-spectra of adsorbed BSA on a clean Ge MIRE and on dextran coated silane layer in the S channels, water in the R channels. Ge MIRE;  $T=25^{\circ}\text{C}$ ; Angle of incidence  $\theta=45^{\circ}$ ; Number of active internal reflections  $N=27.97$ .

The surface concentration of amide II bonds of adsorbed BSA on the clean Ge MIRE was found to be  $\Gamma_{\text{exp}}=(2.88\pm0.54)\times10^{-12}\text{ mol/cm}^2$  while on dextran covered silane layer  $\Gamma_{\text{exp}}=(0.63\pm0.11)\times10^{-12}\text{ mol/cm}^2$ . Comparison of these surface concentrations shows that dextran has reduced adsorption of BSA approx. 80 % in comparison to the clean Ge plate. The relevant parameters used for quantitative analysis are summarized in Table 15.

Table 15. Magnitudes and uncertainties of input parameters of amide II vibrations of adsorbed BSA in H<sub>2</sub>O environment. Integrated molar absorption coefficients are overtaken from ref. [114].

<i>Parameter, Symbol</i>	<i>Magnitude</i>
Angle of incidence, $\theta/\text{deg}$	$45.0 \pm 1.5$
Refractive index of germanium MIRE, $n_1$	$4.0 \pm 0.0$
Refractive index of an adsorbed/bound layer, $n_2$	$1.45 \pm 0.05$
Refractive index of bulk (H <sub>2</sub> O) at $1555\text{cm}^{-1}$ , $n_3$	$1.31 \pm 0.05$
Integrated molar absorption coefficient of amide II, $\int \epsilon(\tilde{\nu})d\tilde{\nu} / 10^6 \text{ cm/mol}$	$8.25 \pm 1.24$
Integrated absorbance of amide II on Ge MIRE, $\int A_{\text{pp/vp}}(\tilde{\nu})d\tilde{\nu} / \text{cm}^{-1}$	$0.714 \pm 0.036$
dextran MW=40000, Integration range $1592 \pm 1 - 1484 \pm 1 \text{ cm}^{-1}$	$0.457 \pm 0.023$
Integrated absorbance of amide II on dextran coated silane layer, $\int A_{\text{pp/vp}}(\tilde{\nu})d\tilde{\nu} / \text{cm}^{-1}$	$0.160 \pm 0.008$
Integration range $1592 \pm 1 - 1484 \pm 1 \text{ cm}^{-1}$	$0.092 \pm 0.004$
Number of equal functional groups per molecule, $\nu$	$582 \pm 0$
Number of active internal reflections, $N$	$27.97 \pm 1$

As in the case with glucosamine, experimentally determined surface concentration of BSA on a clean Ge MIRE indicates monolayer formation of BSA via its lateral surface while BSA adsorption on dextran coated silane layer was significantly reduced to a submonolayer level.

## 4.7 Possible experimental problems

### 4.7.1 Solvent (toluene) contamination by water and molecular sieve beads

While the presence of a thin chemisorbed water layer on a Ge surface plays the most important role in the silane layer formation, a physisorbed water layer as well as moisture traces in solvent (toluene) enable unwanted polymerization of the silane molecules in solution. Therefore, water content in toluene has to be minimized and carefully controlled.

Hydroxylation of 7-OTCS molecules initiated only by a stable water layer on the Ge surface is an essential starting point for the silanization reaction since 7-OTCS molecules are very reactive and even small water traces in the solvent could significantly contribute to directing reaction in an unwanted way. There are three very important sources of the system contamination by water: solvent humidity (as received), a physisorbed water layer on the Ge surface and water molecules attached to the molecular sieve remnants that are used for solvent drying.

Figure 50 shows mentioned cases of toluene contamination by water. Dry toluene spectrum without any water contaminations is presented on top of Figure 50A and B. *Solvent humidity* and probably *detached physisorbed water molecules* of an unstable water layer on the Ge surface contribute to the formation of free hydroxyl groups placed at about  $3400\text{cm}^{-1}$  (Figure 50A and B, middle). Very important source of toluene contamination by water molecules are *remnants of molecular sieve* used for toluene drying (Figure 50A and B, bottom). Not precipitated nanoparticles of molecular sieve with attached OH groups via Si-OH bonds are observed in the spectra at  $3475$  and  $3417\text{ cm}^{-1}$ . Such particles can cause unwanted effects such as fast hydrolyzation and polymerization.

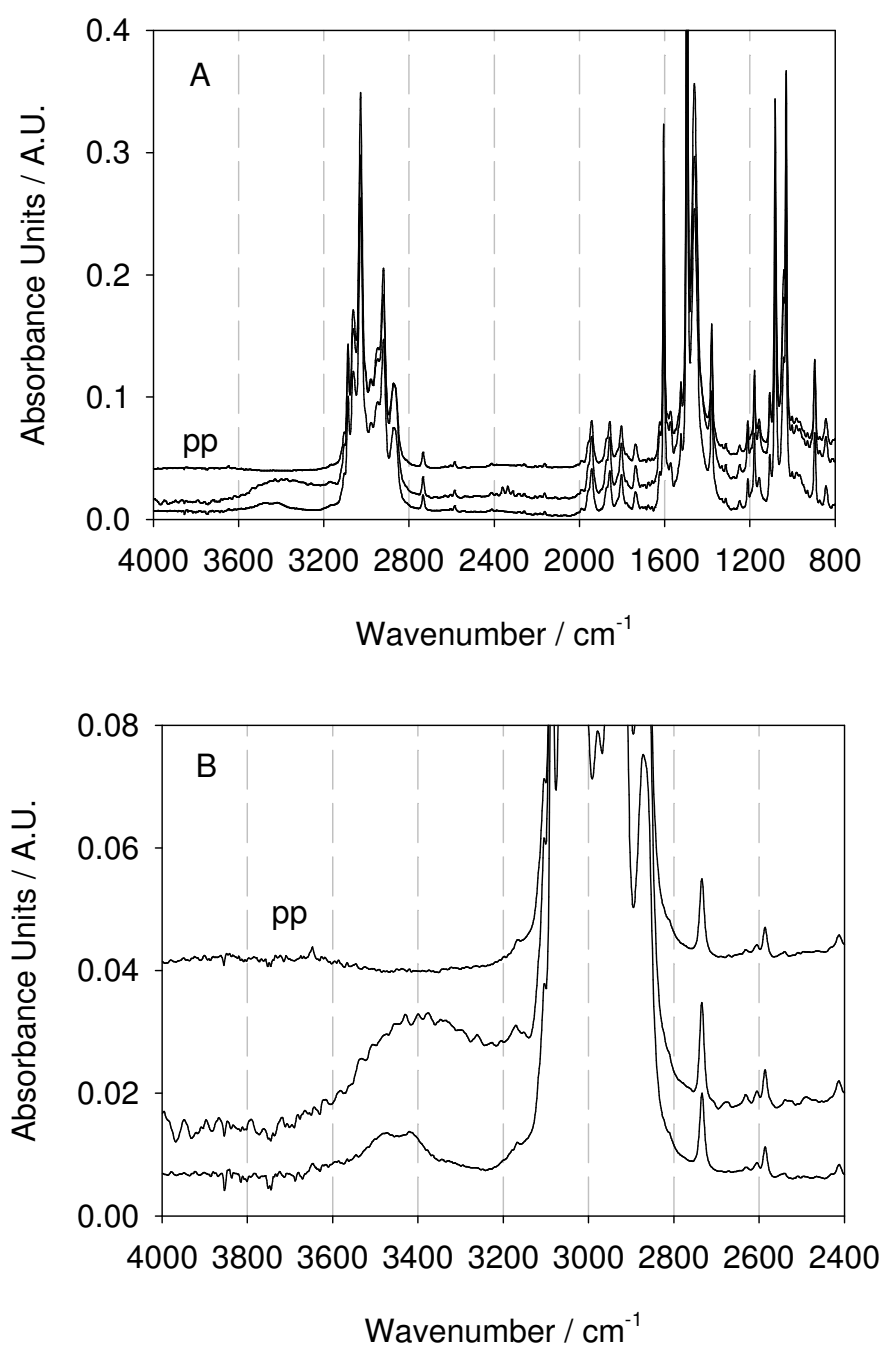


Figure 50. A. The absorbance FTIR toluene spectra showing different types of contamination. Dry toluene spectrum without any contaminations (top). Spectrum of toluene featuring OH vibrations at  $3400\text{ cm}^{-1}$  resulting from solvent humidity (middle). Spectrum of contaminated toluene solution by molecular sieve used as a drying reagent where Si-OH vibrations are placed at  $3475$  and  $3417\text{ cm}^{-1}$  (bottom). B. Expanded spectral range of toluene spectra between  $4000$  and  $2400\text{ cm}^{-1}$ . All spectra were measured with parallel (pp) polarized light. Reference: dried hydroxylated Ge MIRE.  $T=15^\circ\text{C}$ ; Angle of incidence  $\theta=45^\circ$ ; Number of active internal reflections  $N=19.4$ .

Figure 51 shows an increase of water content in toluene with time. Both cuvettes reference (Figure 51A) and sample (Figure 51B) were filled with toluene. The first time-resolved absorbance spectra of toluene in the R and S compartments separately were recorded in the stationary state (light blue and red spectra, respectively). Inlet and outlet tubes of reference cuvette were closed not to be affected by air humidity during measurement. Toluene constantly exposed to laboratory atmosphere was recirculating only through the sample cuvette with a pump velocity of  $0.83 \mu\text{l/sec}$  and spectra were measured after 25, 175, 325 and 475 min of the initiation of toluene recirculation. One can notice that toluene spectra of the reference compartment were stable indicating that the closed system was air resistant. On the other side, toluene humidity in the sample cuvette monitored over time was confirmed by the presence of OH vibrations in the region between  $3600\text{-}3200 \text{ cm}^{-1}$ .

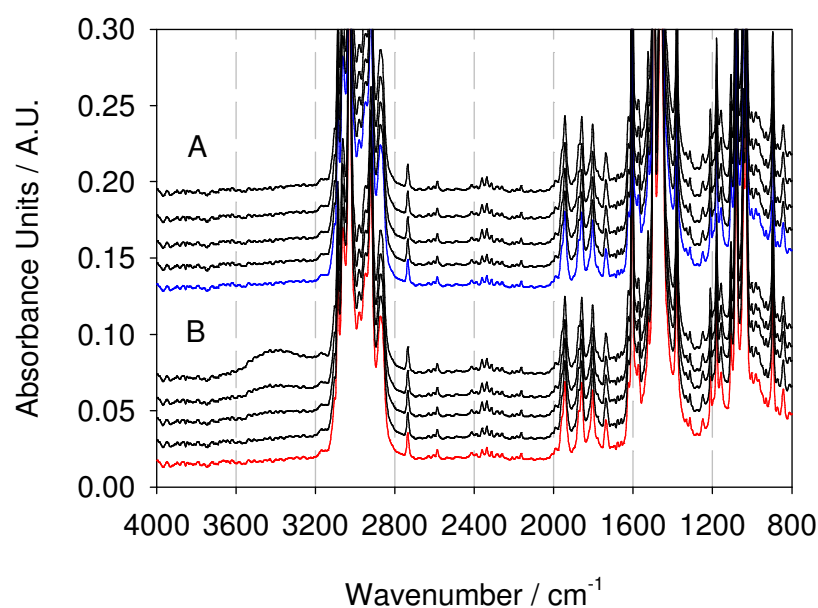


Figure 51. Selected time-resolved absorbance FTIR spectra of toluene showing the influence of the laboratory humidity only in the sample cuvette (B) after 25, 175, 325 and 475 min of toluene exposure to laboratory air during toluene recirculation. Hydroxylic vibration at  $3400 \text{ cm}^{-1}$  was increased during time. Reference cuvette containing toluene (A) was clamped on both inlet and outlet sides. All spectra were measured with parallel (pp) polarized light. Reference: dried Ge MIRE.  $T=15^\circ\text{C}$ ; Angle of incidence  $\theta=45^\circ$ ; Number of active internal reflections  $N=25.33$ .

Although solvent humidity and water vapour coming into the SBSR cell strongly contribute to unwanted polymerization of 7-OTCS molecules, their presence can be

avoided by using anhydrous solvents and by handling in extremely dry laboratory conditions. When molecular sieve is used for drying of organic solvents stirring plays an essential role in this process because diffusion of dissolved H<sub>2</sub>O to the surface of sedimented sieve particles would be an extremely slow process. We suggest that after drying of toluene the time let for sieve sedimentation must be several hours in order to avoid a significant presence of nanoparticle sized sieve close to the upper surface of the solvent. A suspension containing such small particles appeared quite clear and could not be detected by visually. Working with it, however, may lead to strange observations such as the oxidation of the end-standing double bond of the silane layer without addition of any oxidative chemicals, as we unambiguously revealed by FTIR ATR spectroscopy.

#### **4.7.2 Silane layer preparation on the Ge MIRE catalyzed by nanoparticles of molecular sieve**

The aim of silanization was functionalization of the hydroxylated Ge MIRE surface by 7-OTCS molecules, i.e. the formation of a covalently bound silane layer. Figure 52 shows the SBSR spectra of the silane layer bound to the Ge MIRE only in the S cuvettes. Typical silane layer bands are clearly visible:  $\nu_{as}(\text{CH}_2)$  and  $\nu_s(\text{CH}_2)$  at 2927 and 2856 cm<sup>-1</sup>,  $\nu_{as}(\text{CH}=\text{CH}_2)$  at 3077 cm<sup>-1</sup>,  $\nu(\text{C}=\text{C})$  at 1641 cm<sup>-1</sup> and  $\gamma_{op}(\text{CH}=\text{CH}_2)$  at 911 cm<sup>-1</sup>. A broad low structured shape between 1250-975 cm<sup>-1</sup> representing vibrations such as  $\nu(\text{Ge-O-Si})$ ,  $\nu(\text{Si-O-Si})$  and  $\nu(\text{Si-OH})$  is related to chemical connection of 7-OTCS molecules to the Ge surface and probably 7-OTCS polymerization [118].



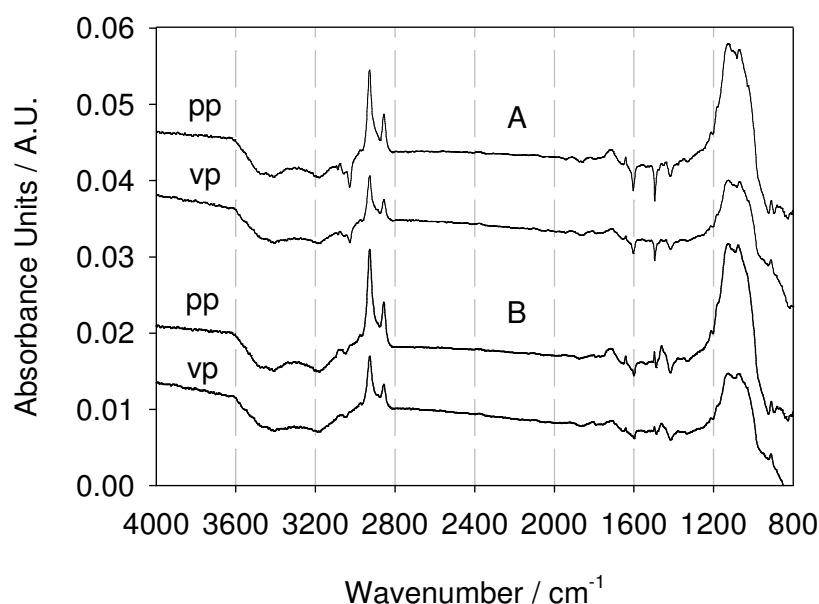


Figure 52. Parallel (pp) and perpendicular (vp) polarized SBSR spectra of a silane layer bound to the Ge MIRE in the S cuvettes. Toluene in the R cuvettes. For typical absorption bands of the silane layer see text. The broad negative band near  $3300\text{ cm}^{-1}$  and the small negative band overlapping with double bond vibration at  $1640\text{ cm}^{-1}$  are expected to result from a thin water layer adsorbed on the Ge MIRE.  $T=15^{\circ}\text{C}$ ; Angle of incidence  $\theta=45^{\circ}$ ; Number of active internal reflections  $N=19.4$ .

However, three relevant differences between this and typical silanization experiment should be mentioned. First, unusually structured band around  $3300\text{ cm}^{-1}$  featuring two troughs at  $3420$  and  $3170\text{ cm}^{-1}$  is observed. Second, a new band appeared at  $1718\text{ cm}^{-1}$  which is assigned to  $\nu(\text{C}=\text{O})$  of  $-\text{COOH}$  or  $-\text{CHO}$  of the partially oxidized end-standing double bond. Third, it should be mentioned that in some SBSR measurements very small wavelength-shifts between light passing through R and S channels are observed. This was the reason for the sigmoid shape of the toluene bands at  $1604\text{ cm}^{-1}$  and  $1495\text{ cm}^{-1}$ .

Due to unusually structured band around  $3300\text{ cm}^{-1}$  and possible oxidation of a double bond, ultrastructural and analytical chemical investigations of the silane layer by Atomic Force Microscopy (AFM) and Energy Dispersive X-ray Analysis (EDX) using an Environmental Scanning Electron Microscope (ESEM) were performed. It was found that nanoparticles in the range of 10 to 100 nm are incorporated into the silane layer as well as adsorbed to the blank germanium surface in the reference cuvettes. Figure 53 shows AFM picture of the silane layer which lead to the spectra

presented in Figure 52. Nanoparticles are inhomogeneously incorporated into the silane layer and appear as white towers with a mean size in the 60 nm range.

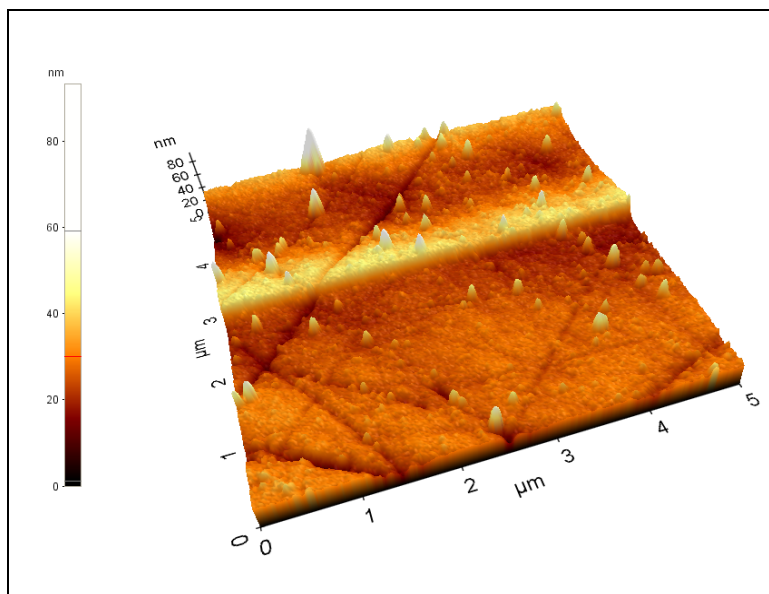


Figure 53. AFM image of the silane layer spectroscopically presented in Figure 52. The white towers have a mean size of approximately 60 nm range. [119] The silane layer is expected to cover the whole surface of the Ge MIRE.

Sample and reference cuvettes, both exposed to toluene dried by molecular sieve particles, were qualitatively analyzed by means of Energy Dispersive X-ray Analysis (EDX). It was found that nanoparticles were present on both, reference (Figure 54) and sample (not shown), respectively. Al and Si atoms turned out to be the main components. Furthermore, traces of elements such as C, O, F and K were detected. Measurements on the particle and on the Ge crystal gave clear evidence that the enhanced amount of Si, Al, K, O can be assigned to the molecular sieve remnants (e.g. zeolites).

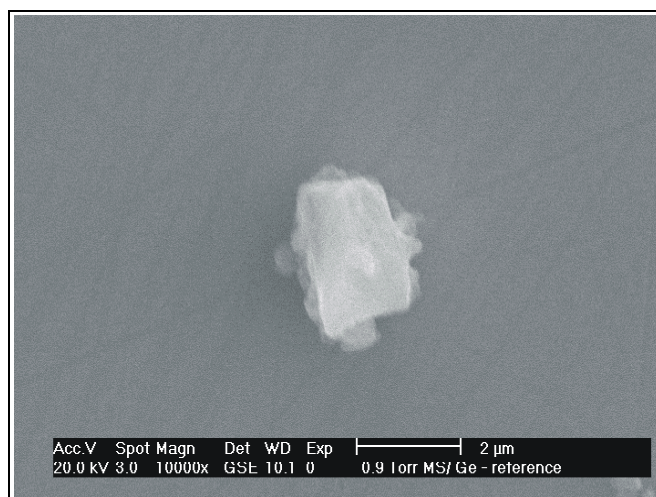


Figure 54. ESEM picture of the reference cuvettes exposed to toluene containing molecular sieve remnants. Qualitative analysis was performed by means of Energy Dispersive X-ray Analysis (EDX). It was found that molecular sieve was present on the reference and sample surface with Al and Si atoms as the main components as well as with some other traces of elements such as C, O, F, K. Measurements on the particle and on the Ge crystal area gave clear evidence that the enhanced amount of Si, Al, K, O can be assigned to molecular sieve remnants (e.g. zeolites).

In the actual case as presented in Figure 52 the surface concentration of these particles is expected to be higher on the blank germanium surface in the reference channel than on/in the silane layer in the sample channel, resulting in a negative difference band. This band is overlapping in the S-channel by a weaker negative band at  $3300\text{ cm}^{-1}$ , which is paralleled by a weak negative band at  $1640\text{ cm}^{-1}$ . These bands are expected to result from a compact water monolayer [107], which was removed by the reaction with 7-OTCS, however, remained unaffected by dry toluene in the R channel. [39]

Partial oxidation of the double bond was unambiguously observed by the appearance of a new band at  $1718\text{ cm}^{-1}$ , even when the immobilized layer was kept in pure toluene for several hours. This band was shown to result from  $\text{--COOH}$  [39]. It is now expected that molecular sieve remnants have catalyzed the oxidation of the double bond by small amounts of oxygen dissolved in pure toluene. It is already known that the framework of molecular sieve is composed of  $\text{SiO}_4$  and  $\text{AlO}_4$  tetrahedra, where each aluminium ion causes a net negative charged framework. [120] Therefore, positive metal ions (usually from the group IA or IIA) or protons are required to balance the negatively charged framework. Because of the presence of metal cations or protons in molecular sieve structure, sieve has cation-exchange ability or acidic

properties. The acidic property of the sieve takes the major role in catalytic materials for acid-catalyzed reactions. [121] The unusual shape of the broad band near 3300  $\text{cm}^{-1}$  which is spectroscopically observed to parallel the self-oxidative process, may now be assigned to OH stretching vibrations of molecular sieve remnants.

Using the integrated absorbancies of symmetric and asymmetric  $\text{CH}_2$  stretching vibrations as indicated in Table 16 the surface concentration resulted in  $\Gamma_{\text{CH}_2, \text{mean}} = (8.70 \pm 0.90) \times 10^{-10} \text{ mol/cm}^2$ . From this quantity, one may estimate the mean layer thickness  $d$ , based on its density  $\rho \approx 0.90 \pm 0.10 \text{ g/cm}^3$  [109] and molecular mass  $M_r = 187.15 \text{ g/mol}$  to be  $d \approx (\Gamma_{\text{exp}} \times M_r) / \rho = 1.8 \pm 0.3 \text{ nm}$ . The experimentally determined mean surface concentration of  $\Gamma_{\text{CH}_2, \text{mean}} = 8.70 \times 10^{-10} \text{ mol/cm}^2$  is about 80 % above the most densely packed monolayer coverage ( $\Gamma_{\text{CH}_2, \text{max}} = 4.88 \times 10^{-10} \text{ mol/cm}^2$ ) and indicates that most probably polymerization of 7-OTCS molecules has occurred.

The mean direction of the transition moments of symmetric and asymmetric  $\text{CH}_2$  stretching vibrations,  $\nu_s(\text{CH}_2)$  and  $\nu_{\text{as}}(\text{CH}_2)$ , with respect to the normal of the layer (z-axis) may be estimated from the experimentally determined dichroic ratios  $R$ , according to eq. (19). The relevant data are summarized in Table 16. Averaging the dichroic ratios of both vibrations results in  $R_{\text{CH}_2, \text{mean}} = 1.84 \pm 0.05$  which corresponds to a mean angle between the corresponding transitions moments and the z-axis of  $\Theta = 58.2^\circ \pm 0.3^\circ$ . Since these transition moments are normal to the local molecular axis, one may estimate the mean direction of the hydrocarbon chains of the silane assembly to be inclined by  $\delta = 31.8^\circ \pm 0.2^\circ$  against the normal to the MIRE (z-axis). It should be noted that an isotropic thin layer would exhibit a dichroic ratio of  $R_{\text{iso}} = 2.13 \pm 0.27$  which is significantly different from the experimental value, thus indicating a rather good ordering of the spontaneously formed silane layer.

Table 16. Summary of quantitative data on the surface concentration and orientation of the silane layer based on the evaluation of CH<sub>2</sub> symmetric and asymmetric stretching vibrations.

	$\nu_s(\text{CH}_2)$	$\nu_{as}(\text{CH}_2)$
Integration limits/cm <sup>-1</sup>	2873-2823	2968-2898
$\int A_{pp}(\tilde{\nu}) d\tilde{\nu}$	$0.071 \pm 0.003$	$0.256 \pm 0.013$
$\int A_{vp}(\tilde{\nu}) d\tilde{\nu}$	$0.038 \pm 0.001$	$0.144 \pm 0.007$
$R_{\text{exp}}$	$1.89 \pm 0.10$	$1.79 \pm 0.09$
$\Gamma_{\text{exp}}/10^{-10} \text{ mol/cm}^2$	$8.65 \pm 0.97$	$8.65 \pm 0.98$
d/nm	$1.8 \pm 0.3$	$1.8 \pm 0.3$
$\langle \cos^2 \Theta \rangle$	0.29	0.27
$\Theta /^\circ$	$57.48 \pm 0.44$	$58.83 \pm 0.44$
$S_{\text{seg}}$	$-0.066 \pm 0.010$	$-0.098 \pm 0.010$
$S_{\text{mol}}$	$0.27 \pm 0.15$	$0.39 \pm 0.21$

#### 4.7.3 Different types of toluene incompensation between reference and sample cuvettes

The SBSR spectrum of toluene measured at the nominal R and S positions usually features a significant incompensation of the intensity of toluene bands. This incompensation is due to inequalities between R and S channels, a slight difference in the number of internal reflections in the channels. The reason for that is the hydrodynamically optimized shape of a flow-through cuvettes, which is half-circular at the entrance and exit. Since this spectrum referred to as "SBSR reference spectrum" is used for all forthcoming measurements, good toluene compensation is required.

The number of active internal reflections may be altered in a narrow limit by choosing small deviations from the nominal lift positions. The nominal lift positions are 580 and 2100 motor steps for the R and S cuvette, respectively. Thus different motor steps,  $580 \pm (n \times 40)$  and  $2100 \pm (n \times 40)$  where  $n=0,1,2,\dots$ , were selected for the measurement of new SBSR toluene spectra. Since 400 steps are equal to 2.5 mm, the change of 40 motor steps places the cuvettes per 250  $\mu\text{m}$  up and down from the nominal positions. The automatic compensation of the intensity of the selected solvent marker band at  $1495\text{cm}^{-1}$  was performed by means of Matlab program. The evaluated program required a sequence of single channel R and S spectra of the solvent (toluene) with

the increased lift position by a given increment. The optimized lift positions were then automatically evaluated by searching for two single channel spectra, one from the S channel and the other from the R channel, which led to complete compensation of the toluene marker band (Figure 55).

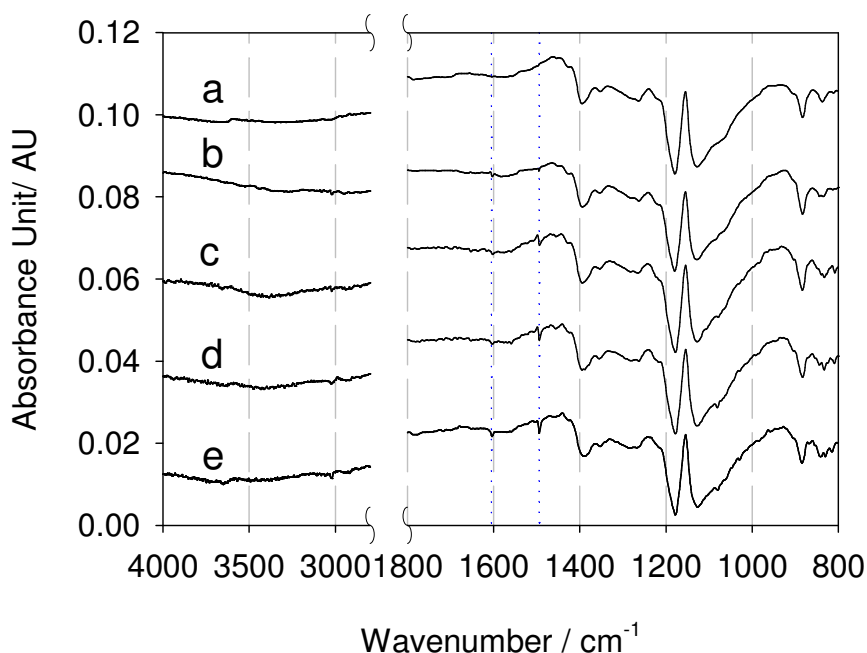


Figure 55. **a.** Parallel polarised SBSR spectra of dried hydroxylated Ge MIRE at nominal R and S lift positions, 580 and 2100 lift motor steps. Below there are SBSR spectra of toluene in both R and S compartments at different R and S measurement positions. **b.** the best compensated SBSR spectrum at measurement positions of 500 (R) and 2100 (S); **c.** 620 (R) and 2060 (S), **d.** 580 (R) and 2100 (S), **e.** 540 (R) and 2140 (S). Region between 1250-1100 $\text{cm}^{-1}$  features not compensated viton vibrations, material that is used for O-ring production.  $T=15^{\circ}\text{C}$ ; Angle of incidence  $\theta=45^{\circ}$ ; Number of active internal reflections  $N=19.4$ .

Figure 56 presents toluene incompensation at different measurement lift positions. It shows the difference between the SBSR spectra of dried hydroxylated Ge MIRE (Figure 55a) and the SBSR spectra of toluene (Figure 55b-e, toluene in both R and S cuvettes) where viton vibrations are completely subtracted leaving only toluene incompensation at 1600 and 1500  $\text{cm}^{-1}$ .

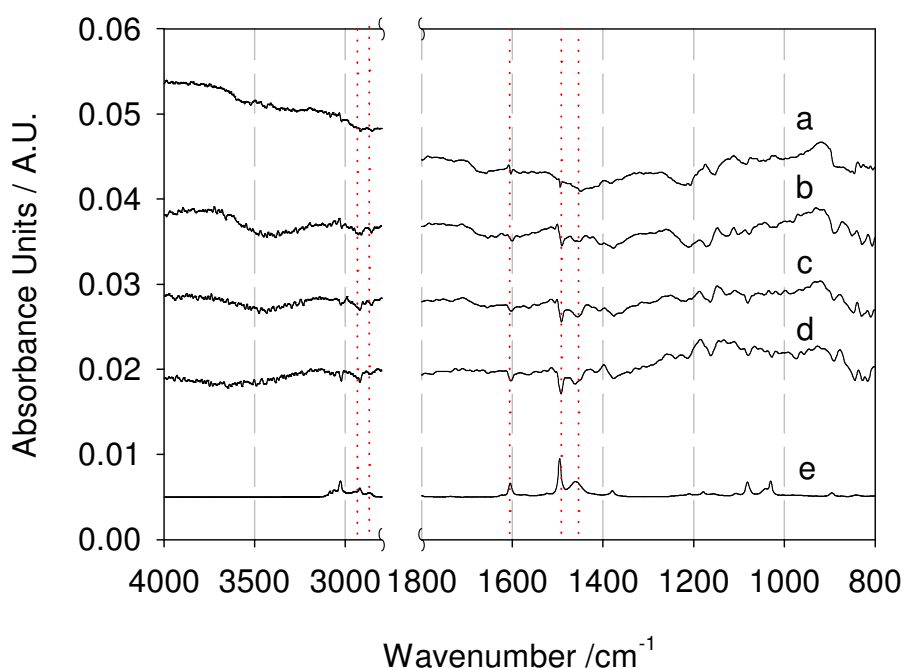


Figure 56. Incompensation of toluene marker bands at  $\sim 1600$  and  $\sim 1500\text{cm}^{-1}$  at different measurement positions. Difference between spectrum presented in Figure 55a (reference) and spectra in Figure 55b-d (samples) shows toluene incompensation while viton vibrations are subtracted. Toluene spectrum divided by 185 presented for comparison (e).  $T=15^{\circ}\text{C}$ ; Angle of incidence  $\theta=45^{\circ}$ ; Number of active internal reflections  $N=19.4$ .

#### 4.7.4 Silane layer preparation on the CdTe MIRE

CdTe MIRE was used without activation step in order to have access to non-hydrolyzed  $\nu_s(-\text{SiCl}_3)$  and  $\nu_{as}(-\text{SiCl}_3)$  vibrations at  $564\text{ cm}^{-1}$  and  $587\text{ cm}^{-1}$ . Moreover, since dry CdTe exhibits a hydrophobic surface, one could expect that no tightly bound water layer would be present as in the case of Ge.

Figure 57A shows the state of 2 % 7-OTCS solution in toluene after approx. 9 hours of contact with the CdTe MIRE. The presence of  $-\text{SiCl}_3$  moieties in silane solution is clearly proved by the corresponding Si-Cl stretching vibrations. However, unexpectedly, 7-OTCS adsorbed also irreversibly to CdTe even without OH groups at the surface. This is revealed upon exchanging 7-OTCS solution by pure toluene, Figure 57B. There remained a tightly bound silane layer on the CdTe surface lacking of any Si-Cl bonds. Since CdTe surface was not water activated before silanisation step, the only possible source enabling hydrolyzation of Si-Cl groups could be molecular sieve remnants in toluene present more in the sample than in the

reference cuvette. Figure 57C presents the background compensated physisorbed polymerized silane layer.

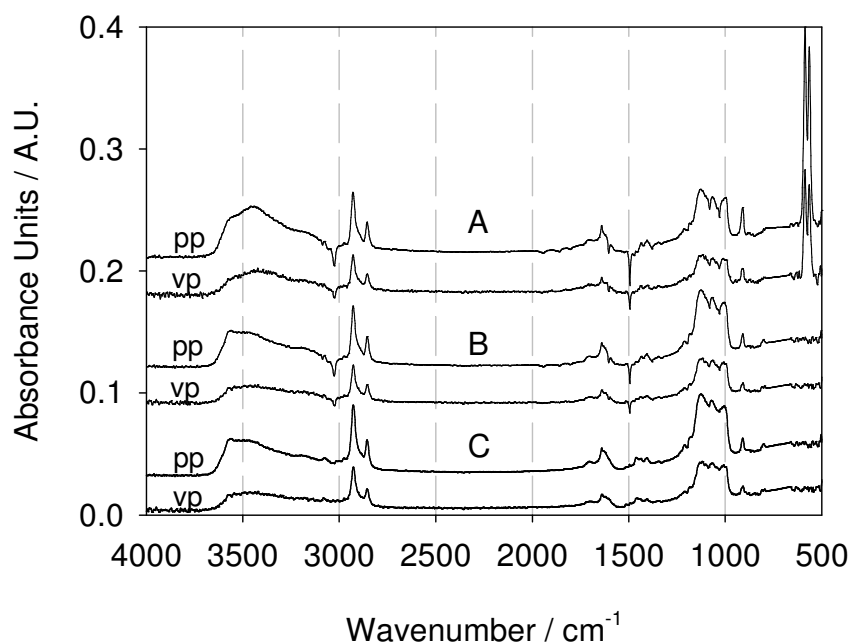


Figure 57. Parallel (pp) and perpendicular (vp) polarized SBSR FTIR spectra of the physically bound silane layer to the CdTe MIRE. A. Adsorbed silane layer in contact with 2 % 7-OTCS solution (v/v) where  $\text{SiCl}_3$  stretching vibrations placed at 587 and 565  $\text{cm}^{-1}$  dominate in the spectra. B. and C. Adsorbed silane layer after replacing 7-OTCS solution by pure toluene have lost all  $\text{SiCl}_3$  stretching vibrations due to complete polymerization to either Si-O-Si (1250-975  $\text{cm}^{-1}$ ) in oligomers or Si-OH bands (3600-3100  $\text{cm}^{-1}$ ) without and with toluene compensation, respectively. The region between 850-650  $\text{cm}^{-1}$  is cut due to strong toluene absorption.  $T=15^\circ\text{C}$ ; Angle of incidence,  $\theta=45^\circ$ ; Refractive index of CdTe,  $n_1=2.67$ ; Number of active internal reflections,  $N=12.7$ .

We suggested that the broad band in the region between 3600-3100  $\text{cm}^{-1}$  results predominantly from free  $\nu(\text{Si-OH})$  vibrations of incorporated molecular sieve remnants into the silane layer, enabling polymerization at the interface. Moreover, these remnants caused a partial oxidation of a double bond to  $-\text{COOH}$  without using any reagent which is confirmed by appearance of a band at 1710  $\text{cm}^{-1}$ .



## Chapter 5 CONCLUSIONS

This work presents *in situ* monitoring of the formation and quantitative analysis of biomimetic surfaces composed of a silane layer and glucose species (glucose and dextran, separately) produced on Ge MIREs. The first step in building of such structures was silanization of the Ge MIRE by 1 % 7-Octenyltrichlorosilane (7-OTCS) in toluene which turned out to be very critical with respect to spurious water content at any place in the reaction system. As documented, 7-OTCS solution in toluene used in our experiment was dry enough in order to avoid hydrolysis of the Si-Cl<sub>3</sub> bonds in a large scale already in solution. We suggest that a compact tightly bound water layer on the hydroxylated Ge surface played an important role in the silanization process. A thin water layer on Ge seems to be resistant to the presence of dry toluene; however, it was chemically removed by the reaction with Si-Cl<sub>3</sub> resulting in HCl, Cl<sub>x</sub>-Si-(OH)<sub>y</sub> and Ge-O-Si-(OH)<sub>z</sub> at least at the beginning of the reaction. This water layer on the Ge MIRE enabled polymerization of 7-OTCS molecules either in solution or of the immobilized layer. In our case, the latter is expected to be more dominant, because 7-OTCS solution was permanently replaced by toluene.

We have found that two types of reactions took place from the beginning of the silanization reaction. Kinetic data analysis gave evidence for an accelerated initial phase where very reactive 7-OTCS molecules reaching Ge surface enabled very fast formation of only Ge-O-Si bonds within approx. 1 min. The second type was much slow process related to the rearrangement of chemisorbed molecules via Si-O-Si bonds as well as to polymerization.

By the quantitative analysis of symmetric  $\nu_s(\text{CH}_2)$  and asymmetric  $\nu_{as}(\text{CH}_2)$  stretching vibrations of the silane layer the thickness of layer was calculated to be 2.3 nm. The experimentally determined mean surface concentration of CH<sub>2</sub> groups,  $\Gamma_{\text{exp}} = (6.33 \pm 0.70) \times 10^{-10} \text{ mol/cm}^2$ , was about 30 % above the most densely packed monolayer coverage and indicated that most probably polymerization has occurred as a parallel reaction to covalent binding to the Ge surface. This partial multilayer formation had to be expected also due to the fact that no Si-Cl<sub>3</sub> vibrations could be detected in an immobilized layer on a CdTe MIRE indicating complete hydrolization

within the layer. The mean inclination of hydrocarbon chains was found to be  $\delta=28.4\pm0.3^\circ$  thus exhibiting a certain overall ordering of the assembly. Also the mean order parameters of the  $\text{CH}_2$ -groups in the hydrocarbon chains,  $S_{\text{seg}}$  and  $S_{\text{mol}}$ , indicated a rather good ordering of the layer.

A further surface chemical step was the oxidation of the end-standing double bond ( $\text{C}=\text{C}$ ) of the silane layer by exposing the dried layer to an argon diluted flow of ozone. The process had led directly to the aimed carboxylic acid groups which could be unambiguously proved by both the SBSR and chemical modulated excitation (c-ME) measurements using buffer solutions at  $\text{pH}=4$  and  $\text{pH}=8$ . Moreover, c-ME demonstrated the power of ME techniques with respect to sensitivity, long term stability and selectivity. Finally, it should be mentioned that the duration of exposition to ozone, as well as the ozone concentration had turned out to be very critical, because complete oxidation of the hydrocarbon chain might occur if exposition was too long. The Si-O-Ge bonds, however, remained unaffected. In this respect *in situ* monitoring turned out to be of great importance. Nevertheless even in our approach a loss of about one third of  $\text{CH}_2$  groups occurred as revealed by a quantitative analysis of the final layer.

One of the problems which could occur parallel to the silanization was partial oxidation of the end-standing double bond of the silane layer. It can be unambiguously observed by the appearance of  $\nu(\text{C}=\text{O})$  vibration of COOH groups even when the immobilized layer was kept in pure toluene for several hours. Ultrastructural and analytical chemical investigations by Atomic Force Microscopy (AFM) and Energy Dispersive X-ray Analysis (EDX) using an Environmental Scanning Electron Microscope (ESEM) revealed particles in the range of 10 to 100 nm incorporated into the silane layer. They were identified as remnants of molecular sieve. We conclude that dissolved and adsorbed nanoparticles of molecular sieve have acted as catalyst for the oxidation of the double bond by small amounts of oxygen dissolved in toluene. Such phenomena can be avoided by expanding sedimentation time for molecular sieve in toluene after stirring to one night and sucking off toluene just below its upper surface. Moreover, degassing of toluene immediately before use is of significant importance, too. Optimum results were achieved by using an in-line vacuum degassing system.

After the oxidation of the silane layer, the next step was activation of carboxylic terminated silane layer groups. It was achieved using by a mixture of NHS and CMC

in water. Formed NHS-esters were relatively stable in a solvent but during the solvent flow, their decomposition occurred. Therefore, immediately after NHS-ester formation amine solution should be introduced into the system.

Although amide bond formation is recommended in the literature at pH at least one and a half unit below  $pK_a$  value that would be at pH=5.4 for glucosamine, it was not possible for reaction to occur under this condition. In our experiment glucosamine and amino-dextran were bound to the silane layers at pH=7.2. Unreacted NHS-ester groups of the silane layer were deactivated by treatment with ethanolamine solution with additional formation of amide bonds.

Amide bond formation was followed by releasing of a certain amount of carboxylate groups from the NHS-esters. This occurred due to short time stability of the NHS-ester groups. It should be noted that the integrated molar absorption coefficient of  $\nu_{as}(\text{COO}^-)$  as a rough approximation obtained from sodium polyglutamate and sodium acetate solutions was overtaken from [114]. Also, the wavelength-dependent refractive indices of liquid  $\text{D}_2\text{O}$  are approximated from those of liquid  $\text{H}_2\text{O}$ . Therefore, quantitative analysis of amide I' bonds in  $\text{D}_2\text{O}$  was much more precise and valuable than analysis of released carboxylate groups.

Quantification analysis of the formed amide bonds was performed by the SBSR spectra measured in  $\text{D}_2\text{O}$  environment in order to avoid overlapping between formed amide I bonds and  $\delta(\text{OH})$  vibration in  $\text{H}_2\text{O}$  environment. For that purpose, integrated molar absorption coefficient of amide I' in  $\text{D}_2\text{O}$  was determined using different concentrated 2-acetamido-2-deoxy-D-glucose solutions.

In the case of glucosamine, the overall amount of produced amide I' bonds was found to be  $\Gamma_{\text{exp}}=(2.03\pm0.21)\times10^{-10}$  mol/cm<sup>2</sup> where contribution of both glucosamine and ethanolamine was approximately the same. The surface concentration of COOH groups produced by ozone  $\Gamma_{\text{exp}}=(2.43\pm0.40)\times10^{-10}$  mol/cm<sup>2</sup> and the overall calculated surface concentration of carboxylate groups not reacted with glucosamine and ethanolamine  $\Gamma_{\text{exp}}=(0.41\pm0.10)\times10^{-10}$  mol/cm<sup>2</sup> show that approximately 17 % of these groups did not reacted.

In preliminary experiment with amino-dextran the overall sum of the surface concentrations of the formed amide I' bonds produced by amino-dextran and ethanolamine was found to be  $\Gamma_{\text{exp}}=(1.45\pm0.21)\times10^{-10}$  mol/cm<sup>2</sup>. The surface concentration of  $\text{COO}^-$  groups of the oxidized silane layer was calculated to be  $\Gamma_{\text{exp}}=(1.59\pm0.24)\times10^{-10}$  mol/cm<sup>2</sup> while of unreacted  $\text{COO}^-$  groups at the end of

experiment  $\Gamma_{\text{exp}} = (0.084 \pm 0.014) \times 10^{-10} \text{ mol/cm}^2$  representing  $\sim 5 \%$  of overall COOH groups produced by oxidation.

Both glucose covered silane surfaces were inert in a certain amount to protein BSA adsorption. Glucose and dextran have reduced adsorption of BSA approx. 70 and 80 % in comparison to the clean Ge plates respectively. Slightly better adsorption reducing was achieved with dextran that could be explained by less amount of  $\text{COO}^-$  groups existing on the surface at the end of experiment.

At the end, it could be concluded that glucose monomer (glucosamine hydrochloride) is equally effective as glucose polymer (amino-dextran) that is much more expensive. The future experiments should show behaviour of these surface when immobilisation of other biomolecules occur.

The flexibility to design these films providing desired surface properties and to control the structure in the nanometer regime is an attractive feature of self-assembled films. Since direct information on investigated functional groups, their orientation in space and their surface concentration are available, we believe that the application of FTIR ATR techniques should gain interest because it can accelerate new developments of chemical surface modifications by direct insight on a molecular level.

## Chapter 6 APPENDIX

### 6.1 Mechanism of ozonization

The following mechanism of oxidation has been already reported. [122,123] The ozone initially attacks double bond via a cycloaddition reaction forming the unstable 5-membered ring called primary *molozonide* (Figure 58). The 5-membered ring of the unstable molozonide has a plane of symmetry that passes through the central oxygen atom and the C-C bond. In the decomposition of the molozonide, not only a weak O-O bond is broken but a relatively strong C-C  $\sigma$ -bond, too.

Because of the symmetry, there are two mechanistic pathways by which the molozonide can decompose to produce either *formaldehyde* and a surface-bound *Criegee intermediate* (Figure 58) or a surface-bound formaldehyde and a gas-phase Criegee intermediate. [124] In the case when formaldehyde is released into the gas phase, the Criegee intermediate remains bound to the surface. This surface-bound intermediate can decompose in several ways, leading to the formation of carbon dioxide and an alkane or a carbonyl or carboxylic acid. [123]

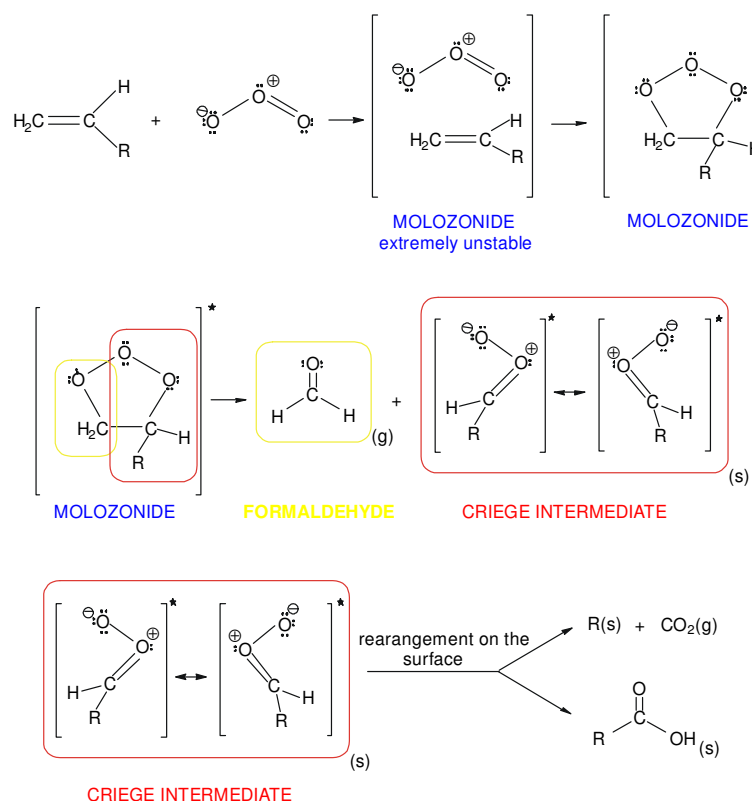


Figure 58. Mechanism of ozonolysis.

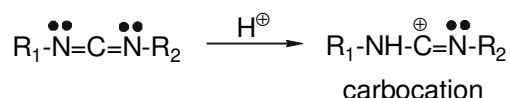
## 6.2 Mechanism of amide bond formation

It is known that the amino moiety is concentrated on the surface firstly by electrostatic attraction between positively charged ligand and the negatively charged carboxyl groups of the surface. During this process the NHS-esters react with nucleophilic groups of the ligand (the  $\alpha$ -amino group).

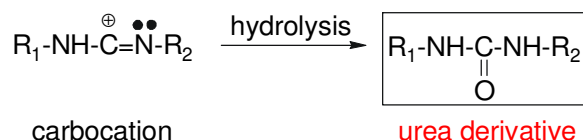
The immobilization according to the principle outlined above depends on a number of parameters, e.g. pH, concentration, ionic strength, and reaction times, and the optimal conditions are individual for the type of ligand to be immobilized.

The following reaction mechanism for the amide formation in aqueous media with the use of carbodiimide was proposed by Nakajima [125].

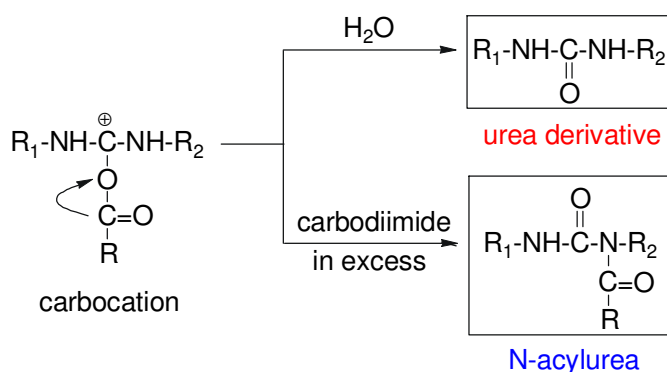
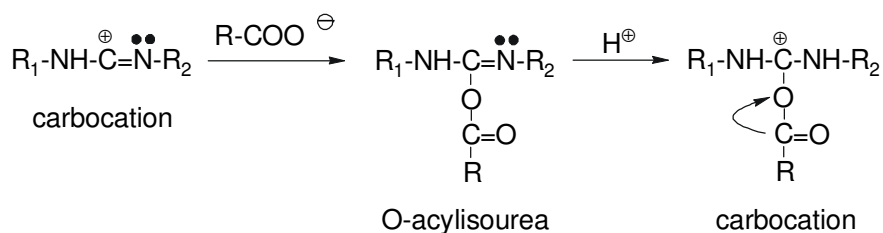
A carbodiimide molecule reacts with a proton to form a carbocation:



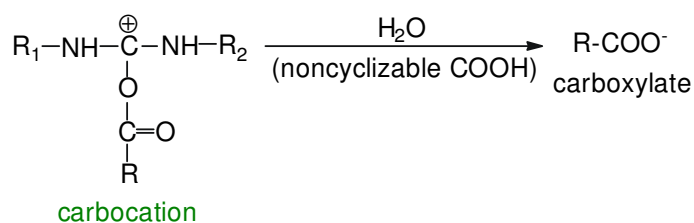
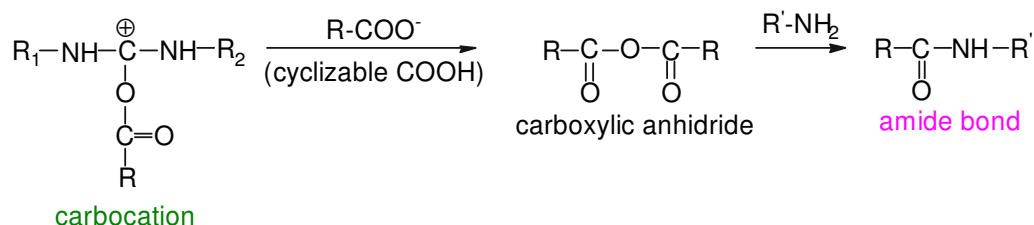
The reaction mechanism of carbodiimide with carboxylic acid is more complicated in aqueous media than in organic systems. Unless carboxylic acid is present, carbocation will be hydrolyzed by water into the corresponding urea derivative:



Carbocation can react with an ionized carboxyl group to form a compound *O*-acylisourea. As a result of deprotonation *O*-acylisourea will change into a carbocation followed by the attack of various bases present in the aqueous system. If any nucleophile is absent, carbocation will transfer into the corresponding urea derivative by the reaction with water.



Since an ionized carboxyl group is a very strong base, its reaction with carbocation may produce carboxylic anhydride in the case of cyclizable carboxyl group, which quickly forms the corresponding amide when amine is present. With noncyclizable carboxyl groups carbocation will be transformed into carboxylate groups.



### 6.3 Determination of integrated molar absorption coefficients of characteristic bands of 7-OTCS

For the determination of the integrated molar absorption coefficients of 7-OTCS in toluene,  $\int \epsilon(\tilde{\nu})d\tilde{\nu}$ , IR transmittance spectra were measured using a  $\text{CaF}_2$  cell with  $\ell = 10 \mu\text{m}$  path length (Figure 59). Four concentrations of 7-OTCS in toluene were used (Table 17).

Characteristic 7-OTCS vibrations should be mentioned: asymmetric  $\nu_{\text{as}}(\text{CH}_2)$  and symmetric  $\nu_{\text{s}}(\text{CH}_2)$  stretching vibrations at  $2927$  and  $2855 \text{ cm}^{-1}$ ; end-standing  $\text{C}=\text{C}$  double bond vibrations:  $\nu_{\text{as}}(\text{CH}=\text{CH}_2)$  at  $3077 \text{ cm}^{-1}$ ,  $\nu(\text{C}=\text{C})$  at  $1641 \text{ cm}^{-1}$  and  $\gamma_{\text{op}}(\text{CH}=\text{CH}_2)$  at  $911 \text{ cm}^{-1}$ . Symmetric  $\nu_{\text{s}}(\text{Si-Cl}_3)$  and asymmetric  $\nu_{\text{as}}(\text{SiCl}_3)$  vibrations at  $564$  and  $587 \text{ cm}^{-1}$  were not accessible with Ge MIRE.

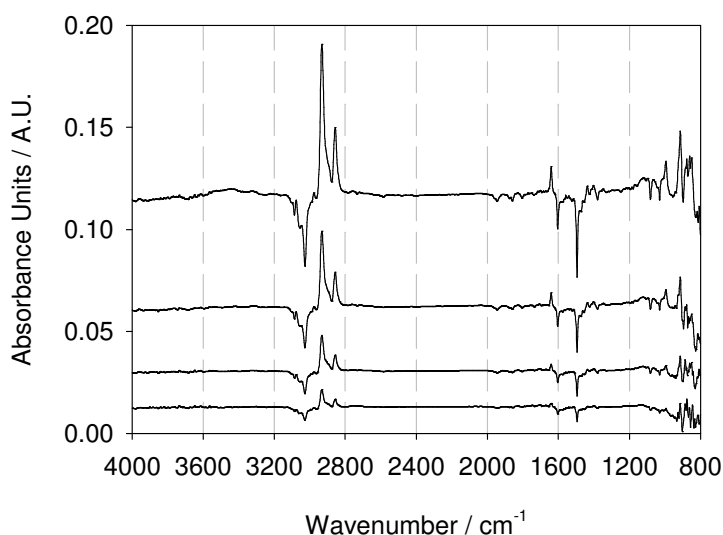


Figure 59. Transmittance spectra of 7-OTCS solutions used for the calculation of integrated molar absorption coefficients of characteristic bands of 7-OTCS molecules.

Integrated molar absorption coefficients were determined according to Lambert-Beer's law (42):

$$\int \epsilon(\tilde{\nu})d\tilde{\nu} = \frac{\int A(\tilde{\nu})d\tilde{\nu}}{c_{\text{CH}_2\text{OTCS}} \cdot \ell} \quad (42)$$

In Table 17 different concentration of 7-OTCS solutions and corresponding integrated absorbancies for symmetric stretching vibrations  $\nu_{\text{s}}(\text{CH}_2)$  in the region between  $2873$ - $2823 \text{ cm}^{-1}$  and asymmetric stretching vibrations  $\nu_{\text{as}}(\text{CH}_2)$  in the region between  $2968$ - $2898 \text{ cm}^{-1}$  are summarized.



Table 17. Different concentrations of 7-OTCS solutions used for the calculation of the integrated molar absorption coefficients of characteristic bands of 7-OTCS and corresponding integrated absorbancies for symmetric and asymmetric stretching vibrations,  $\nu_s(\text{CH}_2)$  and  $\nu_{as}(\text{CH}_2)$ , respectively.

$C_{\text{OTCS}}$ , %(v/v)	$C_{\text{OTCS}}/10^{-5}$ mol/ml	$C_{\text{CH}_2, \text{OTCS}}/\text{mol/L}$	$\int A(\tilde{\nu})d\tilde{\nu} / \text{cm}^{-1}$	$\int A(\tilde{\nu})d\tilde{\nu} / \text{cm}^{-1}$
			symm. 2873-2823 $\text{cm}^{-1}$	asymm. 2968-2898 $\text{cm}^{-1}$
1	4.36	2.61	0.0698	0.2756
2	8.71	5.23	0.1461	0.5565
4	17.4	1.05	0.3061	1.1253
7.75	33.8	2.03	0.5901	2.1982

The corresponding band area was obtained by band integration in the region of symmetric and asymmetric stretching vibrations,  $\nu_s(\text{CH}_2)$  and  $\nu_{as}(\text{CH}_2)$ , using a linear baseline method. Integrated molar absorption coefficients of  $\nu_s(\text{CH}_2)$  and  $\nu_{as}(\text{CH}_2)$  are found to be  $\int \epsilon(\tilde{\nu})d\tilde{\nu} = (2.95 \pm 0.33) \times 10^5 \text{ cm}^2/\text{mol}$  and  $\int \epsilon(\tilde{\nu})d\tilde{\nu} = (10.9 \pm 1.16) \times 10^5 \text{ cm}^2/\text{mol}$ , respectively. The integrated absorbancies were divided by  $N=6$  the number of  $\text{CH}_2$  groups per molecule.

## 6.4 Determination of integrated molar absorption coefficients of sodium acetate bands

Integrated molar absorption coefficients of sodium acetate in water were determined according to Lambert-Beer's law:

$$\int \epsilon(\tilde{\nu}) d\tilde{\nu} = \frac{\int A(\tilde{\nu}) d\tilde{\nu}}{c_{\text{COO}^-} \cdot \ell} \quad (43)$$

Figure 60 shows the SBSR spectra of different concentrated sodium acetate solutions used for the calculation of integrated molar absorption coefficients of characteristic bands.

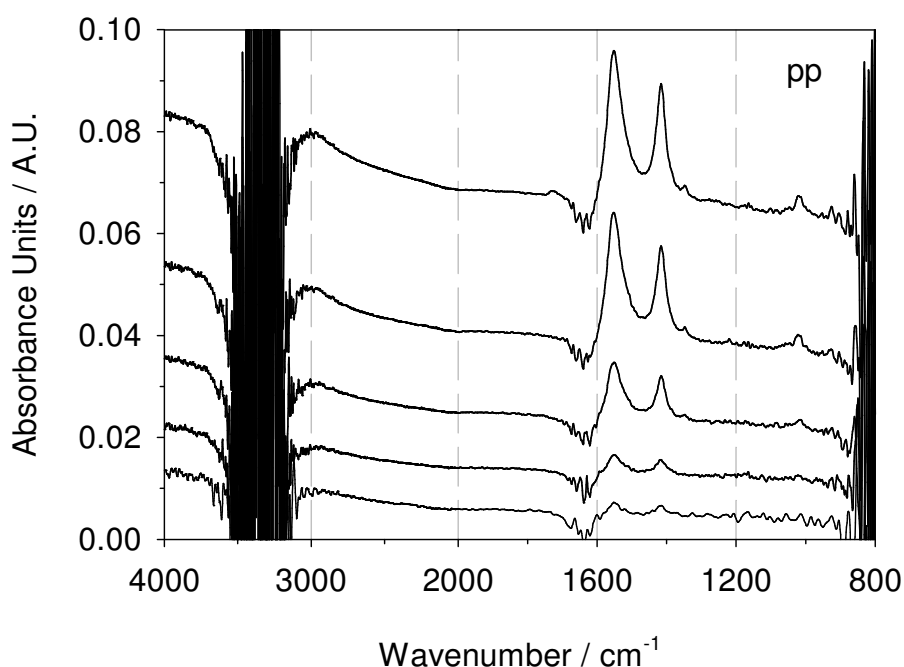


Figure 60. The SBSR FTIR pp-spectra of sodium acetate in water used for the calculation of integrated molar absorption coefficients of symmetric  $\nu_s(\text{COO}^-)$  and asymmetric  $\nu_{as}(\text{COO}^-)$  stretching vibrations.

In Table 18 different concentration of sodium acetate solutions and corresponding integrated absorbances for symmetric stretching vibrations  $\nu_s(\text{COO}^-)$  in the region between  $1459\text{--}1373\text{ cm}^{-1}$  and asymmetric stretching vibrations  $\nu_{as}(\text{COO}^-)$  in the region between  $1616\text{--}1472\text{ cm}^{-1}$  are summarized.

Table 18. Five concentrations of sodium acetate solutions used for the calculation of the integrated molar absorption coefficients of symmetric  $\nu_s(\text{COO}^-)$  and asymmetric  $\nu_{as}(\text{COO}^-)$  stretching vibrations.

$C_{\text{CH}_3\text{COONa}}/10^{-3} \text{ mol/L}$	$\int A(\tilde{\nu})d\tilde{\nu} / \text{cm}^{-1}$	$\int A(\tilde{\nu})d\tilde{\nu} / \text{cm}^{-1}$
	symm. 1459-1373 $\text{cm}^{-1}$	asymm. 1616-1472 $\text{cm}^{-1}$
5	0.0593	0.1371
10	0.0794	0.2300
30	0.2414	0.6561
50	0.4958	1.4391
75	0.6159	1.6624

The corresponding band area was obtained by band integration in the region of symmetric and asymmetric stretching vibrations,  $\nu_s(\text{COO}^-)$  and  $\nu_{as}(\text{COO}^-)$ , using a linear baseline method. Integrated molar absorption coefficients of  $\nu_s(\text{COO}^-)$  and  $\nu_{as}(\text{COO}^-)$  are found to be  $\int \epsilon(\tilde{\nu})d\tilde{\nu} = (9.71 \pm 1.59) \times 10^6 \text{ cm/mol}$  and  $\int \epsilon(\tilde{\nu})d\tilde{\nu} = (2.68 \pm 0.33) \times 10^7 \text{ cm/mol}$ , respectively.

## 6.5 Determination of integrated molar absorption coefficients of amide I' in D<sub>2</sub>O by 2-Acetamido-2-deoxy-D-glucose

Integrated molar absorption coefficient of amide I' in D<sub>2</sub>O was determined according to Lambert-Beer's law:

$$\int \epsilon(\tilde{\nu}) d\tilde{\nu} = \frac{\int A(\tilde{\nu}) d\tilde{\nu}}{c_{\text{amide I'}} \cdot \ell} \quad (44)$$

Spectra of different concentrated 2-Acetamido-2-deoxy-D-glucose (*N*-acetyl-D-glucosamine) solutions are shown in Figure 61. In Table 19 different concentrations of 2-Acetamido-2-deoxy-D-glucose solution and corresponding integrated absorbances of amide I' vibration  $\nu(\text{C}=\text{O})$  in the region between 1662-1588 cm<sup>-1</sup> are summarized.

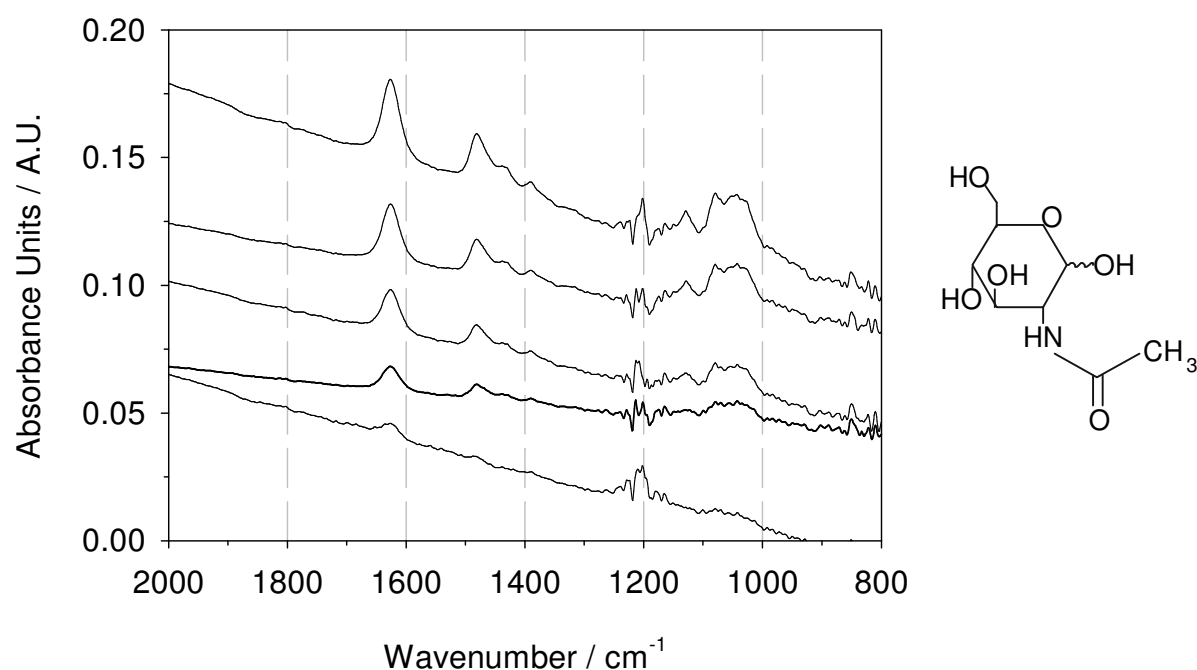


Figure 61. The SBSR FTIR pp-spectra of 2-Acetamido-2-deoxy-D-glucose (*N*-acetyl-D-glucosamine) solutions used for the calculation of integrated molar absorption coefficients of amide I' bands in D<sub>2</sub>O.

Table 19. Relevant parameters used for the calculation of the integrated molar absorption coefficients of amide I'  $\nu(\text{C=O})$  vibrations.

$C_{\text{amide I'}/10^{-3}}$ mol/L	$\int A_{\text{pp}}(\tilde{\nu})d\tilde{\nu}$ [cm <sup>-1</sup> ]	$\int A_{\text{vp}}(\tilde{\nu})d\tilde{\nu}$ [cm <sup>-1</sup> ]	$d_{\text{e,pp}}^b/10^{-5}$ [cm]	$d_{\text{e,vp}}^b/10^{-5}$ [cm]	$\int \epsilon_{\text{pp}}(\tilde{\nu})d\tilde{\nu}$ 10 <sup>-5</sup> [mol/cm]	$\int \epsilon_{\text{vp}}(\tilde{\nu})d\tilde{\nu}$ 10 <sup>-5</sup> [mol/cm]
7.9	0.1581	0.0696	4.29	2.14	1.53	1.57
15	0.2831	0.1425	4.29	2.14	1.53	1.50
27	0.4851	0.2516	4.29	2.14	1.54	1.60
37.5	0.6698	0.3227	4.29	2.14	1.62	1.63
50	0.8925	0.4570	4.29	2.14	1.71	1.51

The corresponding band area was obtained by band integration in the region of amide I' vibrations,  $\nu(\text{C=O})$  using a linear baseline method. Integrated molar absorption coefficient of amide I' is calculated according to eq.  $\int \epsilon_{\text{pp/vp}}(\tilde{\nu})d\tilde{\nu} = \int A_{\text{pp/vp}}(\tilde{\nu})d\tilde{\nu} / (c \cdot N_{\text{refl}} \cdot v \cdot d_{\text{e,pp/vp}}^b)$ , where  $c$  denotes the concentration,  $N_{\text{refl}}$  the number of reflections (=27.21),  $v$  the number of the functional groups (=1). For the calculation of the effective thickness of bulk medium  $d_{\text{e,pp/vp}}^b$  the following eqs. were used:  $d_{\text{e,pp}}^b = n_{31} \cdot d_{\text{p3}} \cdot (E_{0x3}^{r^2} + E_{0z3}^{r^2}) / 2\cos\theta$  and  $d_{\text{e,vp}}^b = n_{31} \cdot d_{\text{p3}} \cdot E_{0y3}^{r^2} / 2\cos\theta$ . Integrated molar absorption coefficient of amide I' was found to be  $\int \epsilon(\tilde{\nu})d\tilde{\nu} = (1.57 \pm 0.09) \times 10^7$  cm/mol.

## 6.6 Oxidized silane layer

Figure 62 presents oxidized silane layer used for amide bond formation to amino-dextran. The surface concentration of available  $\text{COO}^-$  groups produced by ozone was found to be  $\Gamma_{\text{exp}} = (1.59 \pm 0.24) \times 10^{-10} \text{ mol/cm}^2$ , Table 20.

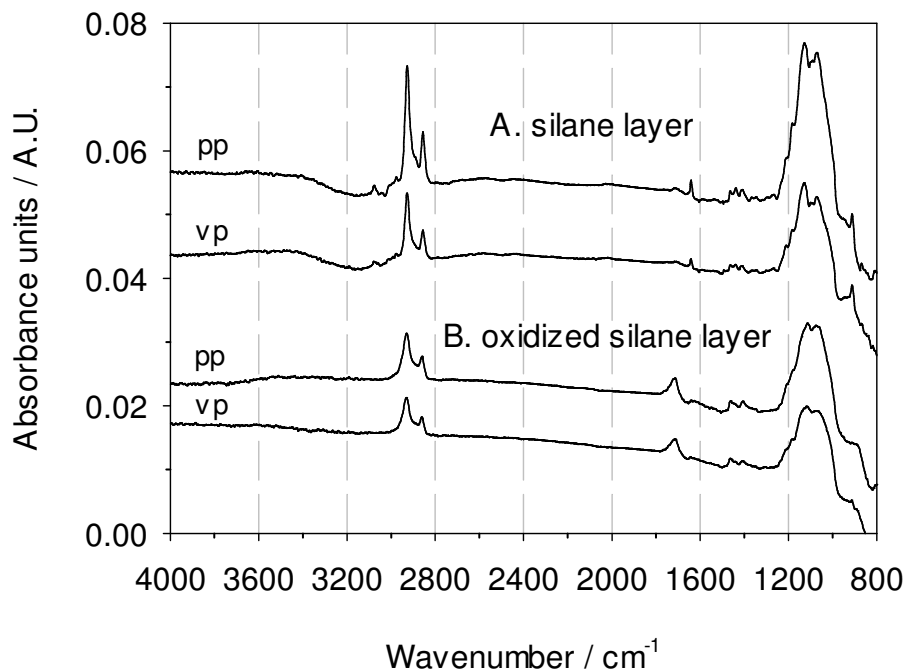


Figure 62. A. The SBSR FTIR pp- and vp-spectra of the silane layer thicknesses of 2.3 nm in toluene; reference: pure toluene. B. The SBSR FTIR pp- and vp-spectra of the oxidized silane layer in air; reference: air. Ge MIRE;  $T=15^\circ\text{C}$ ; Angle of incidence  $\theta=45^\circ$ ; Number of active internal reflections  $N=27.97$ .

Table 20. Magnitudes and uncertainties of input parameters for  $\nu_{\text{as}}(\text{COO}^-)$  vibrations in  $\text{H}_2\text{O}$  produced by oxidation of a silane layer. Integrated molar absorption coefficients are overtaken from ref. [114].

<i>Parameter, Symbol</i>	<i>Magnitude</i>
Angle of incidence, $\theta/\text{deg}$	$45.0 \pm 1.5$
Refractive index of germanium MIRE, $n_1$	$4.0 \pm 0.0$
Refractive index of an adsorbed/bound layer, $n_2$	$1.45 \pm 0.05$
Refractive index of bulk ( $\text{H}_2\text{O}$ ) at $1550\text{cm}^{-1}$ , $n_3$	$1.34 \pm 0.05$
Integrated molar absorption coefficient of $\nu_{\text{as}}(\text{COO}^-)$ , $\int \epsilon(\tilde{\nu}) d\tilde{\nu} / 10^7 \text{ cm/mol}$	$2.68 \pm 0.33$
Integrated absorbance of $\nu_{\text{as}}(\text{COO}^-)$ , $\int A_{\text{pp/vp}}(\tilde{\nu}) d\tilde{\nu} / \text{cm}^{-1}$	$0.22 \pm 0.01$
Integration range $1616 \pm 1 - 1472 \pm 1 \text{ cm}^{-1}$	$0.151 \pm 0.008$
Number of equal functional groups per molecule, $\nu$	$1 \pm 0$
Number of active internal reflections, $N$	$27.97 \pm 1$

## References

- 1 Schreiber F., *Progress in Surface Science* **2000**, 65, 151-256.
- 2 Tabor, D. J. *Colloid Interface Sci.* **1980**, 75, 240
- 3 Franklin, B., *Phil. Trans. R. Soc.* **1774**, 64, 445
- 4 Pockels, A., *Nature* **1891**, 43, 437-439.
- 5 Langmuir, I., *J. Am. Chem. Soc.* **1917**, 39, 1848-1904.
- 6 Blodgett, K., B. J. *Am. Chem. Soc.* **1935**, 57, 1007-1022.
- 7 Pradeep T., *Resonance*, **1999**, 53-62.
- 8 Bigelow W.C., Pickett D.L., Zisman W.A., *J. Colloid Interface Sci.* **1**, **1946**, 513
- 9 Blackman L.C.F., Dewar M.J.S., *J. Chem. Soc.* **162**, **1957**, Part I- IV
- 10 Netzer L., Sagiv J., *J. Am. Chem. Soc.* **1983**, 105, 674
- 11 Nuzzo, R. G.; Allara, D. L., *J. Am. Chem. Soc.* **1983**, 105, 4481.
- 12 Durmaz Firat, PhD Thesis, A Modular Approach to Functional Self-Assembled Monolayers, ETH Zurich, 2006
- 13 Ulman A., *An introduction to ultrathin organic films: from Langmuir-Blodgett to self-assembly*; First ed.; Academic Press: San Diego, **1991**.
- 14 Zehner R.W., *Design and characterisation of novel systems for molecular and nanoscale self-assembly*, PhD dissertation, Department of Chemistry, The University of Chicago, Chicago, Illinois, **1998**
- 15 Huimin Li, PhD Dissertation, *Relationship Between Molecular Structure and Surface Properties of Self-Assembled Monolayers*, Virginia Polytechnic Institute, State University, Blacksburg, Virginia, **2004**
- 16 Yong Zhu, Joel Gregie, *Self-Assembled Monolayer used in Micro-motors*, Term Project, **2000**
- 17 Kumar A., Biebuyck H. A., Whitesides G. M., *Langmuir* **1994**, 10, 1498-1511.
- 18 Durmaz Firat, *A Modular Approach to Functional Self-Assembled Monolayers*, PhD Dissertation, ETH Zürich, **2006**
- 19 *Silicon Compounds: Silanes and Silicones, A Survey of Properties and Chemistry*, Edited by Barry Arkles & Gerald Larson, **2004**, Gelest, Inc., Morrisville, PA
- 20 Madsen N.B., PhD Dissertation, *Modification and characterization of the interface in polymer/inorganic composites*, Risø National laboratory, Roskilde, Denmark, **1999**
- 21 Bain C.D., Whitesides G.M., *Angew. Chem. Int. Ed. Engl.* **1989**, 28, 506.
- 22 Wasserman S.R., Whitesides G.M., Tidswell I.M., Ocko B.M., Pershan P.S., J.D. Axe, *J. Am. Chem. Soc.* **1989**, 111, 5852.
- 23 Ulman A. (Ed.), *Self-Assembled monolayers of thiols, Thin Films*, vol. 24, Academic Press, San Diego, **1998**
- 24 Poirier G.E., *Chem. Rev.* **1997**, 97, 1117
- 25 Matijašević J., Glowacky J., Koker T., Heissler S., Faubel W. and Fringeli U.P., to be published
- 26 Lüth H., *Surfaces and Interfaces of Solids*, Springer, Berlin, **1993**.
- 27 Dubois L.H., Zegarski B.R., Nuzzo R.G., *J. Phys. Chem.* **1993**, 98, 678.



- 
- 28 Feidenhans'l R., *Surf. Sci. Rep.* **1989**, 10, 105.
- 29 Dosch H., *Critical Phenomena at Surfaces and Interfaces*, Springer Tracts in Modern Physics, vol. 126, Springer, Heidelberg, **1992**.
- 30 Scoles G. (Ed.), *Atomic and Molecular Beam Methods*, vols. 1 and 2, Oxford University Press, Oxford, **1992**.
- 31 Chidsey C.E.D., Liu G.-Y., Rowntree P., Scoles G., *J. Chem. Phys.* **1989**, 91, 4421.
- 32 Tolan M., *X-ray Scattering from Soft-Matter Thin Films*, Springer Tracts in Modern Physics, vol. 148, Springer, Heidelberg, **1999**.
- 33 Tidswell I.M., Ocko B.M., Pershan P.S., Wasserman S.R., Whitesides G.M., Axe J.D., *Phys. Rev. B* **1990**, 41, 1111.
- 34 Ulman A., *An introduction to ultrathin organic films: from Langmuir-Blodgett to self-assembly*; First ed.; Academic Press: San Diego, **1991**.
- 35 Nuzzo R.G., Dubois L.H., Allara D.L., *J. Am. Chem. Soc.* **1990**, 112, 558.
- 36 Parikh A.N., Allara D.L., *J. Chem. Phys.* **1992**, 96, 927.
- 37 Wenzl P., Fringeli M., Goette J., and Fringeli U.P., *Langmuir* **1994**, Vol. 10, No. 11, 4253-4264.
- 38 Hassler N., Reiter G., Weber V., Falkenhagen D. and Fringeli U.P., *Biochimica et Biophysica Acta* **2004**, 1699, 253– 261.
- 39 Matijašević J., Hassler N., Reiter G., and Fringeli U.P., *Langmuir* **2008**, 24, 2588-2596.
- 40 Kluth G.J., Carraro C., Maboudian R., *Phys. Rev. B* **1999**, 59, R10449-R10452.
- 41 Stöhr J., *NEXAFS Spectroscopy*, Springer, New York, **1992**.
- 42 Richter A.G., Yu C.-J., Datta A., Kmetko J., Dutta P., *Phys. Rev. E* **2000**, 61, 607.
- 43 Brzoska J.B., Shahidzadeh N., Rondelez F., *Nature* **1992**, 360, 719
- 44 Parikh A.N., Allara D.L., Azouz I.B., Rondelez F., *J. Phys. Chem.* **1994**, 98, 7577.
- 45 Vallant T., Kattner J., Brunner H., Mayer U., Hoffmann H., *J. Phys. Chem.* **1998**, 102, 7190.
- 46 Finklea H.O., Robinson L.R., Blackburn A., Richter B., *Langmuir* **1986**, 2, 239-244.
- 47 Tao Ye, *Structure, dynamics and reactivity of molecular assemblies at interfaces*, PhD Dissertation, Faculty of Arts and Science, University of Pittsburgh, **2003**
- 48 Dubois, L.H. and R.G. Nuzzo, *Synthesis, structure, and properties of model organic surfaces*. Annual Review of Physical Chemistry, **1992**. 43, 437-463.
- 49 Ulman, A., *Formation and structure of Self-Assembled monolayers*. Chemical Reviews, **1996**, 96, 1533-1554.
- 50 Vermette P., Gauvreau V., Pézolet M., Laroche G., *Colloids Surf. B: Biointerfaces* **2003**, 29, 285-295.
- 51 Senaratne W, Andruzzi L., and Ober C.K., *Biomacromolecules* **2005**, 6, 2427-2448.
- 52 Li D., Ratner M. A., Marks T. J., *J. Am. Chem. Soc.* **1990**, 112, 7389-7390.
- 53 Swalen J. D., Allara D. L., Andrade J. D., Chandross E. A., Garoff S., Israelachvili J., McCarthy T. J., R. Murray, R. F. Pease, J. F. Rabolt, K. J. Wynne, and Yu H., *Langmuir* **1987**, 3, 932-950.
- 54 Ito K., Ariyoshi Y., Tanabiki F., Sunahara H., *Anal. Chem.* **1991**, 63, 273-276.
- 55 Liu S., Maoz R., Schmiedt G., Sagib J., *Nanoletters* **2002**, 2, 10, 1055-1060.
- 56 Durand R. R., Bencosme S.C., Collman J.P., Anson F.C., *J. Am. Chem. Soc.* **1983**, 105, 2710-

- 2718.
- 57 Li G., Ma H., Jiao Y., Chen S., *J. Serb. Chem. Soc.* **2004**, 69, 10, 791-805.
- 58 Green J-B. D., McDermott M. T., Porter M. D., Siperko L. M., *J. Phys. Chem.* **1995**, 99, 10960-10965.
- 59 Porter M. D., Bright T. B., Allara D. L., Chidseyi C.E.D., *J. Am. Chem. Soc.* **1987**, 109, 3559-3568.
- 60 Stojanović D., Vuković G.D., Orlović A.M., Uskoković P.S., Aleksić R., Bibić N., Dramićanin M.D., *Industrial Engineering Research* **2007**, 4, 93-102.
- 61 Arkles, B., *Tailoring surfaces with silanes*. Chemtech, **1977**, 7, 766-778.
- 62 Dulcey, C.S., J.H. Georger Jr., V. Krauthamer, D. Stenger, T.L. Fare, and J.M. Calvert, *Deep UV photochemistry of chemisorbed monolayers: patterned coplanar molecular assemblies*. Science, **1991**, 252, 551-554.
- 63 Komeda, T., K. Namba, and Y. Nishioka, *Applied Physics Letters* **1997**, 70, 25, 3398-3400.
- 64 Sugimura, H., K. Ushiyama, A. Hozumi, and O. Takai, *Langmuir* **2000**, 16, 13, 885-888.
- 65 Schneeweiss, M.A., H. Hagenstrom, M.J. Esplandiu, and D.M. Kolb, *Applied Physics A-Materials Science & Processing* **1999**, 69, 5, 537-551.
- 66 Moberg, P. and R.L. McCarley, *Journal of the Electrochemical Society* **1997**, 144, 6, L151-L153.
- 67 Zheng, J.W., Z.H. Zhu, H.F. Chen, and Z.F. Liu, *Langmuir* **2000**, 16, 10, 4409-4412.
- 68 Doppelt, P. and M. Stelzle, *Microelectronic Engineering* **1997**, 33, 1-4, 15-23.
- 69 Wang M.S., Palmer L.B., Schwartz J.D., and Razatos A., *Langmuir* **2004**, 20, 7753-7759.
- 70 Mrksich, M. and G.M. Whitesides, *Annual Review of Biophysics and Biomolecular Structure* **1996**, 25, 55-78.
- 71 Lingler, S., I. Rubinstein, W. Knoll, and A. Offenhausser, *Langmuir* **1997**, 13, 26, 7085-7091.
- 72 Collet, J., M. Bonnier, O. Bouloussa, F. Rondelez, and D. Vuillaume, *Microelectronic Engineering* **1997**, 36, 1-4, 119-122.
- 73 Vuillaume, D., C. Boudas, J. Collet, J.V. Davidovits, and F. Rondelez, *Applied Physics Letters* **1996**, 69, 11, 1646-1648.
- 74 Bumm, L.A., J.J. Arnold, M.T. Cygan, T.D. Dunbar, T.P. Burgin, L. Jones, D.L. Allara, J.M. Tour, and P.S. Weiss, *Science* **1996**, 271, 5256, 1705-1707.
- 75 Kasemo B, *Surface Science* **2002**, 500, 656-677.
- 76 Patel N., Davies M.C., Hartshorne M., Heaton R.J., Roberts C.J., Tendler S.J.B., and Williams P.M., *Langmuir* **1997**, 13, 6485-6490.
- 77 Silin V., Weetal H., and Vanderah D.J., *Journal of Colloid and Interface Science* **1997**, 185, 94-103.
- 78 Frey B.L, Corn R.M., *Anal. Chem.* **1996**, 68, 3187-3193.
- 79 Khalikova E., Susi P., and Korpela T., *Microbiology and Molecular Biology Reviews* **2005**, 69, 2, 306-325.
- 80 Massia S.P., Stark J., Letbetter D.S., *Biomaterials* **2000**, 21, 2253-2261.
- 81 Trudel J, Massia S.P., *Biomaterials* **2002**, 23, 3299-3307.
- 82 Leonard, E., Turitto, V., Vincent, T. and Vroman, L., *Blood in contact with natural and artificial surfaces*, New York Academy of Science, New York, 1987.
- 83 Wang M.S., Palmer L.B., Schwartz J.D., and Razatos A., *Langmuir* **2004**, 20, 7753-7759.

- 
- 84 Baurecht D., Reiter G., Hassler N., Schwarzott M., Fringeli U.P., *Chimia* 2005, 59, 226-235.
- 85 Born, M., Wolf, E., *Principles of Optics*, Oxford: Pergamon Press, **1983**, 6<sup>th</sup> ed. Ch.1, pp. 47- 51.
- 86 Fringeli U.P., in *Encyclopedia of Spectroscopy and Spectrometry: ATR and Reflectance IR Spectroscopy*, Applications; John Cl. Lindon, **2000**; pp. 58-75.
- 87 Goos F. and Lindberg-Hänchen H., *Ann. Phys* **1949**, 5, 251
- 88 Fringeli, U.P. in Mirabella, F.M. (Ed.), *Internal Reflection Spectroscopy, Theory and Applications*, Marcel Dekker **1992**, Chpt. 10, 255-324.
- 89 Oliver Maute, PhD Thesis: Preparation of Ordered *tert*-Butylcalix[4]arene Layers on Modified Surfaces: Comparative FTIR, SFM, TPD, and Contact Angle Studies, Fakultät für Chemie und Pharmazie der Eberhard Karls Universität Tübingen, **1999**.
- 90 Harrick N.J., *Internal Reflection Spectroscopy*, John Wiley & Sons, Inc., **1967**.
- 91 Fringeli U. P., Baurecht D., Bürgi T., Siam M., Reiter G., Schwarzott M. and Brüesch P., ATR Spectroscopy of Thin Films. In: H. S. Nalwa (ed.), *Handbook of Thin Films Materials*, Vol. 2, Chapter 4, Academic Press, **2002**, pp. 191-229.
- 92 Fringeli U.P., Reiter G., and Matijašević J., *Applied Spectroscopy*, to be published
- 93 OPTISPEC, Rigistrasse 5, CH-8173 Neerach (Switzerland), [www.optispec.ch](http://www.optispec.ch)
- 94 Fringeli, U.P. in Schlunegger, U.P. (Ed.), *Biologically Active Molecules*; Springer: Berlin, **1989**; pp. 241-252.
- 95 Fringeli, U., Baurecht, D. and Günthard, Hs. H. and *Infrared and Raman Spectroscopy of Biological Materials*. Edited by H.-U. Gremlich, Novartis Pharma AG, Basel, Switzerland, and B. Yan, ChemRx Advanced Technologies, Inc., South San Francisco, California, **2001**
- 96 Baurecht, D. and Fringeli, U., Quantitative modulated excitation Fourier transform infrared spectroscopy, **2001**, *Review of Scientific Instruments* 72 (10), 3782-3792.
- 97 Maentele, W.(**1996**). *Infrared and Fourier-transform infrared spectroscopy*. In *Biophysical Techniques in Photosynthesis* (eds. J. Ames & A. J. Ho.), pp. 137–160. Dordrecht: Kluwer Academic Publishers.
- 98 Günthard, Hs. H., *Ber. Busenges. Phys. Chem.* **1978**, 78, p. 1110.
- 99 Eigen, M., De Maeyer, L. In: Friess, SL. et al. (**1963**), *Techniques of Organic Chemistry*. Vol. 8. Part 2. New York: Wiley-Interscience, 895-1054.
- 100 Strehlow, H. & Knoche, W. (**1977**). *Fundamentals of Chemical Relaxation*. Weinheim, Germany: Verlag Chemie
- 101 Norrod K.L., Rowlen K.L., *J. Am. Chem. Soc.* **1998**, 120, 2656-2657.
- 102 Johnson B., Loefas S. and Lindquist G., *Analytical Biochemistry* **1991**, 198, 268-277.
- 103 Cattaruzza F., et al, *Nucleic Acids Research* **2006**, 34, 4, e32
- 104 Voicu R., Boukherroub R., Bartzoka V., Ward T., Woytyk J.T.C., Wayner D.D.M., *Langmuir* **2004**, 20, 11713-11720.
- 105 Chou Y.P., Lee S.C., *Journal of Applied Physics* **1998**, 83, 8, 4111-4123.
- 106 Ay F., Audinli A., *Applied Physics Letters* **2003**, 83, 23, 4743-4745.
- 107 Brzoska J. B., Azouz I. B., Rondelez F, *Langmuir* **1994**, 10, 11, 4367-4373.
- 108 Matinlinna J.P., Areva S., Lassila L.V.J., Vallittu P.K., *Surf. Interface Anal.* **2004**, 36, 1314-1322.

- 109 R  he J., Novotny V. J., Kanazawa K. K., Clarke T., Street G. B., *Langmuir* **1993**, 9, 2383-2388.
- 110 Wojtyk J.T.C., Morin K.A., Boukherroub R., Wayner D.D.M., *Langmuir* **2002**, 18, 6081-6087.
- 111 Grubor N.M., Shinar R., Jankowiak R., Porter M.D., Small G.J., *Biosensors and Bioelectronics* **2004**, 19, 547-556.
- 112 Lahiri J., Isaacs L., Tien J., and Whitesides M., *Anal. Chem.* **1999**, 71, 777-790.
- 113 Soultani-Vigneron S. et al., *Journal of Chromatography B* **2005**, 822, 304-310.
- 114 Fringeli U.P., Apell H.-J., Fringeli M., L  uger P., *Biochimica nad Biophysica Acta* **1989**, 984, 301-312.
- 115 Fringeli U.P. ang G  nthard H.H., Grell E. (Ed.), *Infrared Membrane Spectroscopy*; Springer: Berlin, **1981**; pp. 270-332.
- 116 Kizil R., Irudayaraj J., Seetharaman K., *J. Agric. Food Chem.* **2002**, 50, 14, 3912-3918.
- 117 Reiter G., Hassler N., Weber V., Falkenhagen D., Fringeli U.P., *Biochimica et Biophysica Acta* **2004**, 1699, 253-261.
- 118 Matinlinna J.P., Areva S., Lassila L.V.J., Vallittu P.K., *Surf. Interface Anal.* **2004**, 36, 1314-1322.
- 119 Glowacky J., Heissler St., Leiste H., Koker T., Faubel W., and Gerdes A., *Investigation of the formation of ultrathin siloxane films on functionalized Germanium crystals by FTIR-ATR spectroscopy*, International Conference on Advanced Vibrational Spectroscopy 4 (ICAVS4), **2007**.
- 120 Naydenov V., *Modified Molecular Sieve Macrostructures*, Division of Chemical Technology, Department of Chemical and Metallurgical Engineering, Lulea University of Technology, Lulea, Sweden, **2002**
- 121 Wu X., *Acidity and catalytic activity of zeolite catalysts bound with silica and alumina*, Office of Graduate Studies of Texas A&M University, **2003**
- 122 Usher C.R., Michel A.E., Grassian V.H., *Chem. Rev.* **2003**, 103, 4883-4939.
- 123 Dubowski Y., Vieceli J., Tobias D.J., Gomez A., Lin A., Nizkorodov S.A., McIntire T.M., Finlayson-Pitts B.J., *J.Phys.Chem.A* **2004**,
- 124 Park J., Gomez A.L., Walser M.L., Lin A., Nizkorodov S.A., *Phys. Chem. Chem. Phys.* **2006**, 8, 2506-2512.
- 125 Nakajima N., Ikada Y., *Bioconjugate Chem.* **1995**, 6, 123-130.

## Lebenslauf

### Persönliche Daten:

- ◆ Geboren: 30.06.1980 in Belgrad, Serbien
- ◆ Familienstand: ledig
- ◆ Staatsangehörigkeit: Republik Serbien

### Studium:

- ◆ Okt. 2004 - Sept. 2008 Doktoratstudium am Institut für Biophysikalische Chemie der Universität Wien, Thema: "Synthesis of biomimetic surfaces under permanent in situ FTIR ATR monitoring"
- ◆ 2003 Diplomarbeit zum Thema: "Synthesis of peptide-steroid conjugates on polymer support and their physicochemical characterisation"
- ◆ Okt. 1999 - Okt. 2003 Studium der Physikalischen Chemie an der Fakultät für Physikalische Chemie der Universität Belgrad

### Schul Ausbildung:

- ◆ 1999 Matura, Thema: "Iron"
- ◆ Sept. 1996 - Juni 1999 5. Belgrader Gymnasium, Richtung Naturwissenschaften und Mathematik
- ◆ Sept. 1987 - Juni 1996 Grundschule "Starina Novak", Belgrad

### Wissenschaftliche Arbeit (Berufspraxis):

- ◆ Sept. 2007 - Aug. 2008 Assistentin in Ausbildung am Institut für Biophysikalische Chemie der Universität Wien

### Stipendien und Auszeichnungen:

- ◆ 2003 Bester Student des Jahrgangs 1999, Fakultät für Physikalische Chemie der Universität Belgrad
- ◆ 2003 Beste Diplomarbeit des Jahres in Chemie, Kostić Foundation
- ◆ 2003 Beste Diplomarbeit des Jahres in Chemie, Bulajić Foundation
- ◆ Okt. 2003 - Okt. 2004 Stipendium des serbischen Ministeriums für Wissenschaft und Ausbildung
- ◆ Okt. 2004 - März 2005 Stipendium der Universität Wien
- ◆ Apr. 2005 - Aug. 2007 Stipendium der Firma OPTISPEC, Swiss und des Instituts für Biophysikalische Chemie der Universität Wien

### Weitere Qualifikationen:

#### Sprachen:

- ◆ Serbisch (Kroatisch, Bosnisch and Montenegrinisch)-Muttersprache
- ◆ Englisch-sehr gut in Wort und Schrift
- ◆ Deutsch-Grundkenntnisse
- ◆ Russisch-Grundkenntnisse

#### EDV:

- ◆ MS-Office, Windows 95/98/NT/ME/XP
- ◆ Opus, SigmaPlot, ChemWin, Corel DRAW

### Weitere Interessen:

- ◆ Sport (Fitness, Laufen, Schwimmen, Radfahren)
- ◆ Lesen, Reisen

### Publikationen:

#### Wissenschaftliche Artikel in Zeitschriften:

- ◆ Jasmina Matijašević, Norbert Hassler, Gerald Reiter and Urs Peter Fringeli, *In situ* ATR FTIR monitoring of the formation of functionalized monolayers on germanium substrate: From 7-Octenyltrichlorosilane to 7-Carboxylsilane, *Langmuir* **2008**, 24, 2588-2596.
- ◆ Matijašević J., Glowacky J., Koker T., Heissler S., Faubel W. and Fringeli U.P., Nanoparticle sized molecular sieve remnants from solvent drying may incorporate into thin organic surface layers and probably act as catalyst, *Langmuir* **2008**, in preparation

#### Publizierte Konferenzbeiträge:

- ◆ 11. Österreichische Chemietage, 19. - 22. Sept. 2005, Montanuniversität, Leoben, Österreich, Präsentation des Posters: *In Situ Monitoring of Surface Chemical Reactions by Fourier Transform Infrared Attenuated Total Reflection (FTIR ATR) Spectroscopy*
- ◆ 6<sup>th</sup> EBSA&British Biophysical Society Congress, 14. - 18. Juli 2007, Imperial College, London, Großbritannien, Präsentation des Posters: *In situ ATR FTIR monitoring of the formation and modification of the silane layers on germanium substrate*